

Investigation of Effects of Ternary Alloying on the Hydrogen Storage Behavior of ZrCo Alloy

By

Ram Avtar Jat

CHEM01201004018

Bhabha Atomic Research Centre, Mumbai

A thesis submitted to the

Board of Studies in Chemical Sciences

In partial fulfillment of requirements

For the Degree of

DOCTOR OF PHILOSOPHY

of

HOMI BHABHA NATIONAL INSTITUTE

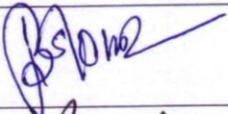
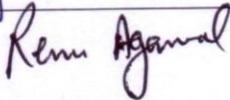

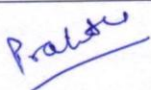





July, 2016

Homi Bhabha National Institute

Recommendations of the Viva Voce Committee

As members of the Viva Voce Committee, we certify that we have read the dissertation prepared by **Shri Ram Avtar Jat** entitled "**Investigation of Effects of Ternary Alloying on the Hydrogen Storage Behavior of ZrCo Alloy**" and recommend that it may be accepted as fulfilling the thesis requirement for the award of Degree of Doctor of Philosophy.

| | | |
|-------------------------------------|---|-----------------|
| Chairman - Sr. Prof. B.S. Tomar |  | Date: 19/7/2016 |
| Guide / Convener - Dr. Renu Agarwal |  | Date: 19/7/2016 |
| Co-guide - Dr. S.C. Parida |  | Date: 19/7/2016 |
| Examiner - Prof. Pratibha Sharma |  | Date: 19/7/16 |
| Member 1- Dr. S. Kannan |  | Date: 19.7.16 |
| Member 2- Dr. S.K. Mukerjee |  | Date: 19-7-16. |
| Member 3- Dr. Smruti Dash |  | Date: 19/7/2016 |

Final approval and acceptance of this thesis is contingent upon the candidate's submission of the final copies of the thesis to HBNI.

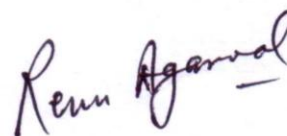
I hereby certify that we have read this thesis prepared under our direction and recommend that it may be accepted as fulfilling the thesis requirement.

Date: 19/7/2016

Place: Mumbai

(Dr. S.C. Parida)

Co-guide



(Dr. Renu Agarwal)

Guide

STATEMENT BY AUTHOR

This dissertation has been submitted in partial fulfillment of requirements for an advanced degree at Homi Bhabha National Institute (HBNI) and is deposited in the Library to be made available to borrowers under rules of the HBNI.

Brief quotations from this dissertation are allowable without special permission, provided that accurate acknowledgement of source is made. Requests for permission for extended quotation from or reproduction of this manuscript in whole or in part may be granted by the Competent Authority of HBNI when in his or her judgment the proposed use of the material is in the interests of scholarship. In all other instances, however, permission must be obtained from the author.



(Ram Avtar Jat)

DECLARATION

I, hereby declare that the investigation presented in the thesis has been carried out by me. The work is original and has not been submitted earlier as a whole or in part for a degree / diploma at this or any other Institution / University.



(Ram Avtar Jat)

List of Publications arising from the thesis

Journal: 07

1. "Structural and hydrogen isotope storage properties of Zr-Co-Fe alloy", **Ram Avtar Jat**, Ripandeeep Singh, S.C. Parida, A. Das, Renu Agarwal, K.L. Ramakumar, *International Journal of Hydrogen Energy*, 40, **2015**, 5135-5143.
2. "Determination of deuterium site occupancy in ZrCoD_3 and its role in improved durability of Zr-Co-Ni deuterides against disproportionation", **Ram Avtar Jat**, Ripandeeep Singh, S.C. Parida, A. Das, Renu Agarwal, K.L. Ramakumar, *International Journal of hydrogen energy*, 39, **2014**, 15665-15669.
3. "Investigation of hydrogen isotope effect on storage properties of Zr-Co-Ni alloys", **Ram Avtar Jat**, S.C. Parida, Renu Agarwal, K.L. Ramakumar, *International Journal of hydrogen energy*, 39, **2014**, 14868-14873.
4. "Effect of Ni content on the hydrogen storage behavior of $\text{ZrCo}_{1-x}\text{Ni}_x$ alloys", **Ram Avtar Jat**, S.C. Parida, Renu Agarwal, S.G. Kulkarni, *International Journal of hydrogen energy*, 38, **2013**, 1490-1500.
5. "Hydrogen sorption-desorption studies on ZrCo-Hydrogen system", **Ram Avtar Jat**, S.C. Parida, J. Nuwad, Renu Agarwal and S.G. Kulkarni, *Journal of Thermal Analysis and Calorimetry*, 112, **2013**, 37–43.
6. "Synthesis, characterization and hydrogen isotope storage properties of Zr-Ti-Co ternary alloys", **Ram Avtar Jat**, Subhasis Pati, S.C. Parida, Renu Agarwal and S.K. Mukerjee, Communicated to *International Journal of hydrogen energy* (MS # HE-D-16-01607).
7. "An analogy of interstitial site occupancy and hydrogen induced disproportionation of $\text{Zr}_{1-x}\text{Ti}_x\text{Co}$ ternary alloys", **Ram Avtar Jat**, Ripandeeep Singh, Subhasis Pati, P.U. Sastry, A. Das, Renu Agarwal and S.C. Parida, Communicated to *The Journal of Physical Chemistry C* (MS # jp-2016-08700e).

Conferences: 06

1. Hydrogen isotope storage behavior of $\text{Zr}_{1-x}\text{Ti}_x\text{Co}$ alloys, **Ram Avtar Jat**, Subhasis Pati, S.C. Parida, Renu Agarwal, S.K. Mukerjee, 20th DAE-BRNS International Symposium & Workshop on Thermal Analysis, THERMANS-2016, January 18-20, 2016, Indian Institute of Technology (BHU) Varanasi, Varanasi, India, pp. 77.

2. Hydrogen induced disproportionation studies on Zr-Co-M (M=Ni, Fe, Ti) ternary alloys, **Ram Avtar Jat**, Subhasis Pati, P. U. Sastry, V.B. Jayakrishnan, S.C. Parida, Renu Agarwal, S.K. Mukerjee, 20th DAE-BRNS International Symposium & Workshop on Thermal Analysis, THERMANS-2016, January 18-20, 2016, Indian Institute of Technology (BHU) Varanasi, Varanasi, India, pp. 78.
3. Effect of Ni content on hydrogen occupancy in $\text{ZrCo}_{1-x}\text{Ni}_x$ deuterides, **Ram Avtar Jat**, Ripandeep Singh, S.C. Parida, A. Das, Renu Agarwal, A.R. Joshi, K.L. Ramakumar, 58th DAE-Solid State Physics Symposium (DAE-SSPS-2013), December 17-21, 2013, Thapar University, Patiala, Punjab.
4. Hydrogen isotope storage behavior of $\text{ZrCo}_{1-x}\text{Ni}_x$ alloys, **Ram Avtar Jat**, S.C. Parida, Renu Agarwal, A.R. Joshi and K.L. Ramakumar, 19th DAE-BRNS International Symposium & Workshop on Thermal Analysis, THERMANS-2013, December 19-21, 2013, Bhabha Atomic Research Centre, Mumbai, India, pp. 141.
5. Hydrogen storage behavior of $\text{ZrCo}_{1-x}\text{Ni}_x$ alloys, **Ram Avtar Jat**, S.C. Parida, Renu Agarwal, S.G. Kulkarni, DAE-BRNS 4th Interdisciplinary Symposium on Materials Chemistry (ISMC), December 11-15, 2012, Bhabha Atomic Research Centre, Mumbai, India, pp. 150-151.
6. Hydrogen sorption-desorption studies on ZrCo-Hydrogen system, **Ram Avtar Jat**, S.C. Parida, Renu Agarwal and S.G. Kulkarni, 18th DAE-BRNS International Symposium & Workshop on Thermal Analysis, THERMANS-2012, January 31-February 4, 2012, Bhabha Atomic Research Centre, Mumbai, India, pp. 350.

BARC News Letter: 02 (Conference award papers)

1. Hydrogen isotope storage behavior of $\text{ZrCo}_{1-x}\text{Ni}_x$ alloys, **Ram Avtar Jat**, S.C. Parida, Renu Agarwal, A.R. Joshi and K.L. Ramakumar, BARC News Letter, Founders Day Special Issue, October 2014, 201-204.
2. Hydrogen sorption-desorption studies on ZrCo-Hydrogen system, **Ram Avtar Jat**, S.C. Parida, Renu Agarwal and S.G. Kulkarni; BARC News Letter, Founders Day Special Issue, October 2013, 295-299.



(Ram Avtar Jat)

DEDICATED
TO MY PARENTS



ACKNOWLEDGEMENTS

The realization of this thesis was accomplished with the contribution of many people to whom I would like to show my greatest appreciation. I would like to express my heartfelt gratitude and regards to my supervisors, Dr. Renu Agarwal and Dr. S.C. Parida for their guidance, support and encouragement in fulfilling this work from conception to worthy completion. In no less measure, I want to thank late Shri Bhaskar Sen, Ex-Head, PDD, whose motivations helped me a lot and his memory will be eternal.

I extend my gratitude to Dr. S.K. Mukerjee, Head PDD, for his continuous help in this process. I offer my thanks to Prof. K.L. Ramakumar, Director RC&I Group for his invaluable mentoring.

I wish to acknowledge the Doctoral Committee Chairman, Prof. B.S. Tomar and members Prof. S. Kannan and Dr. Smruti Dash for their crucial guidance and support in completion of this work. I also acknowledge Dr. Amitabh Das and Shri Ripandeep Singh for their extended help in Neutron diffraction and Rietveld refinement of diffraction data. I would like to thank Shri Subhasis Pati, SRF, PDD for his co-operation and help during the experiments and data analysis. I sincerely acknowledge the contributions of Dr. P.U. Sastry, Dr. A.K. Tyagi, Shri Santu Kaity and Shri Jitendra Nuwad who were kind in extending the facilities for characterization of materials.

I am also thankful to Dr. V. Venugopal, Dr. Ziley Singh, Dr. A.R. Joshi, Shri S.G. Kulkarni, Shri S.P. Hasilkar, Dr. Y.P. Naik, Dr. S.K. Rakshit, Shri Pradeep Samui, Shri D. Chattaraj, Shri. N.S. Anand, Shri. S.G. Sawant and all the members of PDD for their kindness and gracious assistance.

I wish to express my sincere thanks to my friends Shri Kartikey Kumar Yadav, Dr. Sanghamitra Chatterjee and Shri B.M. Tripathi for their moral support and constant positivity when it was needed. It is a great pleasure for me to acknowledge the contributions of all the persons and institutions who have helped me directly and indirectly in this memorable journey.

I am eternally grateful to my parents, my wife Deepika, younger brother Bhagchand and daughter Urvashee for all the love, trust, support and encouragement. Their great influence made me who I am today.

Last but most important, I am thankful to almighty for his blessings on me.

CONTENTS

| | |
|--|-----|
| SYNOPSIS..... | i |
| LIST OF FIGURES | xi |
| LIST OF TABLES | xvi |
| CHAPTER 1: INTRODUCTION | 1 |
| 1.1 Energy demand-Fusion energy..... | 2 |
| 1.2 International Thermonuclear Experimental Reactor (ITER) | 7 |
| 1.3 Hydrogen and its isotopes | 10 |
| 1.4 Storage methods for hydrogen isotopes | 12 |
| 1.4.1 Gaseous storage: High pressure gas cylinders | 13 |
| 1.4.2 Liquid storage..... | 13 |
| 1.4.3 Solid storage | 13 |
| 1.5 Solid state storage of hydrogen isotopes | 14 |
| 1.5.1 Theory of metal-hydrogen interaction..... | 15 |
| 1.5.2 Thermodynamics of Metal-Hydrogen system..... | 18 |
| 1.5.3 Selection of suitable metal/alloys for solid state storage | 22 |
| 1.6 Hydrogen Isotope effect | 24 |
| 1.7 Materials for hydrogen isotope storage and challenges | 28 |
| 1.8 Motivation and Objective of the present investigation | 33 |
| CHAPTER 2: EXPERIMENTAL..... | 34 |
| 2.1 Synthesis of materials..... | 35 |
| 2.1.1 Preparation of alloys: Arc melting method | 35 |
| 2.1.2 Activation of alloys | 36 |
| 2.1.3 Preparation of hydrides/deuterides | 37 |

| | | |
|--|--|----|
| 2.2 | Characterization techniques | 38 |
| 2.2.1 | X-Ray Diffraction (XRD) Technique..... | 38 |
| 2.2.2 | Scanning Electron Microscope (SEM)..... | 39 |
| 2.2.3 | Energy-dispersive X-ray spectroscopy (EDS) and Elemental mapping | 41 |
| 2.2.4 | Neutron powder diffraction (NPD) technique..... | 41 |
| 2.2.5 | Data treatment method | 44 |
| 2.3 | Hydrogen absorption-desorption measurement technique..... | 46 |
| 2.4 | Pressure-Composition-Temperature (PCT) studies | 49 |
| 2.4.1 | Calculation of hydrogen/deuterium absorption/desorption quantities in Sieverts' method | 51 |
| 2.5 | Cyclic life studies | 53 |
| 2.6 | Isothermal disproportionation studies | 53 |
| CHAPTER 3: RESULTS AND DISCUSSION..... | | 55 |
| 3.1 | Storage Behavior of ZrCo Alloy | 56 |
| 3.1.1 | Material Characterization..... | 56 |
| 3.1.2 | Standardization of Sieverts' apparatus with PCT measurements on Pd-H ₂ system..... | 59 |
| 3.1.3 | Pressure-Composition-Temperature measurements on ZrCo-H ₂ /D ₂ systems.... | 60 |
| 3.2 | Storage behavior of ZrCo _{1-x} Ni _x alloys | 65 |
| 3.2.1 | Materials Characterization | 65 |
| 3.2.2 | Pressure-Composition-Temperature measurements on ZrCo _{1-x} Ni _x -H ₂ /D ₂ systems | 71 |
| 3.2.3 | Hydrogen absorption-desorption cyclic life studies..... | 77 |
| 3.3 | Storage behavior of ZrCo _{0.9} Fe _{0.1} alloy | 81 |
| 3.3.1 | Materials Characterization | 81 |

| | |
|---|-----|
| 3.3.2 Pressure-Composition-Temperature measurements on $\text{ZrCo}_{0.9}\text{Fe}_{0.1}\text{-H}_2/\text{D}_2$ systems | 85 |
| 3.3.3 Hydrogen absorption-desorption cyclic life studies | 89 |
| 3.4 Storage behavior of $\text{Zr}_{1-x}\text{Ti}_x\text{Co}$ alloys | 93 |
| 3.4.1 Materials Characterization | 93 |
| 3.4.2 Pressure-Composition-Temperature measurements on $\text{Zr}_{1-x}\text{Ti}_x\text{Co-H}_2/\text{D}_2$ systems | 98 |
| 3.5 Structural studies on Zr-Co-M deuterides | 105 |
| 3.5.1 Neutron diffraction studies on $\text{ZrCo}_{1-x}\text{Ni}_x$ deuterides | 105 |
| 3.5.2 Neutron diffraction studies on $\text{ZrCo}_{0.9}\text{Fe}_{0.1}$ deuteride | 111 |
| 3.5.3 Neutron diffraction studies on $\text{Zr}_{1-x}\text{Ti}_x\text{Co}$ deuterides | 115 |
| 3.6 Isothermal disproportionation behavior of Zr-Co-M ternary alloys | 119 |
| CHAPTER 4: SUMMARY AND CONCLUSION | 124 |
| REFERENCES: | 130 |

SYNOPSIS

Tritium (^3H or T) is a radioactive isotope of hydrogen and is a component of fuel for fusion reactor. The safe storage, transport and delivery of tritium demand a suitable solid state storage medium. Uranium is conventionally used for this purpose due to many favorable properties. However, development of alternate tritium storage materials is a mainstream of research today among the fusion science community. The intermetallic compound ZrCo has been investigated largely as a suitable candidate material for storage, supply and recovery of hydrogen isotopes in various tritium handling facilities like International Thermonuclear Experimental Reactor (ITER) because of its non-radioactive nature, non-pyrophoricity at room temperature and tritium storage properties similar to uranium. ZrCo has a favorable hydrogen isotope ($X = ^1\text{H}$, ^2H or ^3H) absorption capacity (X/ZrCo up to 3) with maximum stoichiometry of ZrCoX_3 . However, ZrCo is prone to hydrogen induced disproportionation upon repeated hydriding-dehydriding cycles. Disproportionation reaction forms a more stable hydride ZrX_2 and hydrogen non-absorptive metallic compound ZrCo_2 which results in loss of its hydrogen isotope recovery and storage abilities.

This has led to the onset of consolidated efforts to find a suitable ternary alloy for storage, supply and recovery of hydrogen isotopes. In the present thesis, a systematic approach has been applied to investigate the effect of ternary alloying on the hydrogen isotope storage properties of ZrCo alloy. Ternary alloys $\text{Zr}_{1-x}\text{Ti}_x\text{Co}$ and $\text{ZrCo}_{1-x}\text{M}_x$ ($\text{M} = \text{Ni}$ and Fe) were prepared and characterized. The hydrogen isotope storage behavior of Zr-Co-M ternary alloys was systematically investigated by employing Sieverts' type volumetric apparatus. The thermodynamic parameters of the hydrogenation reactions and their corresponding isotopic effects were evaluated. Hydrogen induced disproportionation behavior of Zr-Co-M ternary alloys was investigated by hydrogen absorption-desorption cyclic life and isothermal studies.

The phenomenon of hydrogen induced disproportionation in different Zr-Co-M ternary alloys was further investigated by employing neutron powder diffraction (NPD) technique. The extensive work carried out in this thesis enable to identify a suitable ternary substituent for effective storage, supply and recovery of hydrogen isotopes in particular tritium.

This thesis is divided into four chapters as outlined below.

Chapter 1: Introduction; Chapter 2: Experimental methods; Chapter 3: Results and Discussion and Chapter 4: Summary and Conclusion

A brief outline of each chapter is described below.

Chapter 1: Introduction

This chapter deals with the brief introduction about the energy demand and use of nuclear fusion as a source of energy. The properties of different hydrogen isotopes are presented and different methods of storage of hydrogen isotopes are discussed. Solid state storage of hydrogen isotopes and isotope effect on hydrogen storage properties of materials are presented. Thermodynamics of metal-hydrogen interaction is also explained. A brief overview about the materials for solid state storage of hydrogen isotopes is presented. Lastly the aim and scope of the present thesis is addressed.

Solid state storage of tritium in the form of metal tritide is considered as the most safest method in fusion technology and hence is being adapted in International Thermonuclear Experimental Reactor (ITER) program [1]. Intermetallic compounds that have very low equilibrium pressure over tritides at room temperature and high dissociation pressure at moderate temperature, for recovery of absorbed gas with minimal permeation losses, are of prime importance for this application. In this context, uranium is extensively used for storage, supply and recovery of tritium. Despite favorable storage properties, uranium has the drawbacks of restrictive use due to its radioactive and pyrophoric nature [2]. For these reasons, there is a need for an alternate material development which can substitute the

uranium. In the search of alternate materials, as a substitute for uranium, substantial progress has been made in recent years such as development of uranium and zirconium based alloys [U-Ti, U-Zr, Zr-Co, Zr-Ni] which show improved properties over pure uranium metal. Among these, ZrCo alloy has been extensively investigated for its use in ITER program.

The intermetallic compound ZrCo seems to be a suitable candidate material for storage, supply and recovery of hydrogen isotopes as it is non-radioactive and non-pyrophoric at room temperature and has similar tritium storage properties as that of uranium [3]. It is reported that ZrCo can absorb hydrogen at room temperature to form the hydride with a maximum stoichiometry of ZrCoX_3 [3]. However, it has been reported [4] that upon repeated hydriding-dehydriding cycles, the hydrogen storage capacity of ZrCo decreases, which is attributed to the following disproportionation reaction:



The hydrogen induced disproportionation results in the formation of a hydrogen non-absorbing ZrCo_2 and a very stable ZrX_2 hydride phases. Since, decomposition of ZrX_2 requires much higher temperature ($> 973 \text{ K}$) than that of ZrCo-hydride, a significant amount of hydrogen gets trapped within the storage material. This results in reduction of hydrogen storage capacity of ZrCo, which is not desirable for its use in ITER SDS. Konishi et al. [5] have reported that the extent of disproportionation can be suppressed by decreasing the dehydriding temperature. However, decreasing the dehydriding temperature lowers the hydrogen equilibrium pressure of ZrCo- H_2 system due to which the required delivery pressure of 100 kPa of hydrogen couldn't be achieved. Hence, the alternative choice is to thermodynamically stabilize the hydride phase (ZrCoX_3) by suitable ternary alloying with another element (M) and maintaining the equilibrium pressure (p_{X_2}) closer to 100 kPa at lower temperature which in turn will reduce the extent of disproportionation reaction. The suitable alloying element M will elevate the desorption equilibrium hydrogen pressure compared to the parent compound ZrCoX_3 at a particular temperature. Then, it is possible to

deliver the required pressure of 100 kPa of hydrogen with reduced desorption temperature, thereby preventing the extent of disproportionation.

Considering the above mentioned drawbacks of binary metallic hydrides, efforts have been made to improve the hydrogen storage behavior of ZrCo-H₂ system by ternary alloying. Limited studies are reported in literature on the effect of ternary alloying on the hydrogen storage behavior of ZrCo based alloys [6, 7]. Hence, in the present study we have thoroughly investigated the effect of ternary elements on the hydrogen isotope storage behavior of ZrCo alloy by generating the hydrogen/deuterium desorption pressure-composition isotherms (PCIs) and studying their hydrogen induced disproportionation behavior. Further, structural studies are employed to explain the hydrogen induced disproportionation behavior of Zr-Co-M ternary alloys.

Chapter 2: Experimental

This chapter deals with the experimental techniques employed in the present investigation. It describes preparation and characterization of materials, the principles of experimental methods used to investigate the hydrogen isotope storage properties of Zr-Co-M ternary alloys.

Alloys of compositions ZrCo_{1-x}Ni_x ($x = 0.0, 0.1, 0.2$ and 0.3), ZrCo_{0.9}Fe_{0.1} and Zr_{1-x}Ti_xCo ($x = 0.1, 0.2$ and 0.3) were prepared by arc-melting method and characterized by different techniques like XRD, SEM, EDS and Elemental mapping. Prior to hydrogen isotope storage behavior investigations, the alloy samples were activated by hydriding-dehydriding method. For this purpose, a Sievert's type volumetric apparatus was indigenously designed, developed and fabricated. The pressure-composition-temperature (PCT) measurements were carried out using a conventional Sievert's type volumetric apparatus (PCT Pro-2000, SETARAM Instrumentation, France). Hydrogen/deuterium desorption Pressure-Composition isotherms (PCIs) for all the systems were generated in the temperature range of 523-603 K with a step

of 20 K. Hydrogen absorption-desorption cyclic life studies on $\text{ZrCo}_{1-x}\text{Ni}_x$ and $\text{ZrCo}_{0.9}\text{Fe}_{0.1}$ alloys were carried out at 583 K and up to 50 cycles using the Sievert's type volumetric apparatus. These studies were not performed on the $\text{Zr}_{1-x}\text{Ti}_x\text{Co}$ alloys due to their higher desorption equilibrium pressure of hydrogen at 583 K.

The isothermal disproportionation studies of all Zr-Co-M ternary alloys were carried out at 750 K (maximum possible desorption temperature) for 10 hrs under delivery conditions, above 1 bar over pressure of hydrogen. The Zr-Co-M hydrides before and after disproportionation studies were characterized by XRD to see the phase changes during the course of isothermal conditions.

Neutron powder diffraction (NPD) patterns of Zr-Co-M ternary alloy deuterides were recorded on a multi position sensitive detector (PSD) based neutron powder diffractometer ($\lambda = 1.2443\text{\AA}$) at Dhruva reactor, Bhabha Atomic Research Centre, Mumbai, India. The NPD patterns were analyzed using FULLPROF program [8] to investigate the effect of ternary alloying on the structural properties.

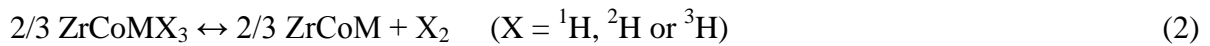
Chapter 3: Results and Discussion

This chapter deals with results and discussion part of the present investigation.

The X-ray diffraction patterns of Zr-Co-M ternary alloys confirm the formation of single b.c.c. (CsCl type) phase (space group $Pm-3m$) similar to ZrCo. A trace amount of ZrCo_2 impurity phase is also present in all the alloys which is in line with the observation of Harris et al. [9] that a single phase of ZrCo is extremely difficult to prepare and is always accompanied by the formation of traces of ZrCo_2 phase. Similarly, the XRD analysis of ternary alloy hydrides/deuterides revealed the formation of single orthorhombic phase (space group $Cmcm$) similar to ZrCoH_3 . Further, the lattice parameters and phase abundances of the alloys were calculated by Rietveld refinement of XRD data using the FULLPROF program [8]. The SEM images of alloys and the hydrides infer that the alloys exhibit a cleavage type

surface, whereas the hydride phases show a cleavage type fracture surface. The cracks generated in the hydride phase are attributed to the lattice expansion of alloy upon hydrogenation. The EDS microanalysis carried out at different morphological positions of the alloy reveals an average composition over the entire sample which is in accordance with the nominal composition of the alloys. The elemental mapping images of alloys reveal the homogeneous nature of the material.

The hydrogen/deuterium desorption pressure-composition isotherms (PCIs) of $\text{ZrCo}_{1-x}\text{Ni}_x\text{-H}_2/\text{D}_2$ ($x = 0, 0.1, 0.2$ and 0.3), $\text{ZrCo}_{0.9}\text{Fe}_{0.1}\text{-H}_2/\text{D}_2$ and $\text{Zr}_{1-x}\text{Ti}_x\text{Co-H}_2/\text{D}_2$ ($x = 0.1, 0.2$ and 0.3) systems were generated in the temperature range of 524-603 K using Sievert's type volumetric apparatus. It is evident from PCIs that in the temperature range of investigation, a single desorption plateau is observed for all the isotherms and the plateau width found to decrease with increase in temperature. The reaction involved in de-hydrogenation/de-deuteration of Zr-Co-M hydrides/deuterides which results in single desorption plateau for all the isotherms can be written as;



The temperature dependence of the equilibrium plateau pressure of hydrogen/deuterium was found to be best represented by the van't Hoff plot. A van't Hoff plot was constructed using the plateau pressure data and the thermodynamic parameters, like enthalpy and entropy change, for hydrogen/deuterium desorption reactions (at the average experimental temperature of 563 K) were calculated using the van't Hoff equation, given below.

$$\ln(P/P^0) = -\Delta_r H/RT + \Delta_r S/R \quad (3)$$

where, $\Delta_r H$ and $\Delta_r S$ are the enthalpy and entropy changes for the dehydrogenation/de-deuteration reaction as mentioned above in Eq. (2). P^0 is the standard pressure.

For the practical application of these materials in hydrogen isotope handling facilities, it is essential to know the desorption temperature for the release of 100 kPa of hydrogen. From the van't Hoff relations, the hydrogen/deuterium desorption temperature (T_{des}) for all the

alloys were calculated. It is evident that the T_{des} decreases with increase in Ni or Ti content and increases with the addition of Fe. It can be seen from Eq. (3) that the hydrogen isotope effect on the equilibrium pressure of hydrogen/deuterium depends on the values of enthalpy and entropy changes for a particular reaction involved. In order to interpret the hydrogen isotope effect on the storage behavior of Zr-Co-M ternary alloys, the thermodynamic parameters obtained for hydrides were compared with those of deuterides. This comparison revealed that all ternary alloys show normal hydrogen isotope effect where the equilibrium pressure of D_2 is higher than that of H_2 at all experimental temperatures. Based on these observations, it is expected that at the operating conditions of hydrogen isotope handling facilities, the equilibrium pressure of tritium, deuterium and hydrogen will follow the order of $p(\text{T}_2) > p(\text{D}_2) > p(\text{H}_2)$ for all ternary alloys.

It is evident from the absorption-desorption cyclic life studies on $\text{ZrCo}_{1-x}\text{Ni}_x$ and $\text{ZrCo}_{0.9}\text{Fe}_{0.1}$ alloys that the hydrogen absorption capacity (H/f.u.) at 583 K for ZrCo and $\text{ZrCo}_{0.9}\text{Ni}_{0.1}$ alloys decrease substantially up to 10 repeated cycles after which it remains almost constant. For the alloys of compositions $\text{ZrCo}_{0.8}\text{Ni}_{0.2}$ and $\text{ZrCo}_{0.7}\text{Ni}_{0.3}$, the absorption capacity decreases slightly up to 3 repeated cycles after which there is small gradual decrease in H/f.u. up to 50 cycles. However, for $\text{ZrCo}_{0.9}\text{Fe}_{0.1}$ alloy the hydrogen absorption capacity (H/f.u.) at 583 K decreases significantly up to 5th absorption-desorption cycle after which it remains almost constant. The XRD patterns of the hydride phases after 50th cycles reveal that the hydrides of all the alloys form a small fraction of ZrCo_2 and ZrH_2 along with major ZrCoH_3 . Hence, it can be inferred that hydrogen absorption-desorption cycles results in disproportionation according to reaction (1). The crystallite sizes of hydrides before and after 50th cycle are calculated by using the Scherrer formula. It is observed that upon cycling the crystallite size decreases significantly for ZrCo and $\text{ZrCo}_{0.9}\text{Ni}_{0.1}$ and marginally for $\text{ZrCo}_{0.9}\text{Fe}_{0.1}$. On the other hand, the change in crystallite size before and after cyclic life studies is very small for $\text{ZrCo}_{0.8}\text{Ni}_{0.2}$ and $\text{ZrCo}_{0.7}\text{Ni}_{0.3}$ alloys.

In order to find the best suitable ternary alloy among the alloys studied, it is required to perform the isothermal disproportionation studies under delivery conditions. The isothermal disproportionation behavior of ternary alloys, at 750 K for 10 hours under the over pressure of hydrogen above 1 bar, reveals that Ni and Fe catalyse the disproportionation reaction in its ternary alloys. The disproportionation rate was found to be slower in Fe substituted alloy as compared to observed in Ni substituted alloys. It is evident that among all ternary alloys studied the $Zr_{1-x}Ti_xCo$ ($x=0.1, 0.2$ and 0.3) alloys found to have higher durability against hydrogen induced disproportionation.

In order to explain the hydrogen induced disproportionation behavior of Zr-Co-M ternary alloys, it is desirable to study the interstitial site occupancies of hydrogen via direct experimental technique like neutron powder diffraction (NPD). Owing to high incoherent scattering nature of hydrogen atom, it was not possible to perform the neutron powder diffraction experiments with hydrides. Therefore, the NPD experiments were carried out on ternary alloy deuterides. Rietveld refinement of neutron diffraction data was carried out by varying the background, occupancies and position of atoms. Since the structures of both $ZrCoH_3$ and $ZrNiH_3$ are same [10], this gives a clue that difference between hydrogen storage properties may be because of different hydrogen occupancy in these hydrides. The deuterium atoms are allowed to occupy $8f_2$ and $8e$ sites in addition to the earlier reported [10], $4c_2$ and $8f_1$ sites. A significant reduction in χ^2 was observed with addition of these extra sites for deuterium occupation. It was observed that among $8f_2$ and $8e$ sites the deuterium occupies only $8e$ sites. This observation is in agreement with the Switendick criterion [11], which also prohibits the simultaneous occupation of both $8f_2$ and $8e$ sites as the H-H distance between these two sites is too small ($\sim 1.3\text{\AA}$). It is evident that for $ZrCoD_3$ the occupancy of $8e$ site is $\sim 3.8\%$ which is in accord with the prediction of Bekris et al. [12]. Based on these observations, the crystal structure of $ZrCoD_3$ with new deuterium site ($8e$) is proposed. Systematic investigations on all ternary alloy deuterides establish the effect of ternary

alloying on the occupancy of new 8e site and Zr-D distance. It is evident that $Zr_{0.8}Ti_{0.2}Co$ has the lowest occupancy of new 8e site among the alloys studied.

Considering the hydrogen isotope storage behavior, hydrogen induced disproportionation and structural studies on different Zr-Co-M (M = Ni, Fe and Ti) ternary alloys, it is proposed that the $Zr_{0.8}Ti_{0.2}Co$ alloy is a suitable ternary alloy as a substitute for the conventionally used highly pyrophoric uranium bed for tritium storage applications.

Chapter 4: Summary and Conclusion

This chapter deals with the summary and conclusion arrived from the work carried out in the present investigation.

The X-ray diffraction patterns of prepared alloys $ZrCo$, $ZrCo_{1-x}Ni_x$ ($x = 0.1, 0.2$ and 0.3), $ZrCo_{0.9}Fe_{0.1}$ and $Zr_{1-x}Ti_xCo$ ($x = 0.1, 0.2$ and 0.3) confirm the formation of b.c.c. phase similar to $ZrCo$, along with a small fraction of $ZrCo_2$ as impurity phase. Hydrogen/deuterium desorption pressure-composition isotherms (PCIs) of all the alloys show a single desorption plateau. Investigation of thermodynamic parameters like enthalpy and entropy of hydrogen/deuterium desorption reactions in these alloys show normal hydrogen isotope effect wherein the equilibrium pressure of deuterium is higher than that of hydrogen at all experimental temperatures. Considering the PCT studies, hydrogen induced disproportionation studies and structural studies, it is proposed that among the alloys investigated, $Zr_{0.8}Ti_{0.2}Co$ alloy is the best suitable non-pyrophoric and non-radioactive ternary alloy as a substitute for the conventionally used highly pyrophoric uranium bed for tritium storage applications. This alloy has potential for its use in ITER facility for storage, supply and recovery of hydrogen isotopes.

References:

- [1] Ortman MS, Warren TJ, Smith DJ. Use of metal hydrides for handling tritium. Fusion Technol. 1985;8:2330-2336.

- [2] Longhurst GR. Pyrophoricity of tritium-storage bed materials. *Fusion Technol.* 1998;14:750-755.
- [3] Willin E, Sirch M, Penzhorn RD, Devillers M. Metal getters for tritium storage. *Fusion Technol.* 1988;14:756-763.
- [4] Devillers M, Sirch M, Penzhorn RD. Hydrogen-induced disproportionation of the intermetallic compound ZrCo. *Chem Mater.* 1992;4:631–639.
- [5] Konishi S, Nagasaki T, Okuno K. Reversible disproportionation of ZrCo under high temperature and hydrogen pressure. *J Nucl Mater.* 1995;223:294–299.
- [6] Zhuo H, Xiaopeng L, Lijun J, Shumao W. Hydrogen storage properties of $Zr_{1-x}Ti_xCo$ intermetallic compound. *Rare Metals.* 2006;25:200-203.
- [7] Gongli T, Xiaopeng L, Lijun J, Shumao W, Zhinian L, Hualing L. Dehydrogenation characteristic of $Zr_{1-x}M_xCo$ (M=Hf, Sc) alloy. *Trans Nonferrous Met Soc China.* 2007;17:s949-953.
- [8] Rodriguez-Carvajal J. FULLPROF: A program for rietveld refinement and pattern matching analysis. Abstracts of the Satellite Meeting on Powder Diffraction of the XVthIUCr Congress, Toulouse, France.1990;p.127.
- [9] Harris IR, Hussain D, Barraclough KG. The constitution of the binary equiatomic alloys of Zr with Fe, Co and Ni. *Scr Metall.* 1970;4:305-308.
- [10] Irodova AV, Somenkov VA, Shil'shtein SS, Padurets LN, Chertkov AA. Structure of $ZrCoD_3$. *Sov Phys Crystallogr.* 1978;23:591-592.
- [11] Switendick AC. Theoretical Study of Hydrogen in Metals: Current Status and Further Prospects. SAND,1978,78-0250.
- [12] Bekris N, Sirch M. On the Mechanism of the Disproportionation of ZrCo Hydrides. *Fusion Sci Technol.* 2012;62:50-55.

LIST OF FIGURES

| | |
|---|----|
| Figure 1.1: Plot of the fusion reactivity (average of cross-section times relative speed of reacting nuclei) vs. temperature for three common reactions [7]..... | 4 |
| Figure 1.2: Schematic of D-T fusion reaction [5]..... | 5 |
| Figure 1.3: ITER Tokamak Cutaway [13]. | 8 |
| Figure 1.4: Schematic of proposed nuclear fusion power plant based on D-T fusion for electricity generation [15]. | 9 |
| Figure 1.5: Lennard-Jones potential energy diagram for chemisorptions of hydrogen in metals (Reprinted from [24], Copyright (2003), with permission from Elsevier)..... | 16 |
| Figure 1.6: Reaction steps for the (a) absorption and (b) desorption of hydrogen by a spherical metal/hydride powder particle (α -phase: Solid solution of hydrogen in metal)..... | 18 |
| Figure 1.7: Schematic of pressure-composition isotherms (PCIs) and van't Hoff plot (Reprinted from [24], Copyright (2003), with permission from Elsevier)..... | 20 |
| Figure 1.8: Schematic diagram of hysteresis in a absorption-desorption PCI..... | 21 |
| Figure 1.9: Schematic potential energy curve for the hydrogen molecules [16], Figure not to scale..... | 25 |
| Figure 1.10: The Schematic comparison of the zero-point vibrational energies of hydrogen isotopes in (a) octahedral and (b) tetrahedral interstitial position with that of gas phase molecules (Reprinted from [39], Copyright (1984), with permission from Elsevier). | 26 |
| Figure 2.1: Schematic and the instrument parameters of neutron powder diffractometer..... | 43 |
| Figure 2.2: Schematic diagram of a Sieverts' type volumetric apparatus. | 47 |
| Figure 2.3: Indigenously designed and developed Sieverts' type volumetric apparatus. | 48 |

| | |
|---|----|
| Figure 2.4: Sieverts' type volumetric apparatus (PCT Pro-2000). | 48 |
| Figure 2.5: Generation of hydrogen desorption PCI for ZrCo alloy..... | 51 |
| Figure 3.1: X-ray powder diffraction patterns of ZrCo and its hydride/deuteride..... | 56 |
| Figure 3.2: Rietveld refinement of XRD pattern of ZrCo alloy. The tick marks indicate ZrCo (top) and ZrCo ₂ (bottom) phases..... | 57 |
| Figure 3.3: SEM images of ZrCo and its hydride at magnifications of 500X and 5000X; (a) and (b) ZrCo alloy; (c) and (d) ZrCo hydride phase. | 58 |
| Figure 3.4: EDX spectra of ZrCo alloy..... | 58 |
| Figure 3.5: (a) Hydrogen desorption PCIs and (b) van't Hoff plot for Pd-H ₂ system | 60 |
| Figure 3.6: Hydrogen/deuterium PCIs for (a) ZrCo-H ₂ and (b) ZrCo-D ₂ systems..... | 61 |
| Figure 3.7: Comparison of van't Hoff plot obtained in this study with those reported in literature for the desorption isotherms of (a) ZrCo-H ₂ and (b) ZrCo-D ₂ systems | 62 |
| Figure 3.8: X-ray diffraction patterns of ZrCo _{1-x} Ni _x alloys: (a) $x = 0$, (b) $x = 0.1$, (c) $x =$ 0.2 and (d) $x = 0.3$ | 65 |
| Figure 3.9: Rietveld refinement of X-ray diffraction pattern of ZrCo _{0.9} Ni _{0.1} alloy. The tick marks indicate ZrCo (top) and ZrCo ₂ (bottom) phases | 66 |
| Figure 3.10: X-ray diffraction patterns of hydrides of ZrCo _{1-x} Ni _x alloys: (a) $x = 0$, (b) x $= 0.1$, (c) $x = 0.2$ and (d) $x = 0.3$ | 68 |
| Figure 3.11: X-ray diffraction patterns of deuterides of ZrCo _{1-x} Ni _x alloys: (a) $x = 0$, (b) $x = 0.1$, (c) $x = 0.2$ and (d) $x = 0.3$ | 68 |
| Figure 3.12: SEM images of ZrCo _{1-x} Ni _x alloys at magnifications of 5000X: (a) $x = 0$, (b) $x = 0.1$, (c) $x = 0.2$, (d) $x = 0.3$, (e) & (f) hydride of ZrCo at magnifications of 5000X and 10000X, respectively | 69 |
| Figure 3.13: Elemental mapping images of ZrCo _{0.9} Ni _{0.1} alloy. | 70 |

| | |
|---|----|
| Figure 3.14: Hydrogen desorption pressure-composition isotherms for $\text{ZrCo}_{1-x}\text{Ni}_x\text{-H}_2$ systems: (a) $x = 0$, (b) $x = 0.1$ (c) $x = 0.2$ and (d) $x = 0.3$ | 71 |
| Figure 3.15: Deuterium desorption pressure-composition isotherms for $\text{ZrCo}_{1-x}\text{Ni}_x\text{-D}_2$ systems: (a) $x = 0$, (b) $x = 0.1$ (c) $x = 0.2$ and (d) $x = 0.3$ | 72 |
| Figure 3.16: van't Hoff plots for $\text{ZrCo}_{1-x}\text{Ni}_x\text{-H}_2/\text{D}_2$ systems | 73 |
| Figure 3.17: Variation of T_{des} with Ni content in $\text{ZrCo}_{1-x}\text{Ni}_x$ alloys | 76 |
| Figure 3.18: Effect of hydrogen absorption-desorption cycles on the storage capacity of $\text{ZrCo}_{1-x}\text{Ni}_x$ alloys at 583 K | 77 |
| Figure 3.19: X-ray diffraction patterns of hydride phases after 50 th cycles: (a) $x = 0$, (b) $x = 0.1$, (c) $x = 0.2$ and (d) $x = 0.3$ | 78 |
| Figure 3.20: X-ray diffraction patterns of de-hydrated phases after 50 th cycle: (a) $x = 0$, (b) $x = 0.1$, (c) $x = 0.2$ and (d) $x = 0.3$ | 80 |
| Figure 3.21: X-ray diffraction pattern of $\text{ZrCo}_{0.9}\text{Fe}_{0.1}$ alloy, its hydride and deuteride | 81 |
| Figure 3.22: Rietveld refinement of X-ray diffraction pattern of $\text{ZrCo}_{0.9}\text{Fe}_{0.1}$ alloy. The tick marks indicate ZrCo (top) and ZrCo_2 (bottom) phases | 82 |
| Figure 3.23: SEM images of (a) $\text{ZrCo}_{0.9}\text{Fe}_{0.1}$ alloy at magnifications of 1000x, (b) & (c) hydride of $\text{ZrCo}_{0.9}\text{Fe}_{0.1}$ at magnifications of 1000x and 5000x, respectively | 84 |
| Figure 3.24: EDS spectra of $\text{ZrCo}_{0.9}\text{Fe}_{0.1}$ alloy | 84 |
| Figure 3.25: Elemental mapping images of $\text{ZrCo}_{0.9}\text{Fe}_{0.1}$ alloy | 85 |
| Figure 3.26: Hydrogen/deuterium desorption pressure-composition isotherms for (a) $\text{ZrCo}_{0.9}\text{Fe}_{0.1}\text{-H}_2$ and (b) $\text{ZrCo}_{0.9}\text{Fe}_{0.1}\text{-D}_2$ systems | 86 |
| Figure 3.27: van't Hoff plots for $\text{ZrCo}_{0.9}\text{Fe}_{0.1}\text{-H}_2/\text{D}_2$ systems | 87 |
| Figure 3.28: Effect of hydrogen absorption-desorption cycles on the storage capacity of $\text{ZrCo}_{0.9}\text{Fe}_{0.1}$ and ZrCo alloys at 583 K | 90 |
| Figure 3.29: X-ray diffraction patterns of $\text{ZrCo}_{0.9}\text{Fe}_{0.1}$ hydride phase after 50 th cycle | 91 |

| | |
|--|-----|
| Figure 3.30: X-ray diffraction patterns of $Zr_{1-x}Ti_xCo$ alloys: (a) $x = 0$, (b) $x = 0.1$, (c) $x = 0.2$ and (d) $x = 0.3$ | 93 |
| Figure 3.31: Rietveld refinement of X-ray diffraction pattern of $Zr_{0.8}Ti_{0.2}Co$ alloy. The tick marks indicate $ZrCo$ (top) and $ZrCo_2$ (bottom) phases | 94 |
| Figure 3.32: X-ray diffraction patterns of hydrides of $Zr_{1-x}Ti_xCo$ alloys: (a) $x = 0$, (b) $x = 0.1$, (c) $x = 0.2$ and (d) $x = 0.3$ | 95 |
| Figure 3.33: X-ray diffraction patterns of deuterides of $Zr_{1-x}Ti_xCo$ alloys: (a) $x = 0$, (b) $x = 0.1$, (c) $x = 0.2$ and (d) $x = 0.3$ | 96 |
| Figure 3.34: SEM images of (a) $Zr_{1-x}Ti_xCo$ alloy at magnifications of 1000x, (b) & (c) hydride of $Zr_{1-x}Ti_xCo$ at magnifications of 1000x and 5000x, respectively. | 97 |
| Figure 3.35: EDX spectra of $Zr_{0.9}Ti_{0.1}Co$ alloy | 97 |
| Figure 3.36: Elemental mapping images of $Zr_{0.9}Ti_{0.1}Co$ alloy. | 98 |
| Figure 3.37: Hydrogen desorption pressure-composition isotherms for $Zr_{1-x}Ti_xCo-H_2$ systems: (a) $x = 0$, (b) $x = 0.1$ (c) $x = 0.2$ and (d) $x = 0.3$ | 99 |
| Figure 3.38: Deuterium desorption pressure-composition isotherms for $Zr_{1-x}Ti_xCo-D_2$ systems: (a) $x = 0$, (b) $x = 0.1$ (c) $x = 0.2$ and (d) $x = 0.3$ | 100 |
| Figure 3.39: van't Hoff plots for (a) $Zr_{1-x}Ti_xCo-H_2$ and (b) $Zr_{1-x}Ti_xCo-D_2$ systems. | 101 |
| Figure 3.40: Rietveld refinement of X-ray diffraction pattern of $ZrCo_{0.9}Ni_{0.1}D_3$ | 107 |
| Figure 3.41: Rietveld refinement of neutron diffraction pattern of $ZrCo_{0.8}Ni_{0.2}D_3$ | 108 |
| Figure 3.42: The crystal structure of $ZrCoD_3$ | 110 |
| Figure 3.43: Variation of occupancy of new 8e site and Zr-D distance with Ni content in $ZrCo_{1-x}Ni_xD_3$ | 111 |
| Figure 3.44: Neutron diffraction pattern of $ZrCo_{0.9}Fe_{0.1}D_3$ with Rietveld refinement. | 113 |
| Figure 3.45: Crystal structure of $ZrCo_{0.9}Fe_{0.1}D_3$ | 113 |
| Figure 3.46: Neutron diffraction pattern of $Zr_{0.8}Ti_{0.2}CoD_3$ with Rietveld refinement..... | 115 |
| Figure 3.47: Crystal structure of $Zr_{0.8}Ti_{0.2}CoD_3$ | 118 |

| | |
|---|-----|
| Figure 3.48: Variation of occupancy of new 8e site and Zr-D distance with Ti content in | |
| $\text{Zr}_{1-x}\text{Ti}_x\text{CoD}_3$. | 118 |
| Figure 3.49: Change in pressure with time for Zr-Co-M-H ₂ systems at 750 K. | 119 |
| Figure 3.50: XRD patterns of Zr-Co-M hydrides before disproportionation studies. | 121 |
| Figure 3.51: XRD patterns of Zr-Co-M hydrides after disproportionation studies. | 122 |
| Figure 3.52: Change in pressure with time for $\text{Zr}_{1-x}\text{Ti}_x\text{Co-H}_2$ systems at 750 K. | 123 |

LIST OF TABLES

| | |
|--|----|
| Table 1.1: Atomic Properties of hydrogen, deuterium and tritium isotopes | 11 |
| Table 1.2: Physical properties of hydrogen isotope molecules | 11 |
| Table 1.3: Characteristic data of tritium | 12 |
| Table 1.4: The variation in stability of binary hydrides of transition metals | 23 |
| Table 1.5: Hydrogen storage capacity of various systems and their volume expansion upon hydride formation | 29 |
| Table 3.1: Comparison of thermodynamic parameters of dehydrogenation reaction of ZrCo-H ₂ system | 62 |
| Table 3.2: Rietveld refinement results of X-ray diffraction patterns of ZrCo _{1-x} Ni _x alloys..... | 67 |
| Table 3.3: The average chemical compositions (atom %) of ZrCo _{1-x} Ni _x alloys obtained by EDAX microanalysis. | 71 |
| Table 3.4: Thermodynamic functions for desorption of hydrogen/deuterium in ZrCo _{1-x} Ni _x -H ₂ /D ₂ systems. | 74 |
| Table 3.5: Effect of hydrogen absorption-desorption cycles on crystallite size of ZrCo _{1-x} Ni _x hydrides. | 79 |
| Table 3.6: Lattice parameters and unit cell volume of ZrCo and ZrCo _{0.9} Fe _{0.1} alloys. | 83 |
| Table 3.7: Thermodynamic functions for desorption of hydrogen/deuterium in ZrCo- H ₂ /D ₂ and ZrCo _{0.9} Fe _{0.1} -H ₂ /D ₂ systems. | 87 |
| Table 3.8: Effect of hydrogen absorption-desorption cycles on storage capacity of ZrCo and ZrCo _{0.9} Fe _{0.1} alloys..... | 90 |
| Table 3.9: Effect of hydrogen absorption-desorption cycles on crystallite sizes of ZrCo and ZrCo _{0.9} Fe _{0.1} hydrides..... | 91 |

| | |
|---|-----|
| Table 3.10: Rietveld refinement results of X-ray diffraction patterns of $Zr_{1-x}Ti_xCo$ alloys..... | 94 |
| Table 3.11: Thermodynamic functions for desorption of hydrogen/deuterium in $Zr_{1-x}Ti_xCo-H_2/D_2$ systems..... | 102 |
| Table 3.12: Lattice parameter and unit cell volumes of $ZrCo_{1-x}Ni_x$ deuterides from Rietveld refinement of XRD data. | 108 |
| Table 3.13: Rietveld refinement results of neutron diffraction data for $ZrCo_{1-x}Ni_x$ deuterides..... | 109 |
| Table 3.14: Lattice parameters and unit cell volume of $ZrCo$ and $ZrCo_{0.9}Fe_{0.1}$ deuteride..... | 114 |
| Table 3.15: Rietveld refinement results of neutron diffraction data for $ZrCo_{1-x}Fe_x$ deuterides..... | 114 |
| Table 3.16: Lattice parameter and unit cell volumes of $Zr_{1-x}Ti_xCo$ deuterides from Rietveld refinement of XRD data. | 116 |
| Table 3.17: Rietveld refinement results of neutron diffraction data for $Zr_{1-x}Ti_xCo$ deuterides..... | 116 |
| Table 4.1: Thermodynamic functions for desorption of hydrogen/deuterium in $Zr-Co-M-H_2/D_2$ systems..... | 126 |
| Table 4.2: Rietveld refinement results of neutron diffraction data for $Zr-Co-M$ deuterides..... | 127 |

CHAPTER 1

INTRODUCTION

1 Introduction

1.1 Energy demand-Fusion energy

The primary goal of all type of energy transformations is to render the energy services to improve quality of life and productivity [1]. For this purpose, it is necessary to develop a sustainable energy economy as the demands for all forms of energy will continue to rise to meet expanding economies. The major increase in demand for energy is from developing countries like India, China, Brazil, where rapid urbanization is expected and hence large-scale electricity generation will be required.

Relying on fossil fuels to meet the increasing energy demand is impractical and impossible due to the depletion of fossil fuels resources. Even if resources are available, it will produce irreparable damage to the environment by emissions of greenhouse gases, through global warming [2]. Also, the conventional nuclear power production based on fission reactions is slated to grow to about 20% of the total by 2050 [3].

To meet the world's energy demand in coming decades, energy options for the future are being explored and investigated to control the global warming and reduce the dependence on the limited crude oil and other fossil fuels. Other available energy options like solar, wind and hydro energy have very low energy density. Also, geographical region specific nature of many of these renewable energy resources restricts their applications. Hydrogen is also being actively evaluated as an alternative, portable and eco-friendly energy carrier for domestic and commercial/industrial applications [4].

Alternate energy options are based on nuclear energy, which involves the nuclear reactions in which the reactant atom(s) lose their integrity. On rearrangement of their nuclei, they form new atom(s) which are more stable than the parent atom(s). Nuclear reactions are accompanied by a much greater release of energy in comparison to combustion of fossil fuels or other conventional energy resources. The nuclear energy can be acquired either from

nuclear fission or nuclear fusion. Nuclear fission is promising, but high capital investment, radioactive waste management and public acceptance are the major factors to its continued application.

Hence, energy from nuclear fusion, which can be viewed as an advance nuclear technology, is a potentially useful complement to other energy sources in meeting the increasing global energy demand in an environment friendly way as it has advantages with regard to safety and waste disposal [5]. Fusion will be available as a future energy option by the middle of this century, and will be able to acquire a significant role in providing a sustainable, secure and safe solution to tackle global energy needs [5].

Fusion is a form of nuclear energy and, as its name implies, is the process in which light nuclei are combined together to form heavier ones. In this process, there is a small mass difference between the initial and the final reaction products which gets converted into energy through Einstein's equation $E=mc^2$, where c is the velocity of light and m is the amount of mass that "disappears" during the course of fusion reaction. The velocity of light being a very large number, it takes only a very small amount of mass conversion to produce a very large amount of energy. The brightest example of fusion reactions in nature is the Sun in which hydrogen nuclei, bound together by strong gravitational force and fuse in a chain of reactions to produce helium. The amount of energy produced per unit mass is much higher for fusion reactions than that of any other mode of energy productions.

For a fusion reaction to occur, the reacting nuclei need to have enough kinetic energy to overcome the repulsive electrostatic barrier (Coulomb barrier) between fusing nuclei.

Some of the fusion reactions of interest are as follows [6];

$$\text{D} + \text{T} \rightarrow \alpha + \text{n} \quad Q = 17.59 \text{ MeV} \quad (1.1)$$

$$\text{D} + \text{D} \rightarrow \text{T} + \text{p} \quad Q = 4.04 \text{ MeV} \quad (1.2)$$

$$\rightarrow {}^3\text{He} + \text{n} \quad Q = 3.27 \text{ MeV} \quad (1.3)$$

$$\rightarrow \alpha + \gamma \quad Q = 23.85 \text{ MeV} \quad (1.4)$$

$$\text{T} + \text{T} \rightarrow \alpha + 2\text{n} \quad Q = 11.33 \text{ MeV} \quad (1.5)$$

$$\text{D} + {}^3\text{He} \rightarrow \alpha + \text{p} \quad Q = 18.35 \text{ MeV} \quad (1.6)$$

$${}^3\text{He} + {}^3\text{He} \rightarrow \alpha + 2\text{p} \quad Q = 12.86 \text{ MeV} \quad (1.7)$$

$$\text{p} + {}^6\text{Li} \rightarrow \alpha + {}^3\text{He} \quad Q = 4.02 \text{ MeV} \quad (1.8)$$

$$\text{p} + {}^7\text{Li} \rightarrow 2\alpha \quad Q = 17.35 \text{ MeV} \quad (1.9)$$

$$\text{p} + {}^{11}\text{B} \rightarrow 3\alpha \quad Q = 8.68 \text{ MeV} \quad (1.10)$$

Probability of some fusion reactions with temperature is shown in Figure 1.1 [7].

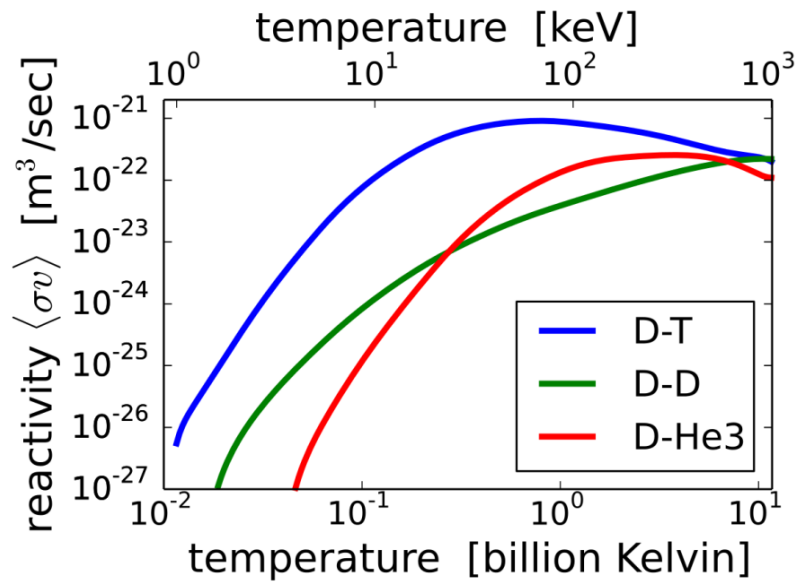


Figure 1.1: Plot of the fusion reactivity (average of cross-section times relative speed of reacting nuclei) vs. temperature for three common reactions [7].

Overcoming the repulsive Coulomb force depends on the charge of nuclei and hence the fusion among elements of higher charges occurs with increasingly lower probability and requires higher temperatures. For these reasons, fusion of deuterons with tritons has been the reaction of choice to date.

It can be seen from Figure 1.1, that the fusion reaction rate increases rapidly with temperature until it maximizes and then gradually drops off. The D-T fusion rate peaks at a lower temperature (about 70 keV, or 800 million kelvins) and at a higher reactivity value than other reactions commonly considered for fusion energy.

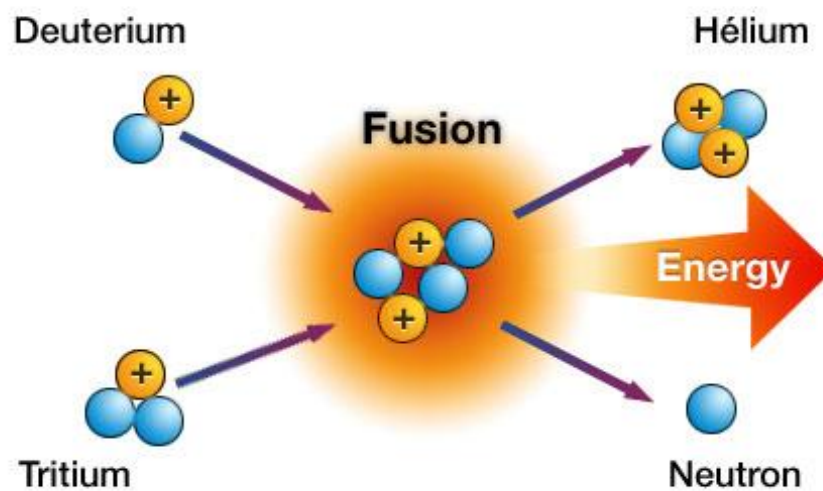


Figure 1.2: Schematic of D-T fusion reaction [5].

A deuterium and a tritium nuclei fuse to produce a helium nucleus and a neutron, Figure 1.2. The reaction produces 17.6 MeV of energy, out of which the helium nucleus carries 3.5 MeV and the neutron 14.1 MeV. In a plasma undergoing fusion, the reactions can be self sustained by utilizing the part of the kinetic energy of the resulting charged helium. For a self-sustaining fusion reaction, the tritium and deuterium plasma must be heated to over 100 million Kelvin, which requires powerful heating devices and minimal thermal loss. To sustain such a high temperature, the hot plasma is kept away from the walls of the reactor using

different confinement techniques. Confinement of plasma is achieved by creating a magnetic “cage” made by applying the strong magnetic fields. For energy production from fusion reaction, British physicist John D. Lawson demonstrated that the conditions for fusion reactions relied on three vital quantities: temperature (T), density (n) and confinement time (τ) [8]. According to John D. Lawson, fusion reaction can occur only when a minimum temperature (called the ideal ignition temperature) is exceeded and also a trade-off exists between the required density (n) and confinement time (τ): higher density requires lower confinement time and vice versa. These requirements of temperature, T , and the product of density and time, $n\tau$, came to be known as “the Lawson criterion” and constituted a scientific “Holy Grail” for fusion researchers [9].

The promise of harvesting unlimited energy from low cost and safe fuels has led to numerous attempts to mimic the thermonuclear action of the sun and the stars, to harness the energy from nuclear fusion. Till date, none of the attempts to produce sustained, controlled nuclear fusion has been able to produce energy on a commercial scale. Although small scale demonstration of successful controlled fusion reactions verify the feasibility of power generation using nuclear fusion. The best demonstration of production of fusion power was achieved in 1997 by Joint European Torus (JET) reactor at Culham in the UK, which produced a fusion power output of 16 MW from an input power of 24 MW (conversion gain $Q=0.65$) [10]. The NIF Laser Fusion reactor at the Lawrence Livermore National Laboratory (LLNL) in the USA first went live in June 2009 and up to now it is the only reactor to have exceeded breakeven performance. In 2013, it achieved a conversion gain of 1.4, but its output power is much lower than that of Tokamak and is still a long way from producing commercial power [11].

1.2 International Thermonuclear Experimental Reactor (ITER)

The scientific feasibility of fusion energy has been proven, but technical feasibility remains to be demonstrated in experimental facilities. The proposed International Thermonuclear Experimental Reactor (ITER) aims to demonstrate that fusion can be part of the solution to meet the global energy needs [12]. ITER, meaning "The Way" in Latin, is an experimental fusion reactor being constructed at Cadarache, in south of France. ITER will be the first fusion device to produce net energy, maintaining fusion for long periods of time and to test the integrated technologies, materials, and physics regimes necessary for the commercial production of fusion-based electricity [12]. The ITER partners are presently the People's Republic of China, the European Union, India, Japan, the Republic of Korea, the Russian Federation and the United States of America. The overall programmatic objective of ITER, as defined in the ITER EDA Agreement, is "*to demonstrate the scientific and technological feasibility of fusion energy for peaceful purposes*" [13]. The ITER Tokamak cutaway is shown in Figure 1.3. The ITER has been designed specially to achieve the following objectives [12];

1. Produce 500 MW of fusion power from 50 MW of input power, means ten-fold return on energy ($Q=10$).
2. Demonstrate the integrated operation of technologies for a fusion power plant.
3. Achieve a deuterium-tritium plasma in which the reaction is sustained through internal heating.
4. Test tritium breeding, means to demonstrate the feasibility of producing tritium within the vacuum vessel.
5. Demonstrate the safety characteristics of a fusion device.

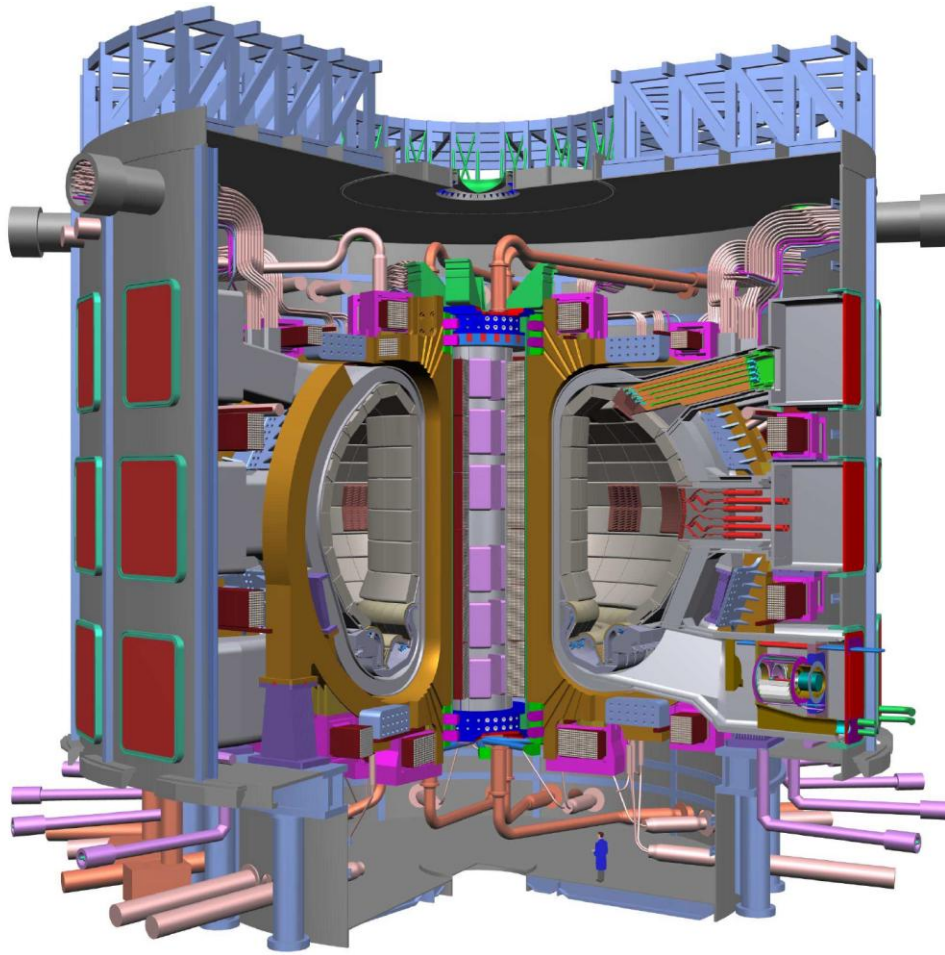


Figure 1.3: ITER Tokamak Cutaway [13].

Fusion power plants are similar to other power plants like coal, oil, and gas-fired power stations as well as nuclear fission based power stations, except the use of fusion reactions to create heat, which is then used to operate a steam turbine, which drives generators to produce electricity. A schematic of proposed fusion power plant is shown in Figure 1.4. In the plasma confinement zone, Tokamak in ITER, the deuterium and tritium fuel will burn and the energy will be released in the form of kinetic energy of charged helium, neutrons and radiation. To sustain the fusion reaction it is required to supply deuterium and tritium to Tokamak. Deuterium is present in the natural water and can be extracted easily. However, the natural abundance of tritium is very less and hence in fusion power plants it is required to produce tritium in-situ. In the proposed fusion power plants the tritium will be produced in-situ by

irradiating the lithium blanket, with neutrons generated in the fusion reaction. These lithium blankets will be positioned in the area surrounding the plasma confinement zone. Thereby, the basic fuels for nuclear fusion power plants will be lithium and water, which are readily and widely available in nature. Most of the energy will be released as heat, which can be extracted and used to make steam and drive turbines, as in any conventional power plant [14].

The production of net electrical power from fusion is planned for DEMO, the next generation reactor after ITER. DEMO will be a demonstrating device, bringing all technologies to the level of performance, reliability and efficiency required for a fusion reactor [12].

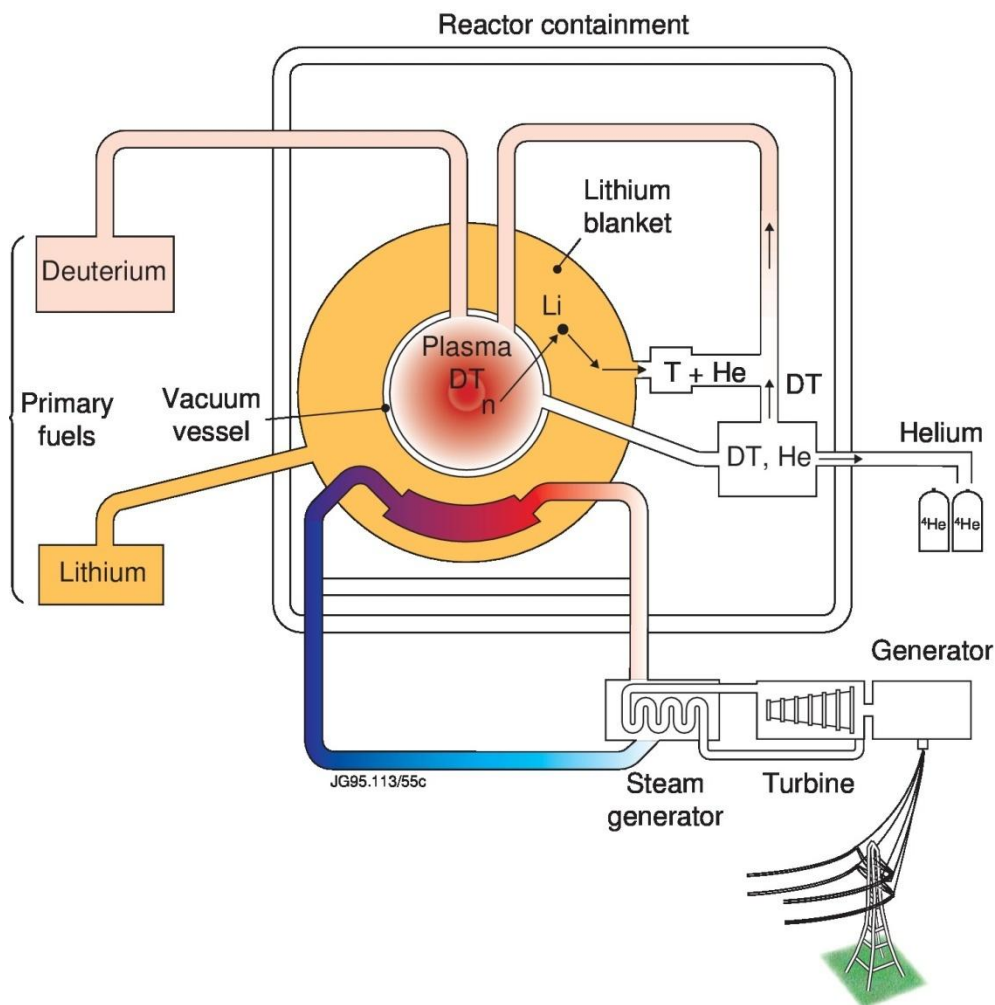


Figure 1.4: Schematic of proposed nuclear fusion power plant based on D-T fusion for electricity generation [15].

1.3 Hydrogen and its isotopes

Hydrogen is the most abundant element in the solar system, around 91% of all the atoms are hydrogen. It is the first element in the periodic table and has the simplest atomic structure among all the elements consisting of one proton and one neutron. There are three naturally occurring isotopes of hydrogen;

1. ^1H (protium or H) consists of 1 proton and 1 electron.
2. ^2H (deuterium or D) consists of 1 proton, 1 neutron and 1 electron.
3. ^3H (tritium or T) consists of 1 proton, 2 neutrons and 1 electron.

In nature H is the most abundance isotope and the abundance of other isotopes, D and T are 0.0156 atom% and 1TU (1 atom per 10^{18} atoms of hydrogen), respectively [16, 17]. In earth's atmosphere tritium is produced by interaction of cosmic radiation with nitrogen and oxygen nuclei via $^{14}\text{N}(\text{n},\text{T})^{12}\text{C}$ and $^{16}\text{O}(\text{n},\text{T})^{14}\text{N}$ reactions, respectively [18]. Some other sources of tritium production are [17-20]: (i) Irradiation of lithium with neutrons in nuclear reactor via $^6\text{Li}(\text{n},\alpha)\text{T}$ reaction, (ii) Interaction of neutrons with D present in the coolant/moderator via $\text{D}(\text{n},\gamma)\text{T}$ reaction and (iii) Ternary fission of heavy nuclei like ^{235}U , ^{238}U , ^{239}Pu and ^{241}Pu etc. in the nuclear fuel.

All the isotopes of hydrogen form covalent molecules like H_2 , D_2 and T_2 . In contrast to H and D, tritium is radioactive in nature. Tritium is the radionuclide with lowest beta decay energy and its decay reaction can be written as [17];



where, β^- is a beta particle and $\bar{\nu}$ is an antineutrino. The maximum energy of beta particle is 18.6 keV and the average energy is 5.7 keV. The atomic properties of H, D, and T and the physical properties of H_2 , D_2 , and T_2 are compared in Table 1.1 and 1.2, respectively. Radiation characteristic data of tritium are listed in Table 1.3.

Table 1.1: Atomic Properties of hydrogen, deuterium and tritium isotopes [16-18].

| Properties | H | D | T |
|---|----------------------|------------------------|------------------|
| Relative atomic mass (a.m.u.) | 1.007825 | 2.014102 | 3.016049 |
| Nuclear spin | 1/2 | 1 | ½ |
| Nuclear magnetic moment (μ_N) | 2.79268 | 0.857386 | 2.9788 |
| Nuclear quadrupole moment (em^2) | 0 | $2.766 \cdot 10^{-31}$ | 0 |
| Incoherent neutron cross-section, σ_{inc} (barns) | 80.20 (± 0.06) | 2.04 (± 0.3) | 0.0 (+0.1, -0.8) |
| Natural abundance (%) | 99.984 | 0.0156 | 10^{-16} |

Table 1.2: Physical properties of hydrogen isotope molecules [16-19].

| Properties | H ₂ | D ₂ | T ₂ |
|---|----------------|----------------|----------------|
| Molecular weight (g/mole) | 2.015 | 4.028 | 6.032 |
| Triple point temperature (K) | 13.804 | 18.69 | 20.62 |
| Boiling point (K) | 20.39 | 23.67 | 25.04 |
| Heat of fusion (kJ/mole) | 0.117 | 0.197 | 0.250 |
| Critical temperature (K) | 33.19 | 38.35 | 40.6 |
| Heat of dissociation at 298 K (kJ/mole) | 435.88 | 443.35 | 446.9 |
| Zero-point energy (kJ/mole) | 25.9 | 18.5 | 15.1 |

Table 1.3: Characteristic data of tritium [17, 20-22].

| | |
|--|--|
| Atomic mass | 3.01605 g |
| Half-life $t_{1/2}$ | 12.323 y (1y = 365.25 d) |
| Decay constant, $\lambda = \ln 2/t_{1/2}$ | $1.782 \cdot 10^{-9} \text{ s}^{-1}$ |
| Maximum β energy | 18.6 keV |
| Mean β energy | 5.69 keV |
| Most probable β energy | 3.0 keV |
| Maximum range of β in air | 4.5 - 6 mm |
| Heat produced by tritium | 0.324 W/g \equiv 1.954 W/mole T_2 , 33.7 μ W/Ci, |
| Ionization energy: $T \rightarrow T^+ + e^-$ | 13.595 eV |
| Dissociation energy: $T_2 \rightarrow 2T$ | 4.591 eV |
| Specific activity of tritium gas | 9615 Ci/g, 58 kCi/mole T_2 , 2.38Ci/cc @STP, 1ppm \equiv 2.6Ci/m ³ |
| Specific activity of T_2O | 2633 Ci/g |

1.4 Storage methods for hydrogen isotopes

A range of methods are available for storage of hydrogen isotopes. However, the choice depends on several factors like nature of application, amount to be stored, storage time, energy density needed, maintenance requirements and cost. Due to radioactive decay of tritium, storage of this isotope of hydrogen puts additional constraints on the storage material. The lattice of the storage material of tritium can develop serious defects due to interaction with beta particles and dispersion of alpha particles. Additionally, for long term storage there can be considerable pressure built up in the storage container due to in-situ production of helium.

Hydrogen storage methods can be broadly classified as [23]:

1. Gaseous storage
2. Liquid storage
3. Solid storage

1.4.1 Gaseous storage: High pressure gas cylinders

The most common method to store hydrogen is as compressed gas. In this method, the hydrogen is typically compressed at high pressure and stored in gas cylinders or spherical containers. However, the gravimetric density of hydrogen in this method is very low due to higher weight of storage container itself [24]. Also, due to explosive interaction of hydrogen with air, there are safety issues with hydrogen storage at high pressure. Owing to the radioactive nature of tritium gas, it is not safe to store it above atmospheric pressure.

1.4.2 Liquid storage

Hydrogen can be liquefied and stored in cryogenic tanks at around 20 K and ambient pressure. Advantage of liquid hydrogen storage is high gravimetric density, whereas, the drawback is low volumetric density. Another drawback of liquid hydrogen is the high cost of liquefaction and the continuous loss of hydrogen due to “boil-off” [25]. This method is also not suitable for storage of radioactive tritium gas due to safety reasons. Safety issues due to accidental leakage of hydrogen from the container are even higher in this storage. Small, but continuous heating of the tanks results in build-up of gaseous hydrogen pressure in the tanks.

1.4.3 Solid storage

Storage of hydrogen isotopes (H, D and T) in the solid state is the safest and most advantageous method over other conventional methods like gaseous storage in high pressure gas cylinders and liquid storage in cryogenic tanks. Hydrogen and its isotopes can be stored in the solid state by combining it with a solid state material through physisorption [26], chemisorption [27] or by chemical reactions [24]. At elevated temperatures, hydrogen reacts

with many transition metals, f-block elements and their alloys to form hydrides. The nature of the chemical bond determines the thermodynamic stability of the hydride, the hydrogen stoichiometry of the material, and the mechanisms for hydrogen absorption and release. Metal hydrides have high volumetric hydrogen density as compared to gaseous and liquid storage.

1.5 Solid state storage of hydrogen isotopes

Many metals/alloys have the property of combining chemically with hydrogen to form a class of compounds called metal hydrides. For the metal/alloy to be used as solid state storage of hydrogen isotopes, it should satisfy certain requirements such as [4, 18, 20, 28];

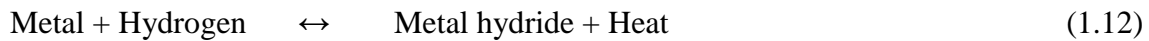
1. High dissociation pressure at moderate temperatures, to allow quantitative recovery of the incorporated gas with minimal permeation losses.
2. Facile reversibility of hydride formation and decomposition reactions.
3. High hydrogen storage capacity
4. Good hydrogen absorption-desorption cyclic life stability.
5. Wide plateau regions in the absorption desorption pressure-composition isotherms (PCIs) for fast kinetics & low permanent tritium trapping.
6. Minimal hysteresis in absorption-desorption pressure-composition isotherms (PCIs).
7. The reactivity of the metal/hydrides/deuterides/tritides system towards air & contaminant gases in the fusion fuel cycle should be moderate.
8. Products formed by reactions with these contaminants should not poison the surface and inhibit the uptake of hydrogen.
9. Operation and maintenance cost of material should be affordable for the intended application.

10. Very low equilibrium pressures over the tritides at room temperature to contain the radioactivity within it.

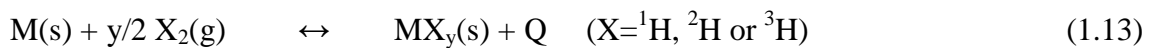
A combination of safety, technical and economical consideration will determine the suitability of any material for storage of hydrogen isotope.

1.5.1 Theory of metal-hydrogen interaction

The reaction between metal and hydrogen can be expressed as;



or



Where M is metal/alloy, MX_y is metal hydride/deuteride/tritide and y is the ratio of hydrogen to metal/alloy denoted as H/M or H/f.u. (f.u.=formula unit of alloy). Q is the heat released during the course of forward reaction and heat absorbed during the backward reaction. The reaction of hydrogen with metal to form metal hydride is a complex reaction and it involves many processes. In a simplified way the metal-hydrogen interaction can be described by one-dimensional potential energy curve (Lennard-Jones potential) [29], as shown in Figure 1.5.

In the Lennard-Jones potential energy diagram (Figure 1.5), far from the metal surface the potential energy hydrogen molecule is lower than that of two hydrogen atoms. The difference is equal to the dissociation energy of hydrogen molecule, 436 kJ/mol H_2 (Table 1.2). This potential energy diagram is plotted with reference to $\text{H}_2(\text{g})$, therefore potential energy of $\text{H}_2(\text{g})$ molecule is at zero potential. When hydrogen molecule moves towards the metal surface, at some point it starts feeling the weak attractive forces (Van der Waals forces) of range ~ 0 to -40 kJ/mole H_2 . This leads to physisorbed state of hydrogen, at around one molecular hydrogen radius distance (~ 0.2 nm) from the metal surface. If the molecule moves closer to the surface, the potential energy will increase due to repulsion. Hence, the hydrogen molecule has to overcome an activation barrier for dissociation of H-H bond and formation of

the metal-hydrogen bond. The height of the activation barrier depends on the surface elements involved. If intersection is located at approximately zero potential energy, dissociation is said to be activated. On the other hand, if intersection is at a potential energy larger than zero relative to gas phase H_2 , dissociation is said to be non-activated and the height determines the activation barrier. In this case, only the fraction of H_2 molecules having the energy larger than the activation barrier will be able to dissociate. After dissociation, the hydrogen atoms find a potential energy minimum which corresponds to the H atoms being bonded to the metal surface (chemisorption). The nature of chemisorption depends on the relative bond strength of H-H and M-H bonds.

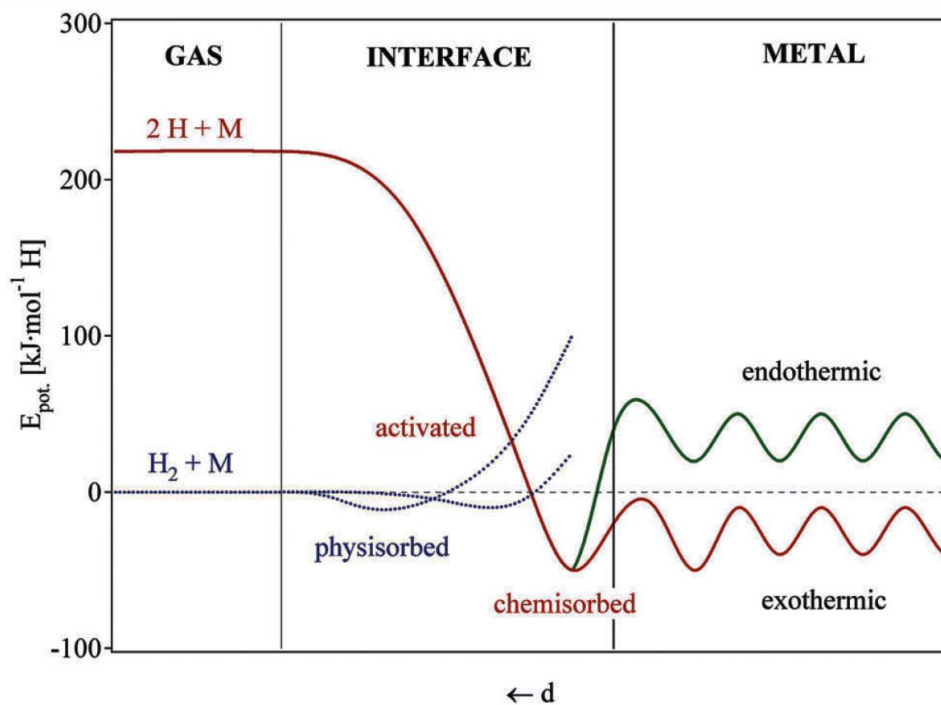


Figure 1.5: Lennard-Jones potential energy diagram for chemisorptions of hydrogen in metals (Reprinted from [24], Copyright (2003), with permission from Elsevier).

Chemisorption process is said to be exothermic if the H-M bond is stronger than the H-H bond and endothermic if the H-H bond is the stronger. After chemisorption, the hydrogen

atoms can penetrate the first metal atomic layer into the subsurface through an activated process from which it can diffuse into the bulk (as a solid solution) of the metal. If the potential energy of bulk H-atoms is below zero relative to gas phase H_2 , hydrogen solid solution is said to be exothermic, if the potential energy of bulk H-atoms is above zero, hydrogen solid solution is said to be endothermic [24, 30, 31].

Therefore, the complete interaction of hydrogen gaseous molecule with metal/alloy resulting in absorption of hydrogen to form metal/alloy hydride is composed of the following processes as shown in Figure 1.6 [32];

1. Physisorption of hydrogen molecules;
2. Dissociation of hydrogen molecules and chemisorption;
3. Surface penetration of hydrogen atoms;
4. Diffusion of hydrogen atoms through the hydride layer, either by an interstitial or a vacancy mechanism;
5. Hydride formation at the metal/hydride interface

For de-hydrogenation reaction, the process is the reverse i.e. hydride decomposition at the hydride/metal interface, diffusion of hydrogen atoms to the sub-surface, surface penetration, recombination of chemisorbed hydrogen atoms and physisorption and desorption to the gas phase [32].

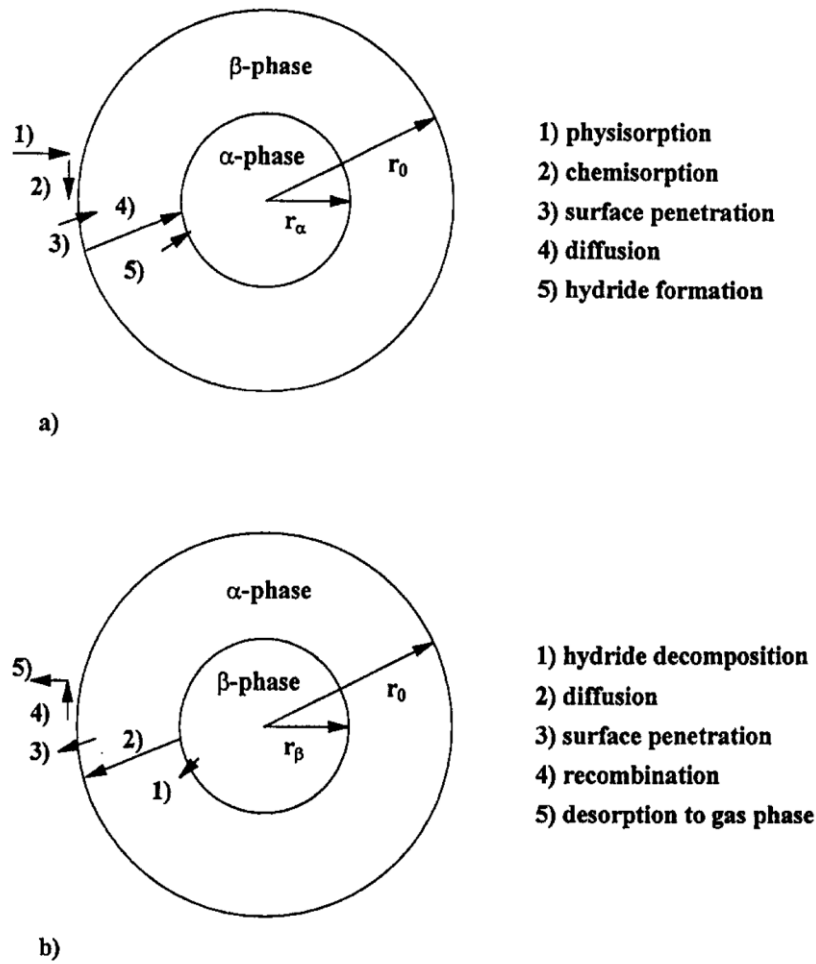


Figure 1.6: Reaction steps for the (a) absorption and (b) desorption of hydrogen by a spherical metal/hydride powder particle (α -phase: Solid solution of hydrogen in metal β -phase: Hydride phase) (Reprinted from [32], Copyright (1996), with permission from Elsevier).

1.5.2 Thermodynamics of Metal-Hydrogen system

Thermodynamic properties of metal-hydrogen system is of great importance for its selection as suitable hydrogen isotope storage material. The behavior of a metal-hydride system can be best represented by pressure-composition isotherms (PCIs). Collection of PCIs at different temperature is known as pressure-composition-temperature (PCT) diagram. A schematic of PCT diagram is shown in Figure 1.7, it is a plot of pressure vs. composition at different temperatures.

At a particular temperature, when metal is exposed to hydrogen, initially the hydrogen concentration in metal increases with increase in pressure. This happens due to solubility of hydrogen in the metal lattice and this phase known as solid solution of hydrogen in metal, denoted by α -phase. When the maximum solubility of hydrogen in the α -phase is reached, interactions between hydrogen atoms become locally important and nucleation and growth of the hydride phase (β -phase) occurs [33]. Further increase in the hydrogen pressure results in substantial increase in hydrogen concentration in metal. In this region of PCIs, the α -phase and β -phase co-exist and the isotherms show a flat plateau. From the Gibbs phase rule [34], the degree of freedom (F) is;

$$F = C - P + 2 \quad (1.14)$$

Where, C is the number of components and P is the number of phases. Therefore, in the two-phase region the hydrogen concentration in the solid matrix increases, while the hydrogen pressure is constant. At same hydrogen pressure, with passage of time, more of α -phase interacts with hydrogen to form β -phase. When all the α -phase disappears and pure β -phase present in the system, then the system has two degrees of freedom. Under this condition further increase in hydrogen concentration in solid matrix requires higher pressures of hydrogen gas. This corresponds to the solid solution of hydrogen in the non-stoichiometric β -phase. Therefore, the whole PCI curve can be divided into three distinct regions; α -phase region with low hydrogen concentration, β -phase region with high hydrogen concentration and $\alpha + \beta$ phase region. With increase in temperature, hydrogen solubility range of α and β phases increases. Therefore, when such PCIs are plotted at different temperatures, the plateau region corresponding to two phase region starts decreasing with increase in temperature. The two-phase region ends in a critical point T_c , above which the transition from α - to β - phase is continuous. Therefore above the critical temperature the system will not show the plateau

region. Multiple plateau regions are possible for the metals and alloys forming the two or more hydride phases.

The $\alpha + \beta$ phase region, also known as plateau region, is of great importance and gives valuable information about the hydrogen storage behavior of any material. Width of plateau is related to the reversible storage capacity of material in the two phases, and the value of plateau pressures at given temperature gives the idea about the stability of metal hydride. The plateau pressure or equilibrium pressure depends strongly on temperature and is related to the changes in enthalpy and entropy of the metal-hydrogen reaction. Stable hydrides require higher temperatures than less stable hydrides to reach a certain plateau pressure.

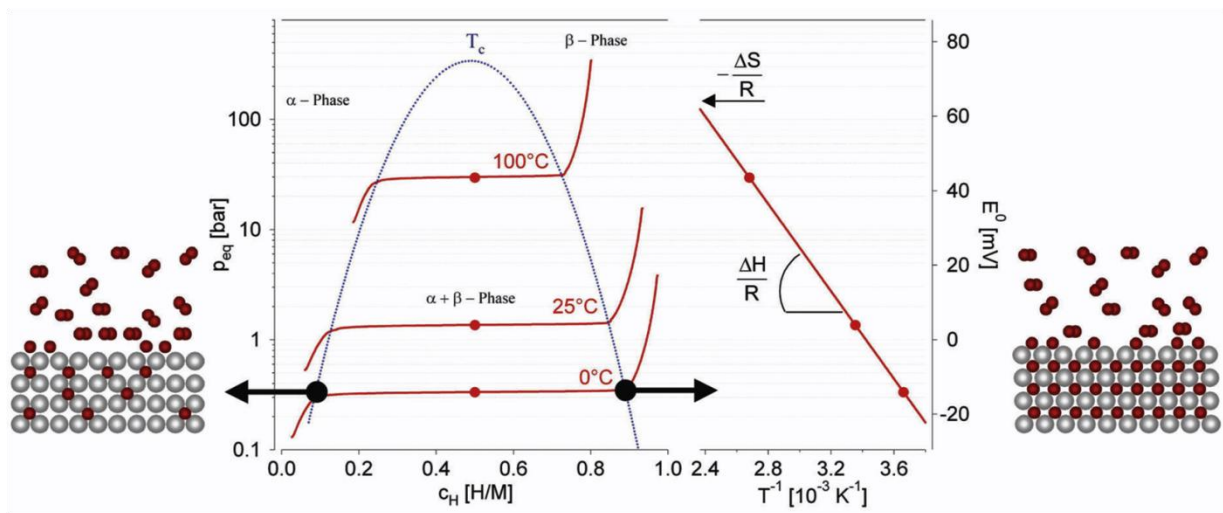


Figure 1.7: Schematic of pressure-composition isotherms (PCIs) and van't Hoff plot

(Reprinted from [24], Copyright (2003), with permission from Elsevier).

In general the PCIs of metal-hydrogen systems exhibit sloping plateau, rather than a flat and horizontal plateau. This phenomenon may be arising due to surface heterogeneities, impurities, particle size and stresses, which results in different equilibrium pressure of hydrogen for different parts of the substrate [28]. In many metal-hydrogen system, hysteresis has been observed, means plateau pressure of absorption PCI is higher than that of desorption

PCI as shown in Figure 1.8. Different theories based on defect [35], solvov behavior [36] etc. were reported in the literature to explain the phenomenon of hysteresis. However, the exact cause of hysteresis is not fully understood till date.

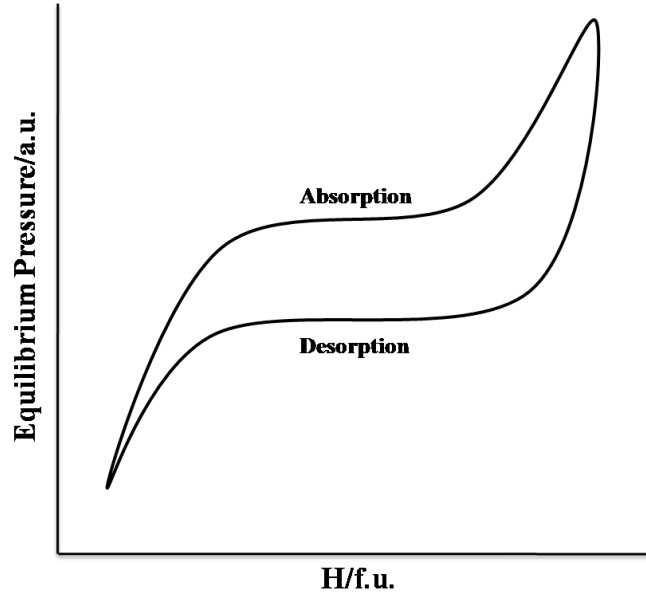


Figure 1.8: Schematic diagram of hysteresis in an absorption-desorption PCI.

Important thermodynamic parameters like changes in standard free energy ($\Delta_r G^\circ$), enthalpy ($\Delta_r H^\circ$) and entropy ($\Delta_r S^\circ$) of metal-hydrogen reaction can be deduced from the plateau pressure data of the PCT diagram, using the following equations:

$$\Delta_r G = \Delta_r G^\circ + RT \ln K_P \quad (1.15)$$

For bi-phasic ($\alpha + \beta$) region at equilibrium, $\Delta_r G = 0$, which implies that:

$$\Delta_r G^\circ = -RT \ln K_P$$

For metal-hydrogen reaction, $M + (y/2) H_2(g) \leftrightarrow MH_y$, shown in Eq. (1.13),

$$K_P = 1/(P_{H_2})^{y/2}$$

Thus,

$$\Delta_r G^\circ = y/2 RT \ln P_{H_2}$$

but,

$$\Delta_r G^\circ = \Delta_r H^\circ - T \Delta_r S^\circ \quad (1.16)$$

Hence,

$$\ln P_{H_2} = 2/y (\Delta_r H^0/RT) - 2/y (\Delta_r S^0/R)$$

$$\ln P_{H_2} = (2\Delta_r H^0/yR) (1/T) - (2\Delta_r S^0/yxR) \quad (1.17)$$

For one mole of hydrogen equation (1.17) can be rewritten as;

$$\ln(P_{H_2}/P^0) = \Delta_r H^0/RT - \Delta_r S^0/R \quad (1.18)$$

where, P^0 is the atmospheric pressure, R is the gas constant (8.314 J/mole·K) and T is the absolute temperature. The plot of natural logarithm of hydrogen equilibrium plateau pressure versus the reciprocal of the absolute temperature $1/T$ is called van't Hoff plot, Figure 1.7. From a number of measurements of PCI, plateau pressures (P_{H_2}) at different temperatures can be used to construct a van't Hoff plot. The $\Delta_r H^0$ and $\Delta_r S^0$ can be evaluated from the slope and intercept of van't Hoff plot, respectively [33]. The entropy change mainly corresponds to the loss of translational degree of freedom when hydrogen gas enters the metal lattice.

1.5.3 Selection of suitable metal/alloys for solid state storage

Most of the elements in periodic table react with hydrogen to form binary hydrides. However, all hydrides are not suitable for their application in storage of hydrogen isotopes since they are either too stable or too unstable. The variation in stabilities of some transition metal binary hydrides is shown in Table 1.4.

Table 1.4: The variation in stability of binary hydrides of transition metals* [37].

| IIIA | IVA | VA | VIA | VIIA | VIIIA | IXA | XA |
|------------------|------------------|--------------------|-------|-------|-------|--------------------|--------------------|
| ScH ₂ | TiH ₂ | VH ₂ | CrH | MnH | FeH | CoH _{0.5} | NiH _{0.5} |
| -200 | -126 | -54 | -16 | -9 | +14 | 0 | -6 |
| YH ₂ | ZrH ₂ | NbH ₂ | MoH | TcH | RuH | RhH _{0.5} | PdH _{0.5} |
| -225 | -165 | -60 | -12 | (+36) | (+42) | (+25) | -40 |
| LaH ₂ | HfH ₂ | TaH _{0.5} | WH | ReH | OsH | IrH | PtH |
| -210 | -133 | -78 | (+16) | (+52) | (+48) | (+42) | (+26) |
| ThH ₂ | UH ₃ | PuH ₂ | | | | | |
| -146 | -85 | -155 | | | | | |

*Values are for enthalpy of formation of the hydrides in kJ/mole H₂, Values in brackets are estimated from empirical model considerations [38].

As discussed in Section-1.5.1 and 1.5.2 that stability of metal/alloy hydrides is related to the changes in standard free energy ($\Delta_r G^\circ$), enthalpy ($\Delta_r H^\circ$) and entropy ($\Delta_r S^\circ$) of metal/alloy-hydrogen reaction involved. By tuning the enthalpy and entropy of metal/alloy-hydrogen system, the desired pressure can be obtained using Eq. 1.18. Using this equation, the desorption temperature (T_{des}) to generate 1 bar (10^5 Pa) pressure can be given as:

$$T_{des} = \left(\frac{\Delta_r H^\circ}{\Delta_r S^\circ} \right) \quad (1.19)$$

If the entropy change for a hydrogen absorption reaction is considered dominated by the loss of entropy of hydrogen gas (130 J/K.mole H₂ at room temperature) upon its absorption in solid, the $\Delta_r S^\circ$ can be taken around 130 J/K.mole H₂. In this case, for generation of 1 bar hydrogen pressure at 298 K, the enthalpy of formation of hydrides, from Eq. 3.19, should be around -40 kJ/mole H₂.

For a practical approach, by combining the two or more metallic elements one can get the alloy or intermetallic compound of desired thermodynamic property. In general, for a

combination the elements are chosen in such a way that one of the elements forms stable hydride while the others form unstable hydrides.

1.6 Hydrogen Isotope effect

Differences in chemical and physical properties arising due to difference in the nuclear mass of an element is called isotope effect. Hydrogen isotope effects are more pronounced due to the large difference in relative masses of hydrogen isotopes, as compared to other elements of periodic table. The vibrational, rotational and translational motion of the molecule is greatly affected by the change in mass of an atom. As per quantum mechanics, the vibrational and rotational states are quantized which results in different discrete energy levels for isotopic molecules. This difference in energy levels leads to differences in the distribution of isotopic molecules between different states. In case of equilibrium isotope effect, the contribution of the vibrational energy is dominant over the translational and rotational energies [16]. The schematic of potential energy curve for hydrogen isotope molecules is shown in Figure 1.9. Since, the force binding the molecules is independent of change in atomic mass upon isotopic substitution the potential energy curve remains same for all hydrogen isotopic molecules like H_2 , HD, D_2 , T_2 etc.. The vibrational energy of a diatomic molecule, in the harmonic oscillator approximation, can be given as:

$$E = (n+1/2) h\nu \quad (1.20)$$

Where, n represents an integer number from zero, ν is the vibrational frequency and h is the Plank's constant.

The vibrational frequency (ν) is given by;

$$\nu = (1/2\pi)(k/\mu)^{1/2} \quad (1.21)$$

where, k is the force constant and μ is the reduced mass. At lower temperatures, the lowest vibrational levels will be populated and isotopic substitution will greatly affect the processes

which involve vibrational excitation. Substitution of lighter isotope with heavier isotope will result in increase in μ and thus lowering the vibrational frequency (ν). Therefore the molecules substituted by deuterium and tritium have correspondingly smaller zero point energies, as shown in Table 1.2.

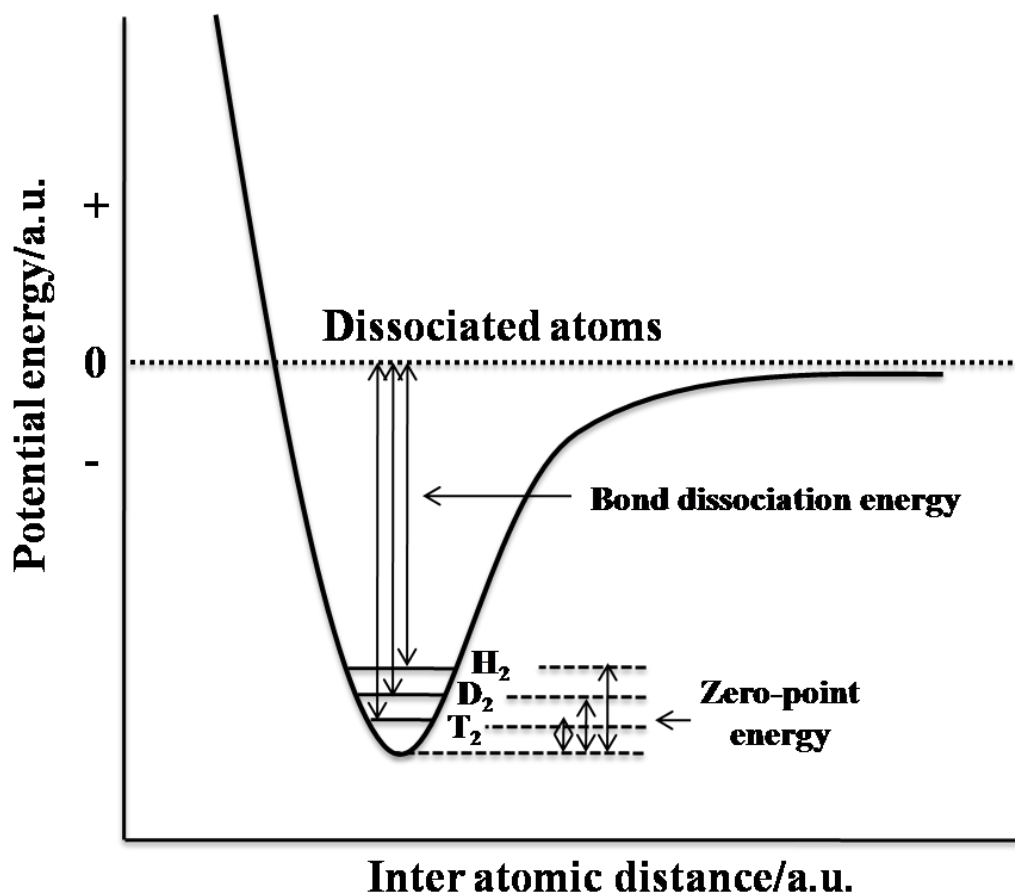


Figure 1.9: Schematic potential energy curve for the hydrogen molecules [16], Figure not to scale.

The vibrational energy corresponds to $n=0$ is known as vibrational Zero Point Energy (ZPE) and is $1/2h\nu$. This is the energy, possessed by the molecules even at the absolute zero temperature. It is evident from Figure 1.9 that heavier isotope has the lowest zero-point energy. Thus ZPE of H_2 is 3 kJ/mol higher than that of HD and 8 kJ/mol higher than that of D_2 [16]. This shows that the binding of heavier nucleus is stronger than lighter nucleus.

In the metal-hydrogen system, when hydrogen reacts with metal/alloy, it can occupy tetrahedral and/or octahedral interstitial sites. The reason behind the thermodynamic isotope

effect can be best explained by considering the potential wells and the zero-point energies of gaseous hydrogen isotope molecules and atoms in tetrahedral/octahedral interstitial sites. A schematic comparison of zero-point vibration energies of hydrogen isotopes in tetrahedral/octahedral positions with that of gas phase molecules is shown in Figure 1.10.

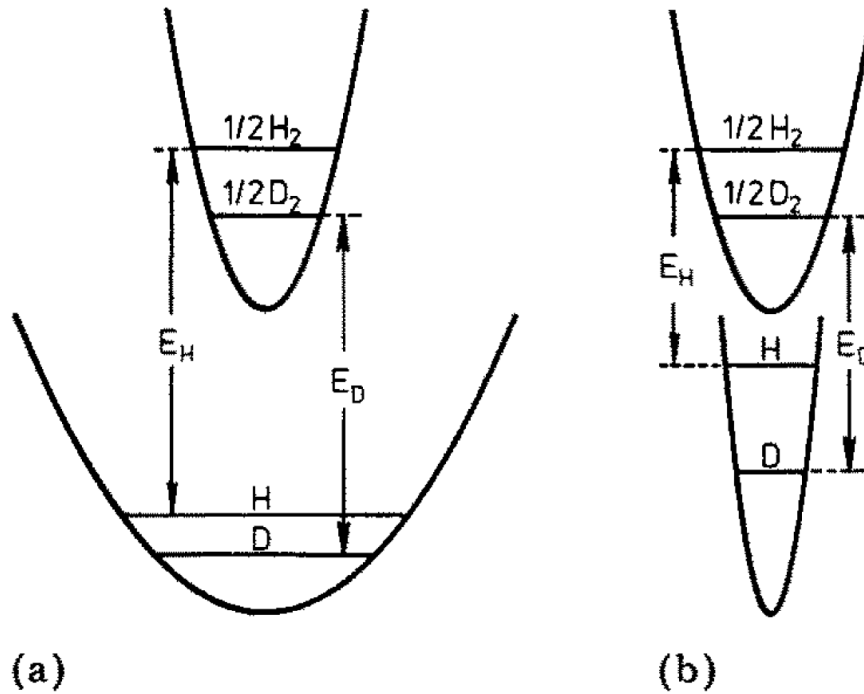


Figure 1.10: The Schematic comparison of the zero-point vibrational energies of hydrogen isotopes in (a) octahedral and (b) tetrahedral interstitial position with that of gas phase molecules (Reprinted from [39], Copyright (1984), with permission from Elsevier).

It can be seen from the figure, that the octahedral potential profile is flat whereas the tetrahedral potential profile is narrow and steep, which is in accordance with the size of octahedral and tetrahedral interstitial sites [39]. Hence, the relative change in zero-point energies of hydrogen isotopes from gaseous molecules to hydride state is of primary concern for the relative stability of metal/alloy hydrides/deuterides/tritides. The more abundant hydrogen isotope in the solid phase will be the one for which the vibrational zero point

energy difference between the gas phase and double of corresponding energy level in solid state phase is the largest. If $|E_D| > |E_H|$, means more energy is gained by the absorption of a D_2 molecule than by that of a H_2 molecule and hence deuterium will have higher preference for the solid phase as compared to hydrogen [18, 40, 41].

In the metal-hydrogen system, the isotope effect on equilibrium pressure of hydrogen molecules over the corresponding hydrides can be explained by considering the change in Gibbs free energy of reaction of interest. As discussed earlier, the free energy of hydrogen desorption reaction ($\Delta_r G^\circ$) can be written as;

$$\Delta_r G^\circ = \Delta_r H^\circ - T\Delta_r S^\circ = -RT \ln(P/P^\circ) \quad (1.22)$$

It can be seen from Eq. (1.22) that the hydrogen isotope effect on the equilibrium pressure of hydrogen arises from the interplay of two thermodynamic parameters namely, entropy and enthalpy change of reaction that control the relative stabilities of the corresponding isotopic hydrides. The value of entropy of desorption reaction ($\Delta_r S^\circ$) for the heavier isotope hydride is more positive than the lighter ones, as the absolute entropies of hydrogen isotopes in the gas phase follow the order $S^\circ(T_2) > S^\circ(D_2) > S^\circ(H_2)$ [42], leading to a '*positive or normal*' isotope effect where the plateau pressure of the hydrogen isotopes will follow the trend: $p(T_2) > p(D_2) > p(H_2)$. The enthalpy of hydrogenation/de-hydrogenation reaction also decides the nature of isotope effect. When the $\Delta_r H^\circ$ of the lighter isotope hydride is more than the heavier isotope hydrides, a *normal* isotope effect is observed for the system, irrespective of temperature. On the other hand, when the $\Delta_r H^\circ$ of the heavier isotope hydride is more than the lighter ones, a temperature dependent isotope effect is expected. Below a certain temperature, *inverse* isotope effect will be observed whereas above this temperature the isotope effect is normal.

1.7 Materials for hydrogen isotope storage and challenges

Solid state storage of hydrogen isotopes (H, D and T) in the form of metal hydrides/deuterides/tritides are being considered as the safest and the most advantageous method over the conventional storage methods like gaseous storage in high pressure gas cylinders and liquid storage in cryogenic tanks [20]. In case of hydrogen/deuterium storage purpose, it is expected that the material should have as high as desorption pressure at near ambient temperatures. However, tritium being radioactive in nature, the criteria for tritium storage materials differs from the conventional hydrogen storage materials. For a material to be used for the interim storage of tritium as metal tritide in the tritium handling facilities, it should have very low equilibrium pressure of tritium over the tritide at room temperature so that all the tritium activity gets trapped within the storage container. Also, the metal tritide should desorb the stored tritium at moderate temperatures, to avoid the permeation losses of tritium from the storage container itself and release of the activity in the environment. Apart from these, the metal tritide should have high He-3 retention capacity so that high purity tritium can be desorbed upon heating the metal tritide. A comparison of different storage options is shown in Table 1.5. It is evident from this table that, metal tritides can store tritium at very high capacity as the hydrogen atom density in most of metals and intermetallic compounds is generally higher than that in pure liquid or even solid hydrogen at cryogenic temperatures.

Table 1.5: Hydrogen storage capacity of various systems and their volume expansion upon hydride formation [43].

| System | N_H (10^{22} at/cm ³) | W_H (%) | ΔV (%) = ($V_{\text{hydride}} - V_{\text{metal}}$)/ V_{hydride}) |
|---------------------------------------|--|-----------|---|
| H ₂ , gas (298 K, 200 bar) | 1.0 | 100.0 | -- |
| H ₂ , liquid (20 K) | 4.2 | 100.0 | -- |
| H ₂ , solid (4K) | 5.3 | 100.0 | -- |
| VH _{0.8} | 5.1 | 1.56 | -- |
| FeTiH _{1.74} | 5.4 | 1.66 | 20 |
| LaNi ₅ H _{6.7} | 5.8 | 1.54 | 34 |
| MgH ₂ | 6.5 | 7.65 | -- |
| ZrH ₂ | 7.3 | 2.16 | -- |
| ZrCoH ₃ | 7.6 | 1.97 | 20 |
| ZrNiH ₃ | 7.7 | 1.97 | -- |
| UH ₃ | 8.2 | 1.25 | 75 |
| TiH ₂ | 9.2 | 4.04 | -- |

Many transition metals like Zr, Ti and Y have high tritium storage capacity [33, 44, 45], but cannot be used for the supply of tritium as their tritides are too stable. They require very high temperature for adequate desorption pressure of tritium, where the permeation losses from storage container becomes significant. Therefore, these hydrides, i.e. TiH_x, ZrH_x, YH_x, etc., are suitable for gettering [33, 46] and long term disposal of tritium [47]. Here, it is important to point out that most of the storage containers are made up of stainless steel and at high temperatures (>973 K) permeation of hydrogen isotopes from the stainless-steel wall becomes significant [18, 20].

Uranium beds are extensively used for interim storage, supply and recovery of tritium [48] due to their favourable tritium storage properties, like: i) large storage capacity (H/U atomic ratio up to 3), ii) very low dissociation pressure at room temperature for holding tritium tightly within the material and iii) moderate desorption temperature (~700 K) to have sufficiently large release pressure (~100 kPa) for supply of tritium. However, upon hydrogenation, uranium easily disintegrates into fine powder, which is highly pyrophoric in nature [49] and have low thermal conductivity due to which temperature control of specimens becomes difficult during hydrogenation. This fine powder is difficult to contain within the storage bed, resulting in damages to valves and other components of the system. Another drawback of uranium is that, its radioactive nature makes it nuclear-controlled material, which imposes constraints due to inventory monitoring and regulated movement. For these reasons, there is a need for the development of alternate materials for interim storage of tritium which can replace the conventional uranium bed. In this context, various uranium, zirconium and lanthanum based alloys, such as U_2Ti , $UZr_{2.3}$, $ZrCo$, $ZrNi$, $LaNi_{5-x}Al_x$, $LaNi_{5-x}Mn_x$ etc. [50-56] have been studied in the recent years, which show improved storage properties over pure uranium metal.

Among these, the intermetallic compound $ZrCo$ is being considered as a suitable hydrogen isotope storage material for different tritium processing facilities like International Thermonuclear Experimental Reactor (ITER) [57-59]. This consideration of $ZrCo$ can be attributed to its higher storage capacity (H/f.u. up to 3, f.u. = $ZrCo$) [53], non-radioactive nature, non-pyrophoricity at room temperature [49] and tritium storage properties similar to uranium [43, 60].

Reaction of $ZrCo$ with hydrogen can be written as;



However, ZrCo has drawback of hydrogen induced disproportionation upon repeated hydriding-dehydriding cycles [41, 61-65]. The hydrogen induced disproportionation reaction in ZrCo-H₂ system can be written as;



The hydrogen induced disproportionation results in the formation of a hydrogen non-absorbing ZrCo₂ phase and a very stable ZrH₂ hydride phase. Since, decomposition of ZrH₂ requires much higher temperature (> 973 K) than that of ZrCo-hydride, a significant amount of hydrogen gets trapped within the storage material. On the other hand, recovery of hydrogen from the ZrH₂ phase at temperature > 973 K results in significant permeation losses from the storage container material. Thus hydrogen induced disproportionation results in reduction of hydrogen storage capacity of ZrCo, which is not desirable for its use in ITER Storage and Delivery System (SDS). Konishi et al. [62] have reported that the extent of disproportionation can be suppressed by decreasing the de-hydriding temperature. However, decreasing the de-hydriding temperature lowers the hydrogen equilibrium pressure of ZrCo-H₂ system due to which the required delivery pressure of 100 kPa of hydrogen can't be achieved.

Hence, alternative choice to overcome the above mentioned problem of ZrCo alloy is to thermodynamically stabilize the hydride phase (ZrCoX₃) by suitable ternary alloying with another element (M) and maintaining the equilibrium pressure (p_{H_2}) close to 100 kPa at a lower temperature which in turn will reduce the extent of disproportionation reaction. Thermodynamically, the alloying element M will elevate the desorption equilibrium hydrogen pressure compared to the parent compound ZrCoX₃ at a particular temperature. Then, it is possible to deliver the required pressure of 100 kPa of hydrogen with reduced desorption temperature, thereby preventing the extent of disproportionation. Several attempts were made to improve its durability against disproportionation by substituting either Zr or Co

with a third element without substantially altering the storage behaviour. A very limited study is reported in literature on the effect of ternary alloying on the hydrogen storage behavior of ZrCo based alloys [66-71]. However, to the best of our knowledge, there is no data reported in the open literature on isotope effect of hydrogen storage behavior of ZrCo based ternary alloys.

Tritium being a radioactive gas, many of the experiments related to development of tritium storage materials are primarily carried out using hydrogen and deuterium. Owing to the similar chemical properties, reactions of hydrogen isotopes with metals/alloys result in formation of corresponding hydrides, deuterides and tritides with same stoichiometry. However, the lattice dynamics of the hydrides, deuterides and tritides differ considerably due to the difference in their zero point vibrational energies, as discussed in Section-1.6. Also, the difference in molecular masses of hydrogen, deuterium and tritium results in different values of their standard entropies. The overall effect of differences in zero point energies and the standard entropies leads to different values of Gibbs free energies of formation for these analogues compounds, which in turn, gives different values of equilibrium pressures for H_2 , D_2 and T_2 at a particular temperature [40]. Hence, it is important to investigate the hydrogen isotope effect on the storage behaviour of these metals and alloys.

1.8 Motivation and Objective of the present investigation

Adding the third element is considered an effective way to elevate the equilibrium dissociation pressure and/or decrease the dehydrogenation temperature of ZrCo based hydrides, thus improving the anti-disproportionation property of ZrCo based alloy. This has led to the onset of consolidated efforts to find a suitable ternary alloy for storage, supply and recovery of hydrogen isotopes. In the present thesis, a systematic approach has been applied to investigate the effect of ternary alloying on the hydrogen isotope storage properties of ZrCo alloy.

Considering the hydride forming ability and chemical properties of elements, Ti can be considered as suitable substitutes for Zr in ZrCo alloy. Similarly, Fe and Ni can be considered as suitable substitutes for Co in ZrCo alloy. Hence, this thesis attempts to study the effect of substitution of Ti, Fe and Ni on the hydrogen storage properties of ZrCo alloy. In this context, ternary alloys $Zr_{1-x}Ti_xCo$ and $ZrCo_{1-x}M_x$ ($M = Ni$ and Fe) were prepared and characterized by different techniques like XRD, SEM, EDS and Elemental mapping. The hydrogen isotope storage behavior of Zr-Co-M ternary alloys were investigated by generating the hydrogen/deuterium desorption Pressure-Composition Isotherms (PCIs) by employing Sieverts' type volumetric apparatus. The thermodynamic parameters of the hydrogenation reactions and their corresponding isotopic effects were evaluated. Hydrogen induced disproportionation behavior of Zr-Co-M ternary alloys were investigated by hydrogen absorption-desorption cyclic life and isothermal studies. The phenomenon of hydrogen induced disproportionation in different Zr-Co-M ternary alloys was further investigated by employing the structural elucidation technique, neutron powder diffraction (NPD). The extensive work carried out in this thesis enable to identify a suitable ternary substituent for effective storage, supply and recovery of hydrogen isotopes in particular tritium.

CHAPTER 2

EXPERIMENTAL

2 Experimental

2.1 Synthesis of materials

2.1.1 Preparation of alloys: Arc melting method

Arc melting method was used to synthesize a series of Zr-Co-M (M=Ni, Fe and Ti) ternary alloys. An arc melting furnace converts the electrical energy into the thermal energy which is in turn utilized to melt the charge of raw materials to form an alloy [72]. Arc melting unit consists of three main parts: power source, chiller and vacuum unit. The power source is used to generate the arc between a tungsten electrode and a copper hearth (having crucible to hold raw material) by applying a low voltage and high ampere current which results in large tension between two electrodes. In an arc melting unit, pure elements of the alloy in the desired ratio stoichiometry can be heated up to a temperature more than 2000°C and the arc temperature can be controlled by the current applied between the two electrodes. The vacuum unit attached to this arc melting unit consists of a diffusion pump backed by rotary vacuum pump and a vacuum of 10^{-6} mbar can be attained by this unit. This is used to evacuate the arc melting chamber and then back filled with inert gas like argon or helium. Evacuation and filling of chamber with inert gas avoids oxidation of molten metal and alloys. Due to the high work potential of helium it is difficult to generate the arc in helium atmosphere than in argon atmosphere. Hence, in general, the melting is performed in high purity argon atmosphere. The cold water circulation from the chiller unit cools both the copper hearth and the electrode. The alloy ingot formed by this method is not perfectly crystalline in nature due to the irregular cooling of sample when the arc is broken off. Bottom of the sample is cooled faster, due to direct contact with water-cooled copper hearth, than the top of the sample and this result in amorphous nature of sample. Fast cooling of the liquid melt by chilled water

causes quenching of sample, resulting in presence of multiple phases and amorphous solidified liquid. Therefore, to attain an equilibrium ambient temperature phase, the arc-melted samples were heat treated. For which the samples are encapsuled in quartz and heated at desired temperature for considerable duration and then quenched to get the desired phase, homogeneity and crystallinity.

For the present study, alloys of compositions $\text{ZrCo}_{1-x}\text{Ni}_x$ ($x = 0.0, 0.1, 0.2$ and 0.3), $\text{ZrCo}_{0.9}\text{Fe}_{0.1}$ and $\text{Zr}_{1-x}\text{Ti}_x\text{Co}$ ($x = 0.1, 0.2$ and 0.3) were prepared by arc-melting of stoichiometric mixtures of high purity metals. After melting of the stoichiometric mixtures of high purity metals it solidified due to cooling of copper hearth. In order to improve the compositional homogeneity, the ingot was turned around, without breaking the vacuum, and re-melted six times in a water cooled copper hearth under a high purity argon atmosphere. The cast ingot were wrapped in a titanium foil and annealed in an evacuated sealed quartz tube at 973 K for 3 days (where titanium worked as getter for residual oxygen in the ampoule) and water quenched to room temperature.

2.1.2 Activation of alloys

Most of the hydrogen isotope storage materials require activation prior to their intended use. Activation of the alloy is a process in which different treatments are given to the sample to achieve the repeatable reversible hydrogen absorption-desorption behavior. Generally surface of alloys are covered by adsorbed impurities and an oxide layer. These impurities act as a barrier for absorption of hydrogen, therefore, it is essential to overcome the effect of surface impurities. For this purpose, firstly the sample is heated at the elevated temperature under very high vacuum, of the order of 10^{-6} mbar or better. Then the sample is exposed to hydrogen at elevated temperature and pressure to initiate the reaction of hydrogen with the sample. Hydrogenation of sample causes significant increase in the lattice volume which

results in the decrepitation of the bulk host material into fine powder and provides a fresh metal surface for further absorption of hydrogen.

In the present study, for the activation of all Zr-Co-M ternary alloys, the sample was loaded in the reaction vessel of in-house designed Sieverts' type volumetric apparatus and out gassed at 773 K in a vacuum of around 10^{-5} Pa for 4 hours. Thereafter, high pure hydrogen gas was introduced into the reaction vessel at 573 K and temperature was lowered to room temperature, while keeping the reaction vessel inside the furnace. In this process, absorption of hydrogen by sample started around 573 K and the bulk alloy was converted into the fine powder of hydride which further provided the fresh alloy surface for absorption of hydrogen. Once, the hydrogen absorption started the temperature was lowered and the heat generated by exothermic absorption of hydrogen was sufficient to activate the further absorption of hydrogen by the alloy. This hydrogen absorption process continued till all the alloy was converted to hydride phase. Thereafter, the hydride phase was dehydrogenated at 773 K for three hours and at 873 K for one hour, under high vacuum ($\sim 10^{-5}$ Pa). This process was repeated twice to achieve the activated alloy of repeatable reversible hydrogen absorption-desorption behavior.

2.1.3 Preparation of hydrides/deuterides

For the preparation of the Zr-Co-M hydride/deuteride phases, the activated alloy sample was loaded into the reaction vessel of Sieverts' type volumetric apparatus (PCT Pro-2000, SETARAM Instrumentation, France) and a known amount of hydrogen/deuterium gas was introduced into the system, at room temperature, to form the corresponding hydride/deuteride phase. The hydrogen/deuterium concentration in the hydride/deuteride phase was calculated by monitoring the change in pressure with time and using the volume-pressure relation at constant temperature.

2.2 Characterization techniques

Various characterization techniques were used for the characterization of the alloys, as well as their hydrides and deuterides. The alloys and their hydrides/deuterides were characterized by X-ray powder diffraction (XRD) method. The surface morphology of alloys and their hydrides/deuterides was investigated by employing the Scanning Electron Microscope (SEM). The homogeneity of the alloys was investigated by compositional analysis at different morphological positions of the alloy by Energy Dispersive X-ray Spectroscopy (EDS) and elemental mapping. The brief description of characterization techniques used is as follows.

2.2.1 X-Ray Diffraction (XRD) Technique

X-ray diffraction is a non-destructive solid state characterization technique for characterization of the crystalline materials. This technique is used to get insight about the phase composition of materials and crystallographic information of different phases. In X-ray diffraction, electromagnetic radiation, monochromatic X-rays, with wavelength of the order of inter atomic spacing are elastically scattered by the electron cloud of the atoms in a crystal. Scattered X-rays are completely in-phase if the path difference is equal to an integer multiple of wavelength of the X-ray (λ). This increases the intensity of the scattered X-ray. Similarly, out-of-phase X-rays result in reduction of intensity. This change in intensity of the scattered X-rays gives a diffraction pattern, which is related with lattice parameters. This phenomenon produces the diffraction peaks at angles defined by the Bragg's law [73];

$$n\lambda = 2d \sin\theta \quad (2.1)$$

where n is the integer, λ is the wavelength of X-ray, 2θ is the angle between the incident beam and diffraction plane and d is the inter-planar distance for a particular set of plane with Miller indices (hkl).

The X-ray powder diffraction measurements of the present powder samples were carried out using a theta–theta geometry diffractometer (supplied by GNR Analytical Instruments Group, Italy; Model: EXPLORER). The CuK_α radiation ($\lambda = 1.5406 \text{ \AA}$) was used for recording of room temperature XRD patterns. The diffractometer operated at the power level of 1.6 kW (40 kV and 40 mA) and was equipped with the secondary graphite monochromator in the diffracted beam. The room temperature powder XRD patterns were recorded in the 2θ range of $20\text{--}80^\circ$ with a step of 0.02° and 3 seconds counting time. X-ray powder diffraction patterns of some of the samples, where the sample quantity was very less due to experimental restrictions, were also recorded using the Rotating Anode X-ray facility of Bhabha Atomic Research Centre (BARC), Mumbai, India.

2.2.2 Scanning Electron Microscope (SEM)

A scanning electron microscope (SEM) is a type of electron microscope that produces images of a sample by scanning it with a focused beam of electrons. The electrons interact with atoms in the sample, producing various signals that contain information about the sample's surface topography and composition. The focused beam of electrons is generally scanned in a raster scan pattern and the signals emitted from the surface are collected. Thereafter, the beam's position is combined with the detected signal to produce an image [74]. When a high-energy primary electron beam interacts with an atom of specimen it undergoes either inelastic scattering with atomic electrons or elastic scattering with the atomic nucleus thus resulting in a number of interactions that produces different types of electrons and photons. Different electron-matter interactions can be classified as follows [75];

- a) Elastic scattering of electrons by atomic nuclei of the sample results in generation of back-scattered electrons (BSE). The probability for elastic scattering increases with Z^2 and hence BSEs are useful for generating images based on Z-contrast.

- b) Inelastic scattering of electrons by sample atoms results in low-energy secondary electrons (SE) which are used for providing the topographic information of the sample surface.
- c) Inelastic scattering of electrons by sample atoms results in X-ray generation (characteristic and Bremsstrahlung background X-rays) from lower sample depths. The characteristic X-rays are useful for chemical analysis of the sample.
- d) Inelastic scattering results in Auger electrons emitted from sample atoms near the sample surface which are useful for surface chemical analysis.

For imaging and chemical analysis using SEM, the particles generated from different electron-specimen interaction should reach to the detector situated above the sample surface. The order of relative energies of the generated particles is as follows [75];

Auger electrons < SE < BSE < X-rays

The Auger electrons emitted from deeper regions of the sample lose their energy through collisions with sample atoms and they can't penetrate the surface. Thus only surface Auger electrons can be detected and thereby making the Auger Electron Spectroscopy (AES) a very sensitive technique to probe the chemical composition of only the top 50-100 Å (i.e., 15-30 monolayers). In comparison, the maximum escape depth of secondary electrons has been estimated as 5 nm in metals and 50 nm in insulators [75]. The principal images produced in the SEM are of three types: secondary electron images, backscattered electron images, and elemental X-ray maps. Secondary and backscattered electrons, produced by different mechanisms, are conventionally separated according to their energies.

In the present study, the microstructure and surface morphology of all Zr-Co-M ternary alloys and their corresponding hydride/deuteride phases were analyzed by Scanning Electron Microscope (SEM, SERON INC South Korea, Model ATS 2100). SEM imaging of powder

samples were carried out by spreading the powder samples on a adhesive carbon tape which is conventionally used in SEM for conduction purpose.

2.2.3 Energy-dispersive X-ray spectroscopy (EDS) and Elemental mapping

Energy-dispersive X-ray spectroscopy (EDS) is an analytical technique used for the qualitative and quantitative analysis of the elements present in the sample. As discussed in Section 2.2.2, the characteristic X-rays generated by the electron-matter interaction are used for chemical analysis of the sample. The number and energy of the characteristic X-rays can be measured by an energy-dispersive spectrometer. Chemical composition of the sample is determined by comparing the intensities of characteristic X-rays from the sample material with intensities from a standard sample of sample elements with known composition.

In the present study, the homogeneity of all Zr-Co-M ternary alloys was investigated by compositional analysis at different morphological positions of the alloy by EDS (Oxford Instrumentation, UK, Model Number INCAE350) and by elemental mapping. Flat and polished alloy sample were used for EDS and elemental mapping.

2.2.4 Neutron powder diffraction (NPD) technique

Neutrons, being an uncharged particle, interact with matter in fundamentally different way than the X-rays. X-rays are scattered by the electron cloud of the atoms whereas the neutrons are scattered by the atomic nuclei. The strength of scattering can be expressed as scattering cross section or scattering length. X-ray scattering is dependent on the number of electrons surrounding the nucleus, whereas, neutron scattering is governed by the strength of interaction between neutron and nucleus of scattering atom. Hence, In X-ray there is a linear increase in atomic scattering factor with atomic number (Z) of scattering atom. However, there is no systematic correlation between the atomic number (Z) of the scattering nuclei and neutron scattering length. Even scattering from different isotopes of the same element can differ significantly. That's the reason, why it is difficult to see the scattering of light atoms by

X-ray diffraction technique? Also it is very difficult to distinguish the neighboring elements in the periodic table by X-ray diffraction. Another important point with regards to neutron scattering is that, the neutron scattering lengths do not change with change in scattering angles. On the other hand, X-ray scattering factor decreases with increase in scattering angle. Also, neutrons have a magnetic moment which in turn is utilized to determine the magnetic ordering and magnetic structures of materials by employing neutron scattering technique [76].

Neutron powder diffraction (NPD) is widely used for structural characterization of hydrogen isotope storage materials. A detailed discussion about the use of X-ray and neutron diffraction in structural characterization of metal hydrides is presented by B.C. Hauback [76] and D.K. Ross [77]. It is important to note that there is a significant difference in the scattering behavior of hydrogen and deuterium. Any element or isotope consists of coherent as well as incoherent scattering cross sections, σ_{coh} and σ_{inc} respectively. In neutron diffraction, coherent scattering is exploited which contributes to the Bragg peaks, whereas the incoherent scattering contributes only to the background. Hydrogen (H) has very high incoherent scattering ($\sigma_{\text{coh}} = 1.8$ barn and $\sigma_{\text{inc}} = 80.2$ barn) [78], and this gives mainly a big background in the neutron diffraction data. On the other hand, deuterium (D) gives mainly coherent scattering ($\sigma_{\text{coh}} = 5.6$ barn and $\sigma_{\text{inc}} = 2.0$ barn) [78], which contributes to the Bragg scattering. Therefore, for structural studies of hydrides by neutron diffraction deuterium is used in lieu of hydrogen.

| | |
|--------------------|--|
| Beam hole no. | T1013 |
| Monochromator | Ge (331) |
| Wavelength | 1.244 Å |
| Beam size | 4.0cm× 1.5 cm |
| Flux at sample | 8.5×10^5 n/cm ² /sec |
| Scattering angle | $4^\circ < 2\theta < 140^\circ$ |
| Q range | $0.4 - 9.4 \text{ Å}^{-1}$ |
| $\Delta d/d$ | $\sim 0.8 \%$ |
| Detector | 5 (1d-PSD) |
| Sample environment | 5 – 300K |

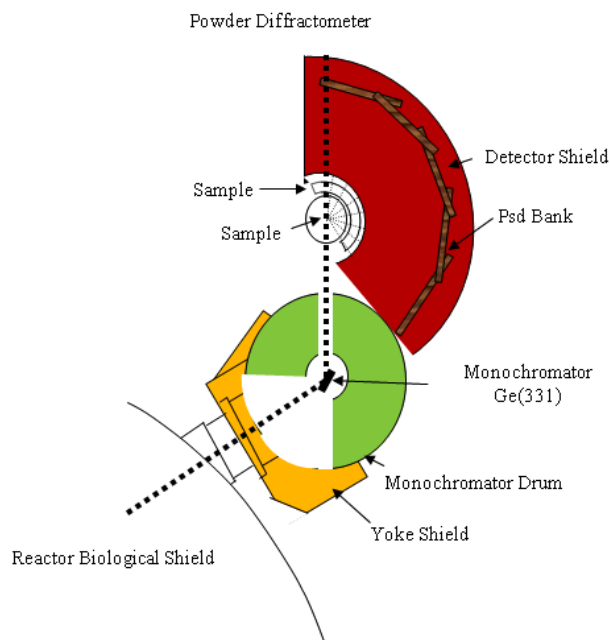


Figure 2.1: Schematic and the instrument parameters of neutron powder diffractometer.

A neutron powder diffraction set-up requires a neutron source, which can be a reactor or spallation neutron source. In the present study, the neutron powder diffraction (NPD) patterns of Zr-Co-M ternary alloy deuterides were recorded on the PD2 neutron powder diffractometer ($\lambda = 1.2443 \text{ Å}$) at Dhruva reactor, Bhabha Atomic Research Centre, Mumbai, India. A schematic and the corresponding instrument parameters of neutron powder diffractometer used is shown Figure 2.1. The resolution ($\Delta d/d$) of the powder diffractometer is 0.8%. The sample used for this measurement was in powder form and it was densely packed in a vanadium container (1cc volume). The detector bank consists of ^3He based five linear position sensitive detectors covering an angular range 0 to 140° . The step size was 0.05° . The data was recorded for about 5 hours. The neutron powder diffraction pattern was analyzed using FULLPROF program [79].

2.2.5 Data treatment method

2.2.5.1 Phase identification

Every crystalline phase has unique structural information like unit cell dimensions and the atomic arrangement within the unit cell, which gives rise to a unique powder X-ray diffraction pattern. This powder X-ray diffraction pattern can be considered as a ‘fingerprint’ of the material and therefore can be used for phase identification by comparing measured diffraction pattern with those reported in the database. The most efficient computer searchable crystallographic database available is the PDF-database from the International Centre for Diffraction Data (ICDD) [80].

2.2.5.2 Structure refinement - the Rietveld method

Rietveld refinement is a widely used technique for the refinement of structural data using powder diffraction patterns. H. M. Rietveld [81, 82], developed this method mainly for refinement of constant wavelength neutron diffraction data. Later on the Rietveld method was also applied for X-ray diffraction [83]. In the present study, Rietveld refinement method has been used for refinement of both powder X-ray diffraction and Powder neutron diffraction data.

Rietveld refinement is a structure refinement technique which works on least squares refinement method that refines the experimental pattern against a calculated pattern until the best fit is obtained. In order to apply this method, a good starting structure model is required having as much structural information as possible.

Rietveld method, being a least-squares method, attempts to minimize the weighted, squared sum of differences between the observed and the calculated values. The function which is being minimized is given as [83];

$$S_y = \sum_{i=1}^n w_i (Y_i^{obs} - Y_i^{cal})^2 \quad (2.2)$$

Where, n is the number of measured data points, w_i is the weighing factor and Y_i^{obs} and Y_i^{cal} are the observed and calculated intensity at point i of the powder diffraction pattern, respectively. Calculated intensity (Y_i^{cal}) is a complex function comprising different parameters contributing to the diffraction pattern of material.

In order to determine the quality of the refinement or to see whether the ‘best fit’ has been achieved or not, different figures of merits are used. The most widely used are the reliability factor R , which can be defined as R_{wp} (weighted profile R -factor), R_p (profile R -factor) and R_{exp} (expected profile R -factor) [84].

$$R_{wp} = \sqrt{\frac{\sum_{i=1}^n w_i (Y_i^{obs} - Y_i^{cal})^2}{\sum_{i=1}^n (Y_i^{obs})^2}} \quad (2.3)$$

$$R_p = \frac{\sum_{i=1}^n (Y_i^{obs} - Y_i^{cal})}{\sum_{i=1}^n Y_i^{obs}} \quad (2.4)$$

$$R_{exp} = \sqrt{\frac{(n-p)}{\sum_{i=1}^n (Y_i^{obs})^2}} \quad (2.5)$$

Where, n is the number of observations and p the number of refined parameters.

The goodness of fit, the chi-squared parameter (χ^2) is given as;

$$\chi^2 = \left(\frac{R_{wp}}{R_{exp}} \right)^2 \quad (2.6)$$

For a better fit, the R_{wp} value should be as close as possible to the R_{exp} value, means that the χ^2 value should be as close to 1 as possible. The quality of fit can be examined using the graphical representation of observed and calculated diffraction patterns and their difference plot.

In the present study, X-ray powder diffraction and neutron powder diffraction patterns were analyzed using FULLPROF program [79]. WinPLOTR was used for graphical representation of observed and calculated diffraction patterns and their difference plot [85].

2.3 Hydrogen absorption-desorption measurement technique

There are various techniques available for investigating the hydrogen sorption-desorption properties of different materials. These can be broadly classified into three categories;

1. The Gravimetric method: It is based on the measuring of change in sample mass during the course of hydrogen absorption-desorption reaction. After incorporating necessary corrections, the measured weight is plotted as a function of hydrogen pressure to generate the pressure-composition isotherms (PCIs). Further details of this method can be found in the chapter written by D.P. Broom [86].

2. The Flowing volumetric method: It is based on the mass flow controllers and the amount of hydrogen absorbed/desorbed by the sample is determined by the amount of hydrogen flown inside/outside the reaction vessel. The details of this method can be found in [86].

3. The Manometric (Sieverts') method: It is the most common and widely used method for investigation of hydrogen storage properties of different materials. It is a very simple method and can be adopted in any normal laboratory even if it doesn't have any sophisticated equipment. It requires a gas handling system having a temperature and pressure measurement devices. A schematic diagram of a Sieverts' type volumetric apparatus is shown in Figure 2.2.

A conventional Sieverts' type volumetric apparatus comprises the following parts [86];

- | | |
|---|--------------------------|
| 1. Gas handling manifold | 6. Pressure transducer |
| 2. Reaction vessel | 7. Vacuum transducer |
| 3. Furnace for heating of reaction vessel | 8. Thermocouple |
| 4. Hydrogen and helium gas supply | 9. Vacuum pumping system |
| 5. Standard volume | |

For the present study two Sieverts' type volumetric apparatus were used. A low pressure Sieverts' type volumetric apparatus is indigenously designed and developed at our laboratory. High pressure Sieverts' type volumetric apparatus (PCT Pro-2000) was supplied by M/s. SETARAM Instrumentation, France. Picture of indigenously designed Sieverts' apparatus is shown in Figure 2.3 and the line diagram of High pressure Sieverts' apparatus is shown in Figure 2.4.

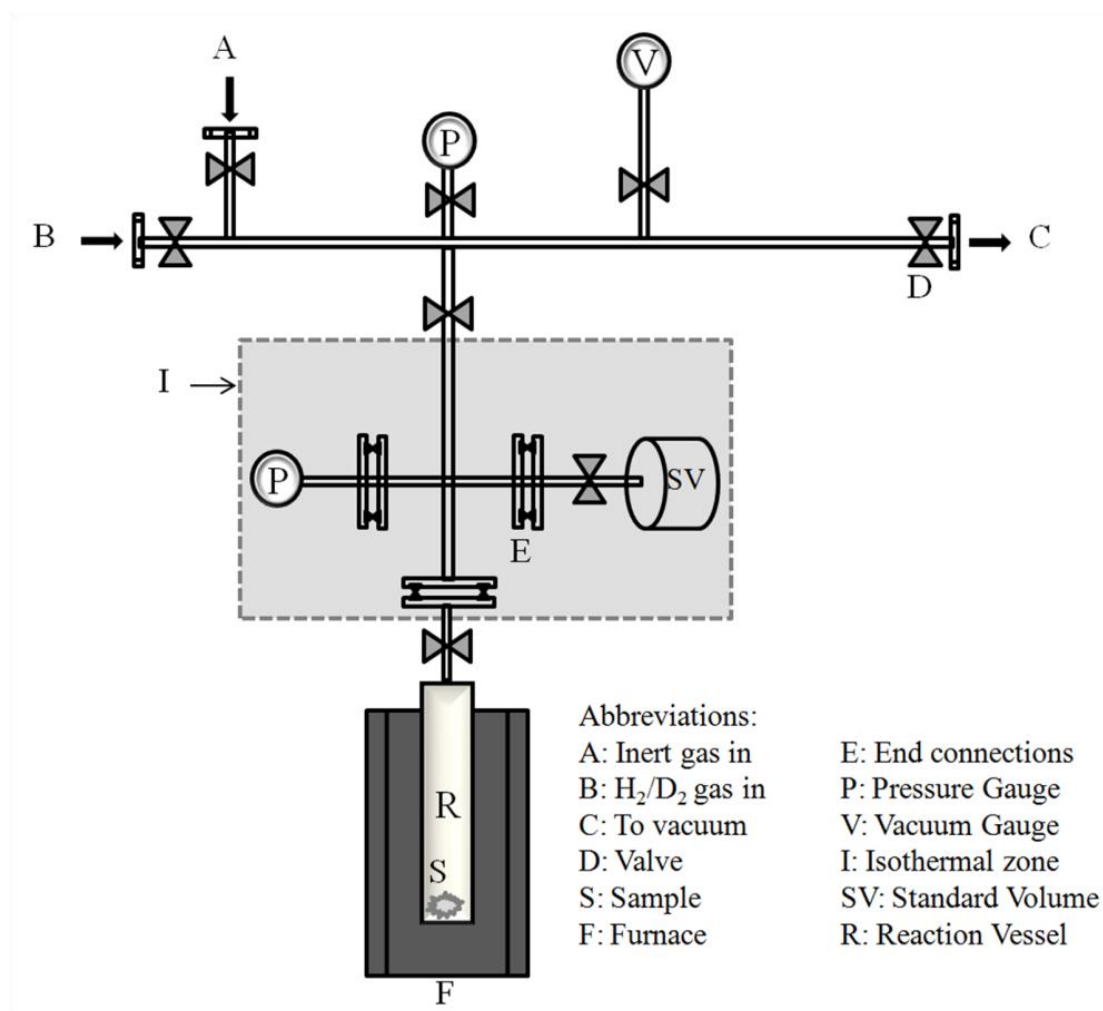


Figure 2.2: Schematic diagram of a Sieverts' type volumetric apparatus.



Figure 2.3: Indigenously designed and developed Sieverts' type volumetric apparatus.



Figure 2.4: Sieverts' type volumetric apparatus (PCT Pro-2000).

Indigenously designed Sieverts' apparatus was used for degassing and activation of all Zr-Co-M ternary alloys. Whereas, all other studies like synthesis of hydrides/deuterides, PCT measurement, cyclic life studies and isothermal disproportionation studies were carried out by employing the high pressure Sieverts' type volumetric apparatus.

2.4 Pressure-Composition-Temperature (PCT) studies

Thermodynamic properties of hydrogen storage materials govern a relation between hydrogen storage capacity, pressure and temperature which can be best represented by the Pressure-composition-temperature (PCT) measurements, here composition is synonymous of hydrogen concentration in the material. Thereby, PCT measurements are the most reported measurement in the literature. PCT measurements are the collection of pressure-composition isotherm (PCI) measurements at different temperatures. In a PCI, variation of concentration with equilibrium pressure is plotted at a constant temperature. The effect of temperature on hydrogen storage properties of any material can be determined by comparing PCIs at different temperatures.

In the present study, the pressure-composition-temperature (PCT) measurements were carried out using a conventional Sieverts' type volumetric apparatus (PCT Pro-2000, SETARAM Instrumentation, France). A known amount of the activated sample was loaded in to the reaction vessel of known volume of the Sieverts' apparatus and thereafter, hydrogen gas (purity 99.999%) at a known pressure was introduced at room temperature. The system was allowed to attain equilibrium by monitoring the pressure change with time. Equilibrium was considered to be attained only when no discernible change in pressure readings (within an error of $\pm 1\%$ of reading) were observed for a period of 3-4 hours. For lower pressure ranges (< 100 Pa), the equilibration time was increased to 5 hours or longer. The hydrogen concentration in the specimen was calculated from the pressure data. This hydride phase was

heated to the desired experimental temperature under a known overpressure in the system to generate hydrogen desorption pressure-composition isotherm (PCI). Desorption equilibrium was established by evacuating a known amount of hydrogen from the reservoir and allowing the system to re-attain equilibrium. This allows to simultaneously calculate the value of hydrogen concentration ($= H/f.u.$, $f.u. = Zr-Co-M$) and the corresponding equilibrium hydrogen desorption pressure at the experimental temperature. Thereafter, the value of $H/f.u.$ was altered by aliquoting a known amount of hydrogen from the reservoir and allowing the attainment of a new equilibrium. This process was repeated till the entire isotherm was generated. Following this procedure, hydrogen/deuterium desorption PCIs for all the Zr-Co-M ternary alloy systems were generated in the temperature range of 523-603 K with a step of 20 K. A real time hydrogen desorption PCI generation from the recorded pressure-concentration-time data at a particular temperature is shown in Figure 2.5. In this figure the upper graph is pressure vs. time plot and the resulting PCI curve is shown below. It can be seen from pressure vs. time diagram that a single PCI measurement consists of a series of pressure dose. The last point of each hydrogen desorption curve provides the concentration of hydrogen in the material at that temperature and equilibrium hydrogen pressure. Thus, by joining the last point of each desorption curve and calculating the corresponding hydrogen concentration, a PCI can be generated as shown in Figure 2.5.

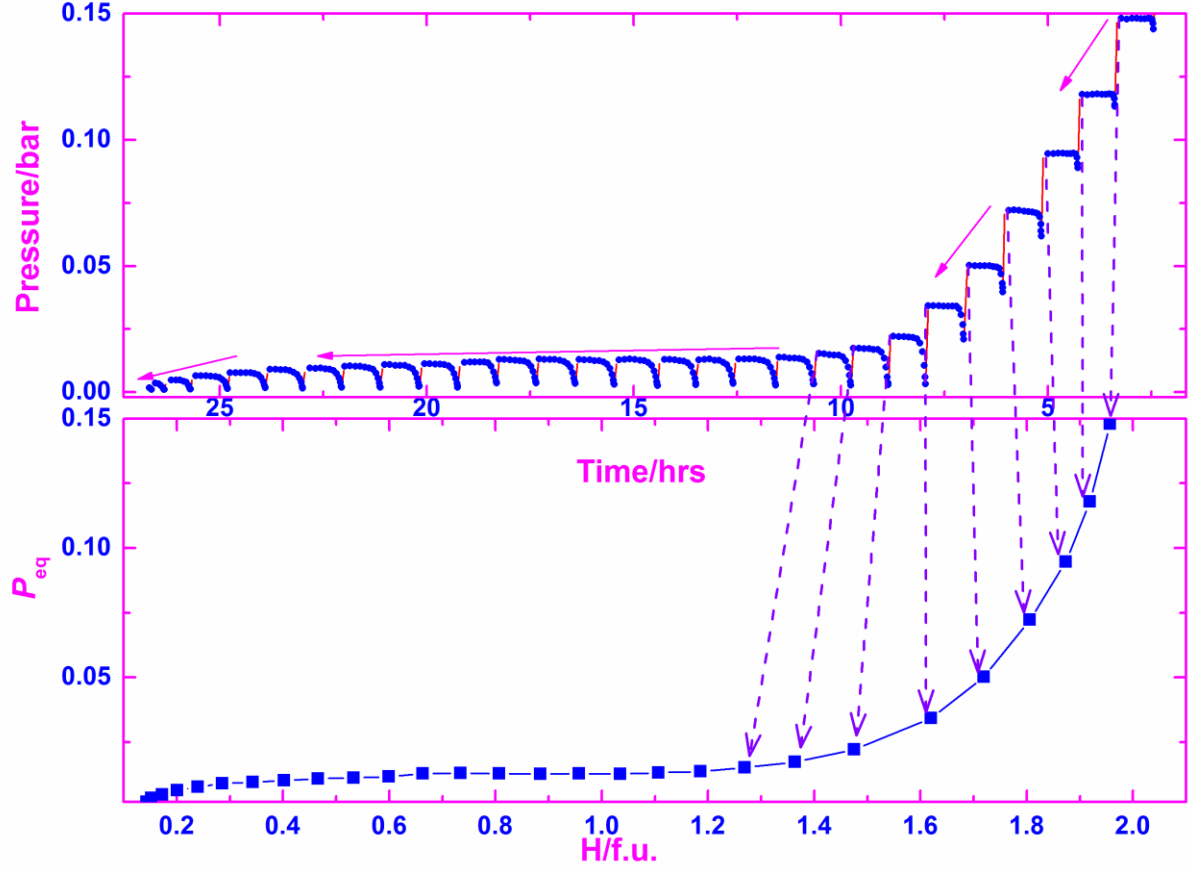


Figure 2.5: Generation of hydrogen desorption PCI for ZrCo alloy.

2.4.1 Calculation of hydrogen/deuterium absorption/desorption quantities in Sieverts' method

In Manometric (Sieverts') method the hydrogen/deuterium concentration in any material is determined by using the pressure-volume-temperature (PVT) correlations. As shown in Figure 2.2, the Sieverts' apparatus consists of a calibrated volume gas reservoir which is connected to a sample reactor. Since hydrogen/deuterium concentration in materials are measured indirectly using PVT correlations, the accurate volumes and temperatures of the calibrated gas reservoirs and sample holder must be known in advance. The position of thermocouple is fixed in such a way that the measured temperature is same as the sample temperature. Volume of sample holder, after loading of sample, is calibrated at experimental temperature using helium gas to accurately know the free gas volume in the sample holder.

Temperatures of the gas reservoir and sample holder are controlled using the PID temperature controller, to maintain them at constant (but not necessarily equal) temperatures. Thus, by fixing volume and temperature of the reservoir and sample holder, the pressures of the system can be measured using suitable pressure transducers to get isothermal pressure-concentration data [87].

A known amount of sample is loaded into the reaction vessel and free gas volume of sample holder is determined using the helium calibration method. Thereafter, the calibrated gas reservoir is filled with a known pressure of hydrogen. This hydrogen is allowed to react with sample by opening the valve of sample reactor and sufficient time is provided to reach the equilibrium in the system. If ΔP is the pressure drop due to absorption of hydrogen by sample the amount of hydrogen absorbed by the sample can be calculated as follows;

$$n = \frac{\Delta P \cdot V}{ZRT} \quad (2.7)$$

where, n is moles of hydrogen, V is the volume of system, z is the compressibility of hydrogen gas at temperature T K and R is the gas constant.

In general, for the present PCIs, the hydrogen concentration is represented by hydrogen to f.u. (formula unit) of the sample (H/f.u.).

$$\frac{H}{f.u.} = \frac{n}{n_s} \quad (2.8)$$

where, n_s is the moles of sample alloy.

For accurate measurements of hydrogen/deuterium concentration for generation of PCIs, the NIST Standard Reference Database [88] containing the latest compressibility factors for different gases were used. These NIST database are inbuilt in the software of Sieverts' type volumetric (PCT Pro-2000, SETARAM Instrumentation, France).

2.5 Cyclic life studies

The cyclic life of the hydrogen isotope storage material plays an important role in order to design the storage and delivery system. Hence, it is essential to investigate whether the hydrogen storage properties of any material stay relatively constant during the course of absorption-desorption cycling. In this context, hydrogen absorption-desorption cyclic life studies of $\text{ZrCo}_{1-x}\text{Ni}_x$ and $\text{ZrCo}_{0.9}\text{Fe}_{0.1}$ alloys were carried out at 583 K and up to 50 cycles using the Sieverts' type volumetric apparatus. Activated sample was loaded in to the reaction vessel of Sieverts' apparatus and the specimen temperature was set at 583 K at which cyclic life study was intended. A known amount of hydrogen was introduced into the reaction vessel kept at 583 K and after hydriding the hydrided sample was allowed to desorb hydrogen in a pre-evacuated large reservoir of known volume (~1 litre). This hydrogen absorption-desorption process was repeated up to 50 cycles. The hydride phase after 50 cycles was analysed by XRD. Thereafter, the cycled hydrided phase was dehydrogenated at 773 K for three hours and at 873 K for one hour, under high vacuum ($\sim 10^{-5}$ Pa) and the dehydrided phase was analysed by XRD. This process was followed for all the compositions of $\text{ZrCo}_{1-x}\text{Ni}_x$ and $\text{ZrCo}_{0.9}\text{Fe}_{0.1}$ alloys. These studies were not performed on the $\text{Zr}_{1-x}\text{Ti}_x\text{Co}$ alloys due to higher desorption equilibrium pressure of hydrogen for these alloys at 583 K.

2.6 Isothermal disproportionation studies

In order to find the best suitable ternary alloy among the alloys studied, it is required to study the isothermal disproportionation behavior of hydrides of these alloys at maximum possible desorption temperature under delivery conditions (under hydrogen pressure).

The isothermal disproportionation behavior of Zr-Co-M ternary alloys were studied at 750 K (maximum possible desorption temperature) under delivery conditions, above 1 bar over pressure of hydrogen. For this purpose, the activated alloy was loaded into the reaction vessel

of Sievert's apparatus and exposed to pure hydrogen to form the hydride. Thereafter, the hydride phase was heated to 750 K and the over pressure of hydrogen in the system was selected accordingly to get the hydrogen pressure above 1 bar. The system under this condition was kept in isothermal condition, at 750 K for 10 hours and then cooled to room temperature. Similar disproportionation studies were carried out for all Zr-Co-M ternary alloys keeping the identical experimental conditions. The Zr-Co-M hydrides before and after disproportionation studies were characterized by XRD to see the phase changes during the course of isothermal conditions.

CHAPTER 3

RESULTS AND DISCUSSION

3 Results and Discussion

3.1 Storage Behavior of ZrCo Alloy

3.1.1 Material Characterization

The XRD patterns of ZrCo and its hydride/deuteride phases are shown in Figure 3.1. The formation of ZrCo phase and its hydride/deuteride phases was confirmed by comparing their XRD patterns with the JCPDS (Joint Committee on Powder Diffraction Standards) files [89].

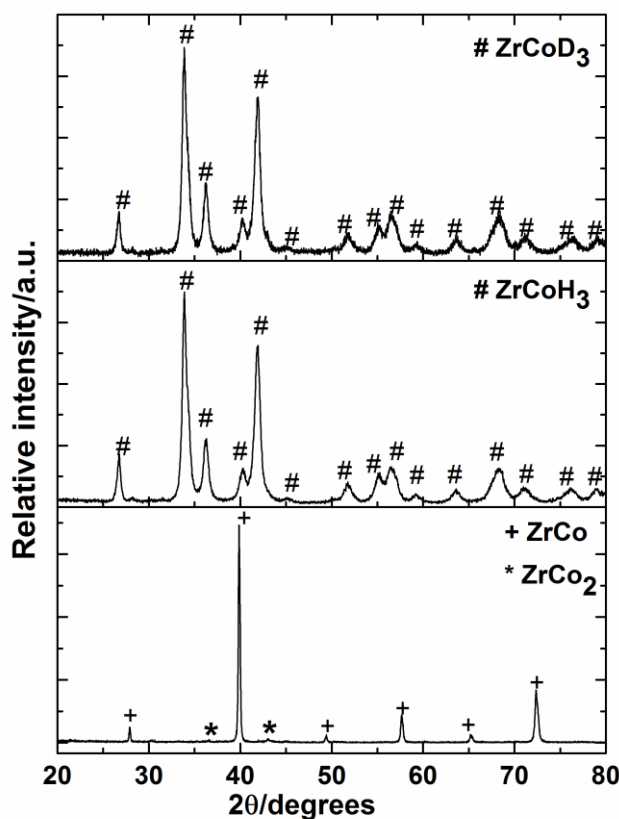


Figure 3.1: X-ray powder diffraction patterns of ZrCo and its hydride/deuteride.

It is evident from Figure 3.1, that a trace amount of ZrCo_2 phase is present in the ZrCo phase. Harris et al. [90] reported that, it is extremely difficult to prepare single phase of ZrCo and it is always accompanied by traces of ZrCo_2 phase. The Zr-Co phase diagram [91] reveals that ZrCo phase crystallizes as ordered CsCl-type b.c.c structure which exists over a very narrow range ($\leq 1\%$) of composition at all temperature and melts congruently. ZrCo phase forms eutectic with ZrCo_2 in the cobalt rich side. Also, ZrCo_2 is the most stable compound in the

Zr-Co system [91]. Hence, it is highly probable that upon cooling from melt to room temperature, a small fraction of ZrCo_2 phase will remain as impurity. The lattice parameter and phase abundances of the ZrCo alloy were calculated by Rietveld refinement of XRD data using the FULLPROF program [79]. Rietveld refinement pattern of ZrCo alloy is shown in Figure 3.2. In the present study the fraction of ZrCo_2 phase was found to be $\sim 1\%$. The lattice parameter of ZrCo was found to be $3.1957 \pm 0.0001 \text{ \AA}$ which is in very good agreement with the values reported in the literature, 3.196 \AA [89], 3.1963 \AA [90] and 3.1954 ± 0.0002 [92].

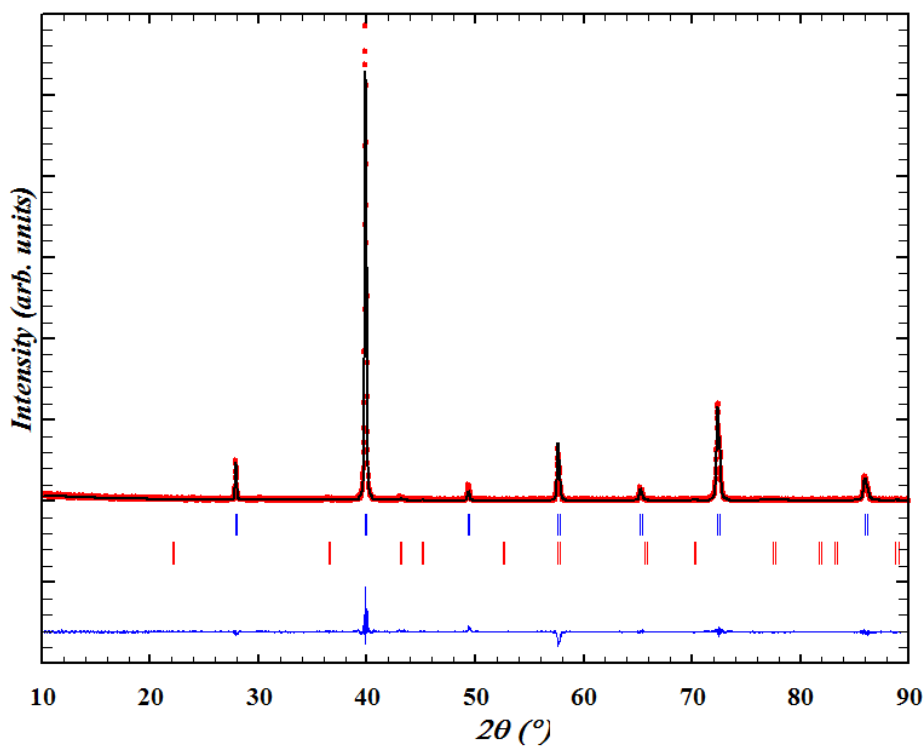


Figure 3.2: Rietveld refinement of XRD pattern of ZrCo alloy. The tick marks indicate ZrCo (top) and ZrCo_2 (bottom) phases.

The SEM images of ZrCo alloy and its hydride with different magnification are shown in Figure 3.3. It is evident from Figure 3.3 that ZrCo alloy exhibits a cleavage type surface whereas its hydride shows a cleavage type fracture surface. The cracks generated in the hydride phase are attributed to the lattice expansion of ZrCo alloy upon hydrogenation. The EDX spectra of ZrCo alloy is shown in Figure 3.4. The EDX microanalysis carried out at

different morphological positions of the alloy reveals an average composition over the entire sample and in accordance with the nominal composition ZrCo.

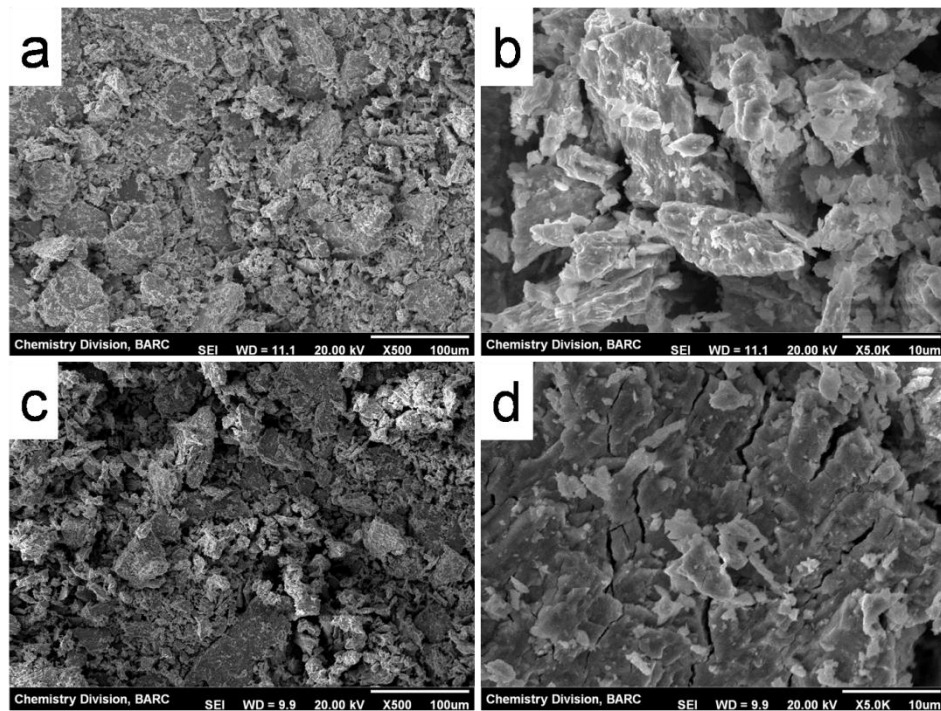


Figure 3.3: SEM images of ZrCo and its hydride at magnifications of 500X and 5000X; (a) and (b) ZrCo alloy; (c) and (d) ZrCo hydride phase.

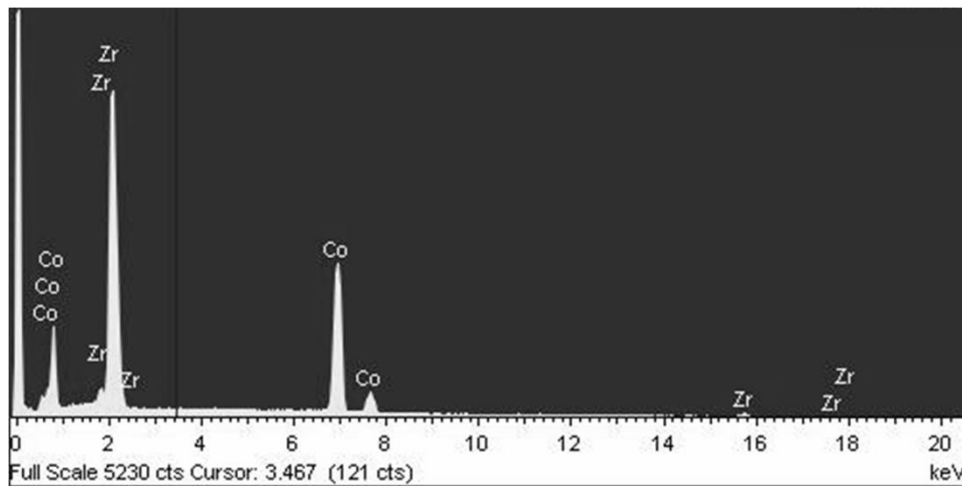


Figure 3.4: EDX spectra of ZrCo alloy.

3.1.2 Standardization of Sieverts' apparatus with PCT measurements on Pd-H₂ system

Prior to PCT measurements on actual systems, the accuracy of Sieverts' type volumetric apparatus was checked by performing the PCT measurements on palladium metal. Palladium metal powder (purity of 99.99% trace metal basis) was used for generation of hydrogen desorption pressure-composition isotherms (PCIs) in the temperature range of 354 to 424 K. First of all, the palladium sample was activated by hydrogen absorption-desorption method shown in Section-2.1.2. Thereafter, activated sample was loaded into the reaction vessel of Sieverts' type volumetric apparatus and hydrogen desorption pressure-composition isotherms were generated at four different temperatures in the range of 354 to 424 K. Hydrogen desorption PCIs for Pd-H₂ system are shown in Figure 3.5(a). A single desorption plateau was observed for all PCIs and the plateau width was found to decrease with increase in temperature. Using the plateau pressure data of all PCIs, a van't Hoff plot was constructed as shown in Figure 3.5(b). A linear relation was observed for temperature dependence of equilibrium plateau pressure and can be represented by van't Hoff relation;

$$\log(P/\text{Pa}) = -2175.7/(T/\text{K}) + 10.25 \quad (3.1)$$

By employing this van't Hoff relation, the enthalpy ($\Delta_r H^\circ$) and entropy ($\Delta_r S^\circ$) change for the de-hydrogenation of Pd hydride were deduced to be 41.7 ± 0.3 kJ/mole H₂ and 100.5 ± 0.4 J/(mole H₂·K), respectively. The obtained values of $\Delta_r H^\circ$ and $\Delta_r S^\circ$ change for the de-hydrogenation of Pd hydride are very close to the values 41.04 ± 0.4 kJ/mole H₂ and 97.5 ± 0.8 J/(mole H₂·K), respectively, reported in literature [93]. This confirms the accuracy of measurements by Sieverts' apparatus.

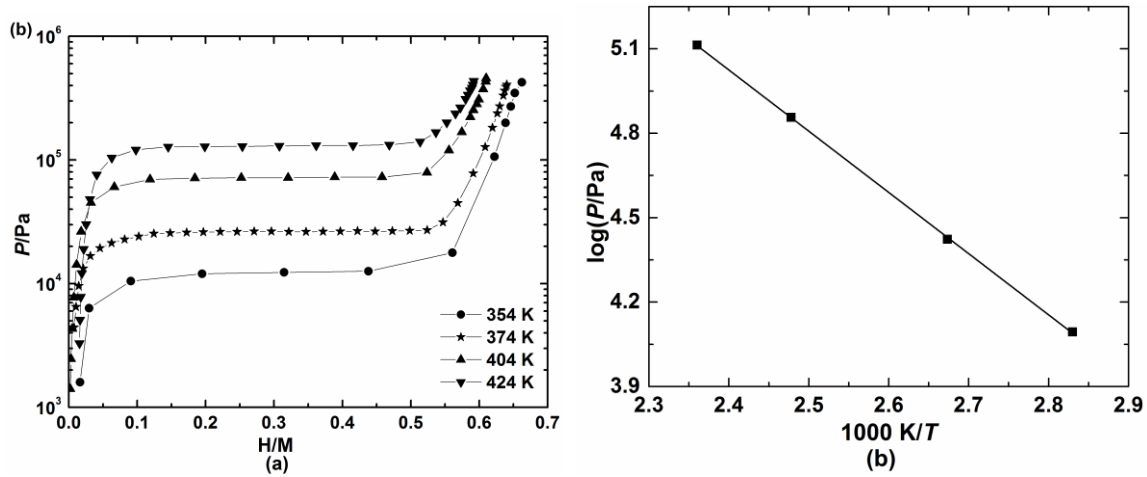
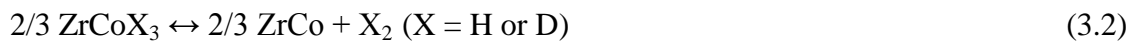


Figure 3.5: (a) Hydrogen desorption PCIs and (b) van't Hoff plot for Pd-H₂ system

3.1.3 Pressure-Composition-Temperature measurements on ZrCo-H₂/D₂ systems

Hydrogen/deuterium desorption PCIs at different experimental temperatures for ZrCo-H₂/D₂ systems are shown in Figure 3.6. It is evident from Figure 3.6, that ZrCo-H₂/D₂ systems exhibit a single desorption plateau at all experimental temperatures and the plateau width decreases with increasing the temperature. The reaction involved in de-hydrogenation/de-deuteration of ZrCo hydride/deuteride which results in single desorption plateau for all the isotherms can be written as:



The temperature dependence of the equilibrium plateau pressure for ZrCo-H₂ system is best represented by the van't Hoff plot, shown in Figure 3.7. Equilibrium plateau pressure values corresponding to X/f.u. = 1 were taken for construction of the van't Hoff plots. A linear relation was observed for the temperature dependence of equilibrium plateau pressure and is represented by the van't Hoff relations. The van't Hoff relations obtained for ZrCo-H₂/D₂ systems are as follows:

ZrCo-H₂ system

$$\log(P/\text{Pa}) = -4369/(T/\text{K}) + 11.4 \quad (3.3)$$

ZrCo-D₂ system

$$\log(P/\text{Pa}) = -4403/(T/\text{K}) + 11.5 \quad (3.4)$$

Using these van't Hoff relations the enthalpy ($\Delta_r H^0$) and entropy ($\Delta_r S^0$) changes for the /de-hydrogenation/de-deuteration of ZrCo hydride/deuteride were deduced at the average experimental temperature of 563 K and listed in Table 3.1.

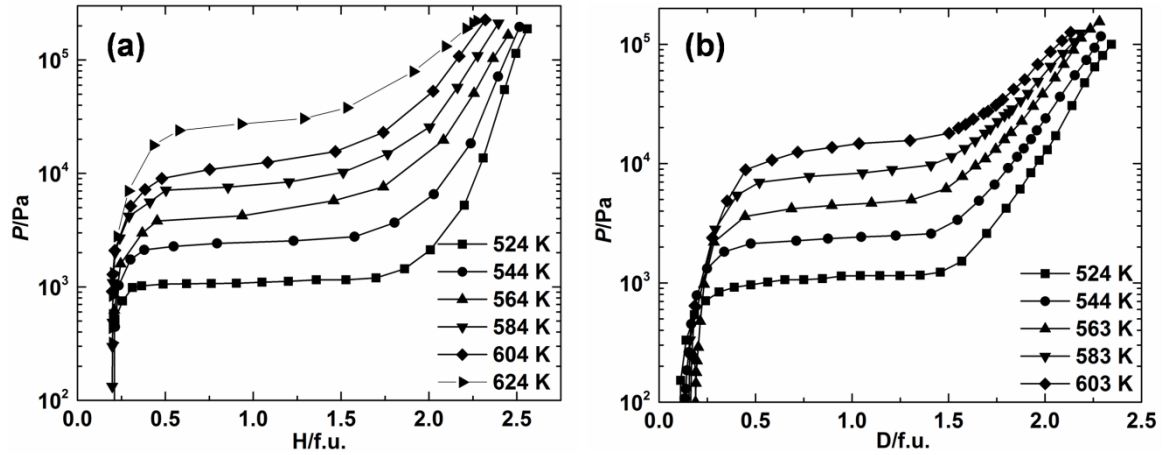


Figure 3.6: Hydrogen/deuterium PCIs for (a) ZrCo-H₂ and (b) ZrCo-D₂ systems

Several reports are available in the literature about the PCIs of ZrCo-H₂/D₂ systems both in hydrogen/deuterium absorption and desorption modes of measurements. The variation of desorption plateau pressure with temperature obtained in this study is compared with those reported in the literature [41, 68, 69, 94, 95] in Figure 3.7. It is evident from this comparison that there is considerable scatter in the reported data. However, the data obtained in this study are encompassed within the extreme limits of scattering reported in the literature. For a better assessment of PCT data, it is important to directly compare the thermodynamic parameters like enthalpy and entropy change of de-hydrogenation/de-deuteration reactions derived from the van't Hoff plots. This comparison is made in Table 3.1.

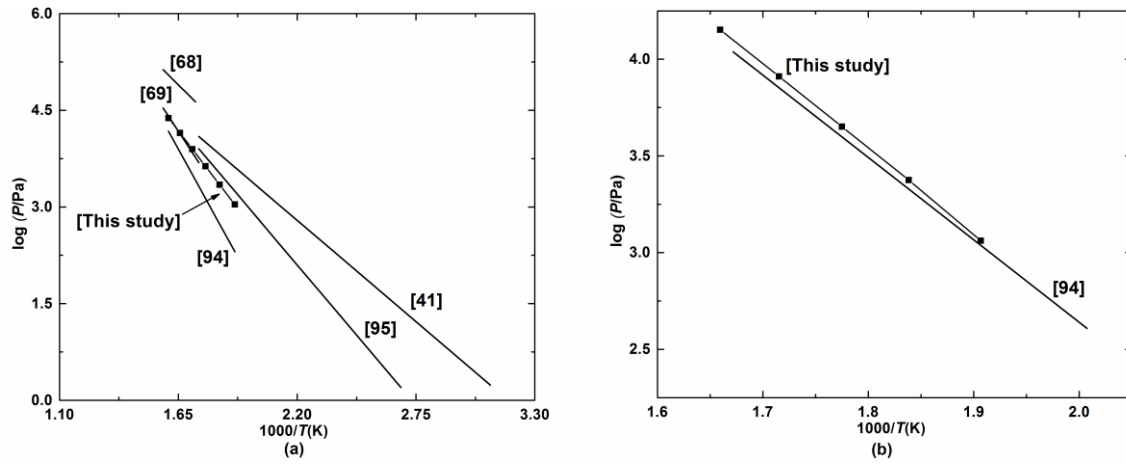


Figure 3.7: Comparison of van't Hoff plot obtained in this study with those reported in literature for the desorption isotherms of (a) ZrCo-H₂ and (b) ZrCo-D₂ systems

Table 3.1: Comparison of thermodynamic parameters of dehydrogenation reaction of ZrCo-H₂ system

| Authors/year [Ref.] | | $\Delta_r H/$ | $\Delta_r S/$ | x= | Temperature |
|------------------------------|-----------|------------------------|--------------------------|--------|-------------|
| | | kJ mole H ₂ | J/mole H ₂ ·K | X/f.u. | Range/K |
| Jat et al./2012 [This study] | Hydride | 83.7 ± 3.9 | 122.0 ± 3.9 | 1.0 | 524-624 |
| | Deuteride | 84.3 ± 0.6 | 124.5 ± 1.1 | 1.0 | |
| Bekris et al./2000 [41] | | 54.7 | 77.9 | 1.0 | 323-573 |
| Gongli et al./2007 [69] | | 97.8 | 145.5 | -- | 573-633 |
| Kost et al./1980 [94] | Hydride | 116.5 | 171.1 | 0.8 | 523-623 |
| | Deuteride | 81.6 | 117.9 | 0.8 | 503-588 |
| Heics and Shmayda/1992 | | 75.8 | 111.1 | 0.8 | 373-623 |
| [95] | | | | | |
| Zhuo et al./2006 [68] | | 63.1 | 101.9 | -- | 578-633 |

It is evident from Table 3.1 that the enthalpy and entropy data obtained in this study are very close to the average of all the reported literature data. Moreover, thermodynamic analysis of different metal/alloy-Hydrogen systems by Anderson [30] suggests that the entropy of dehydrogenation reaction should be $\sim 130 \text{ J}/(\text{mol H}_2 \cdot \text{K})$ which roughly corresponds to the gain in entropy due to the translational degree of freedom when hydrogen is desorbed from the metal hydride to the gas phase. In the present study the entropy of de-hydrogenation reaction was found to be $122 \pm 4 \text{ J}/(\text{mol H}_2 \cdot \text{K})$ which is close to the value suggested by Anderson [30]. This suggests that the data obtained in this study are reasonably accurate.

It is evident from Table 3.1 that the enthalpy of de-deuteration reaction is found to be higher than that of de-hydrogenation reaction. This trend can be attributed to the occupancy of hydrogen/deuterium atoms in tetrahedral sites of ZrCoX_3 [96]. It can be seen from Figure 1.10, that the tetrahedral potential profile is narrow and steeper than that of the octahedral potential profile [39]. Hence, the relative change in zero-point energy of deuterium from gaseous molecules to deuteride state is higher than that of hydrogen, means $|E_D| > |E_H|$, which in turn results in more enthalpy of reaction for reactions involving deuterium than that of hydrogen.

The free energy of hydrogen/deuterium desorption reaction ($\Delta_r G^\circ$) presented in Eq. 3.2 can be written as;

$$\Delta_r G^\circ = \Delta_r H^\circ - T\Delta_r S^\circ = -RT \ln(P/\text{Pa}) \quad (3.5)$$

where P is the equilibrium pressure of hydrogen/deuterium gas. In the form of equilibrium pressure the Eq. 3.5 can be written as;

$$\ln(P/\text{Pa}) = -\Delta_r H^\circ/RT + \Delta_r S^\circ/R \quad (3.6)$$

It can be seen from Eq. 3.6 that the overall hydrogen isotope effect on the equilibrium pressure of hydrogen arises from the interplay of two thermodynamic factors namely, entropy and enthalpy that control the relative stabilities of the corresponding isotopic hydrides. The

value of entropy of desorption reaction ($\Delta_r S^\circ$) for the heavier isotope hydride is more positive than the lighter ones, as the absolute entropies of hydrogen isotopes in the gas phase follow the order $S^\circ(\text{T}_2) > S^\circ(\text{D}_2) > S^\circ(\text{H}_2)$ [42], leading to a '*positive or normal*' isotope effect. The enthalpy of hydrogenation/de-hydrogenation reaction also decides the nature of isotope effect. When the $\Delta_r H^\circ$ of the lighter isotope hydride is more than the heavier isotope hydrides, a *normal* isotope effect is observed for the system, irrespective of temperature. In this case, the plateau pressure of the hydrogen isotopes will follow the trend: $p(\text{T}_2) > p(\text{D}_2) > p(\text{H}_2)$ at all temperatures. On the other hand, when the $\Delta_r H^\circ$ of the heavier isotope hydride is more than the lighter ones, a temperature dependent isotope effect is expected. Below a certain temperature, *inverse* isotope effect will be observed whereas above this temperature the isotope effect is normal. It is evident from Table 3.1 that there is no substantial isotopic effect on the enthalpy of dehydrogenation/de-deuteration for ZrCo-H₂/D₂ systems. Hence, the difference in equilibrium plateau pressure arises due to the difference in entropy of reaction for hydrides and deuterides. Since the entropy of desorption reaction ($\Delta_r S^\circ$) for deuterides is higher than that of hydrides, a normal isotope effect is observed for all the alloys. This leads to higher equilibrium pressure of deuterium than that of hydrogen. The normal isotope effect for ZrCo alloy can be confirmed from the lower desorption temperature (T_{des}) for the deuterides (677 K) than the corresponding hydrides (683 K). Based on these observation, it is expected that for ZrCo alloy the equilibrium pressure will follow the trend: $p(\text{T}_2) > p(\text{D}_2) > p(\text{H}_2)$.

3.2 Storage behavior of $\text{ZrCo}_{1-x}\text{Ni}_x$ alloys

3.2.1 Materials Characterization

The X-ray diffraction patterns of $\text{ZrCo}_{1-x}\text{Ni}_x$ alloys are shown in Figure 3.8. Phase identification of alloys was confirmed by comparing their XRD patterns with the JCPDS (Joint Committee on Powder Diffraction Standards) files [89].

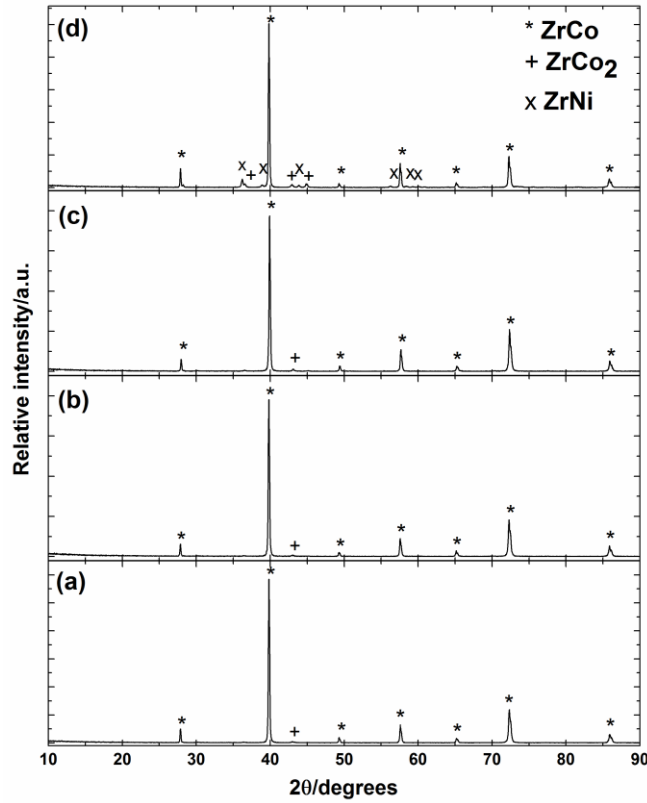


Figure 3.8: X-ray diffraction patterns of $\text{ZrCo}_{1-x}\text{Ni}_x$ alloys: (a) $x = 0$, (b) $x = 0.1$, (c) $x = 0.2$ and (d) $x = 0.3$

It is evident from X-ray diffraction patterns of $\text{ZrCo}_{1-x}\text{Ni}_x$ alloys, Figure 3.8, that trace amount of ZrCo_2 phase is present in all the alloys. This is in accordance with the observations of Harris et al. [90] that a single phase of ZrCo is extremely difficult to prepare. Figure 3.8 also confirms the formation of b.c.c. (CsCl-type) single cubic phase similar to ZrCo for all $\text{ZrCo}_{1-x}\text{Ni}_x$ alloys, except for $\text{ZrCo}_{0.7}\text{Ni}_{0.3}$ alloy. Further, it is observed from Figure 3.8 that trace amount of orthorhombic (CrB-type) phase, similar to ZrNi phase, is present in

ZrCo_{0.7}Ni_{0.3} alloy. This observation is also in accordance with the earlier studies by Carvalho and Harris [97], which reports that b.c.c. (CsCl-type) phase exists from $x = 0$ to 14 atom % . Further, the lattice parameters and phase abundances of the alloys were calculated by Rietveld refinement of XRD data using the FULLPROF program [79]. A representative Rietveld refinement pattern for ZrCo_{0.9}Ni_{0.1} alloy is shown in Figure 3.9. The refinement results for all the ZrCo_{1-x}Ni_x alloys are listed in Table 3.2.

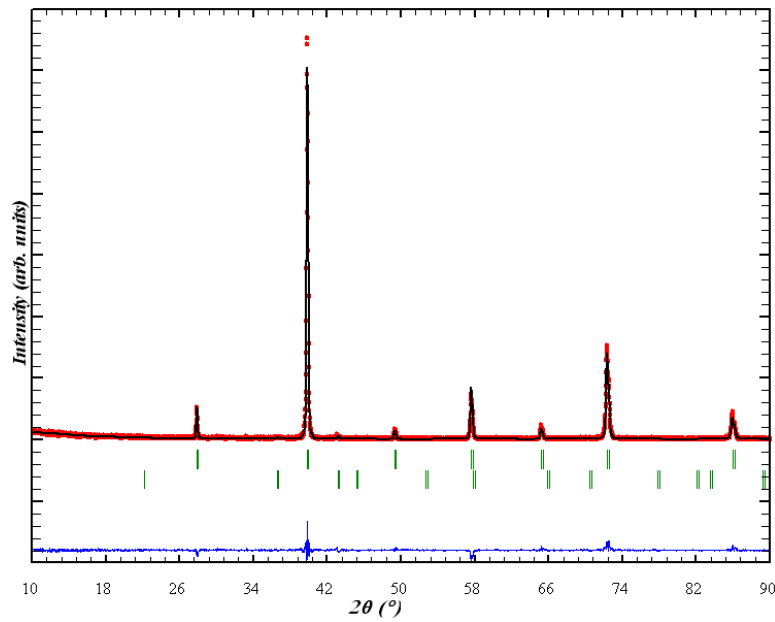


Figure 3.9: Rietveld refinement of X-ray diffraction pattern of ZrCo_{0.9}Ni_{0.1} alloy. The tick marks indicate ZrCo (top) and ZrCo₂ (bottom) phases

It can be seen from Table 3.2 that lattice parameter and unit cell volume of the b.c.c. ZrCo_{1-x}Ni_x alloys increases with increase in Ni content. Similar behavior of lattice expansion with increase in Ni content was also observed by Carvalho and Harris [97] and Hossain et al. [92]. The expansion of lattice with increase in Ni content indicates that the simple atomic size consideration can't explain the trend of lattice parameters. Hence, there may be the effect of number of electrons which in turn affect the filling of *d*-band. In ZrCo_{1-x}Ni_x alloys, the increase in Ni content will fill the *d*-like band which could lead to expansion of lattice due to

a relaxation of the bonding [92]. Lattice expansion anomalies were also reported in the palladium based alloys and attributed to “*d*-band effects” [98].

Table 3.2: Rietveld refinement results of X-ray diffraction patterns of $\text{ZrCo}_{1-x}\text{Ni}_x$ alloys.

| Alloy | Lattice parameters of major constituent phase (ZrCo Phase)/ Å | Cell volume of major constituent phase (ZrCo Phase)/ Å ³ | Phase abundances/ vol% | | |
|---------------------------------------|---|---|------------------------|-------------------|-------|
| | | | ZrCo | ZrCo ₂ | ZrNi |
| | | | phase | phase | phase |
| ZrCo | 3.1957 ± 0.0001 | 32.637 ± 0.002 | 99 | 1 | 0 |
| ZrCo _{0.9} Ni _{0.1} | 3.1971 ± 0.0042 | 32.678 ± 0.074 | 99 | 1 | 0 |
| ZrCo _{0.8} Ni _{0.2} | 3.1982 ± 0.0041 | 32.713 ± 0.072 | 97 | 3 | 0 |
| ZrCo _{0.8} Ni _{0.3} | 3.1988 ± 0.0020 | 32.731 ± 0.035 | 93 | 2 | 5 |

The XRD patterns of the hydride/deuteride phases are shown in Figure 3.10 & 3.11. Phase identification of hydrides/deuterides is carried out by comparing their XRD patterns with the JCPDS (Joint Committee on Powder Diffraction Standards) files [89]. This reveals that, all the $\text{ZrCo}_{1-x}\text{Ni}_x$ hydrides/deuterides forms a single orthorhombic phase similar to ZrCoH_3 .

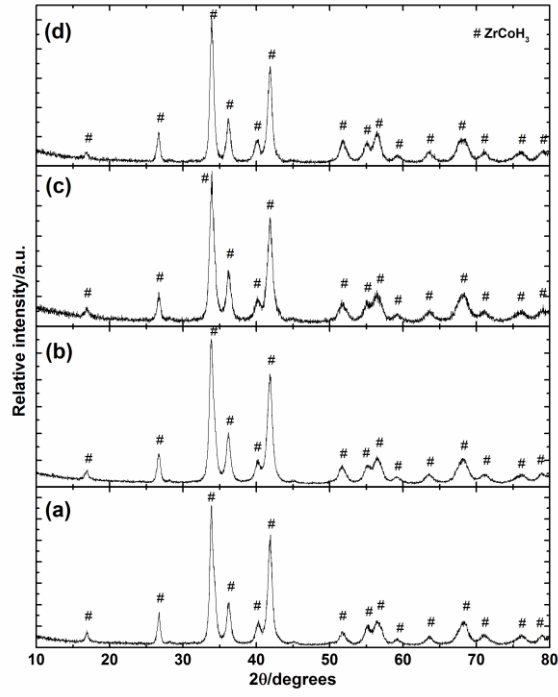


Figure 3.10: X-ray diffraction patterns of hydrides of $\text{ZrCo}_{1-x}\text{Ni}_x$ alloys: (a) $x = 0$, (b) $x = 0.1$, (c) $x = 0.2$ and (d) $x = 0.3$

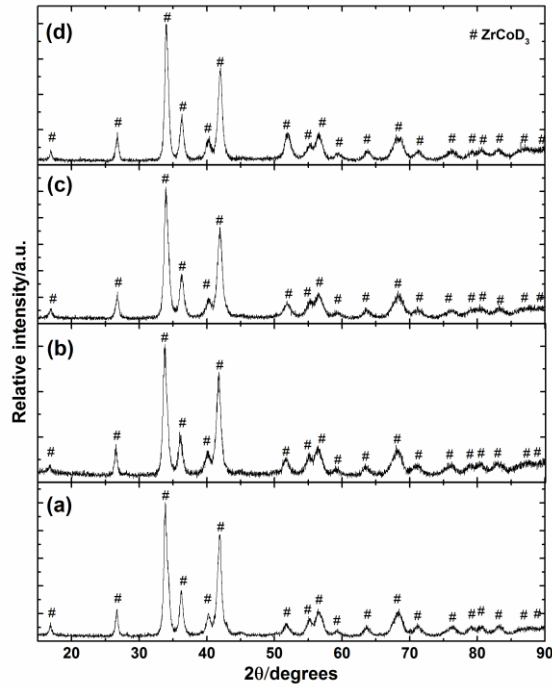


Figure 3.11: X-ray diffraction patterns of deuterides of $\text{ZrCo}_{1-x}\text{Ni}_x$ alloys: (a) $x = 0$, (b) $x = 0.1$, (c) $x = 0.2$ and (d) $x = 0.3$

The SEM images of all $\text{ZrCo}_{1-x}\text{Ni}_x$ alloys and the hydride of one composition with $x = 0$ are shown in Figure 3.12. It is evident from Figure 3.12 that all $\text{ZrCo}_{1-x}\text{Ni}_x$ alloys exhibit a cleavage type surface whereas the hydride phase shows a cleavage type fracture surface. The cracks generated in the hydride phase are attributed to the lattice expansion of ZrCo alloy upon hydrogenation.

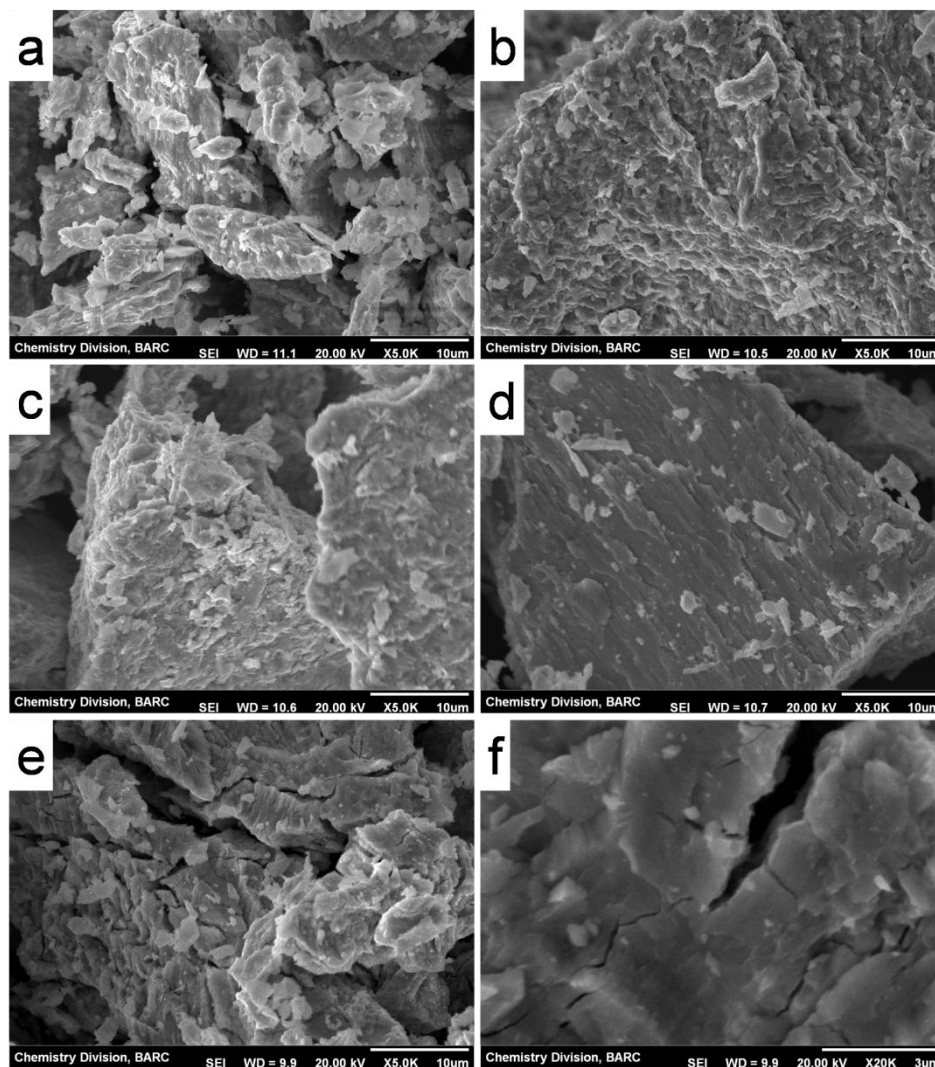


Figure 3.12: SEM images of $\text{ZrCo}_{1-x}\text{Ni}_x$ alloys at magnifications of 5000X: (a) $x = 0$, (b) $x = 0.1$, (c) $x = 0.2$, (d) $x = 0.3$, (e) & (f) hydride of $\text{ZrCo}_{0.9}\text{Ni}_{0.1}$ at magnifications of 5000X and 20000X, respectively

The EDAX microanalysis carried out at different morphological positions of the alloy reveals an average composition over the entire sample which is in accordance with the nominal composition of the alloys. The average chemical compositions of $\text{ZrCo}_{1-x}\text{Ni}_x$ alloys obtained by EDAX microanalysis are given in Table 3.3. The homogeneity of the alloys is confirmed by elemental mapping. The elemental mapping images of $\text{ZrCo}_{0.9}\text{Ni}_{0.1}$ alloy are shown in Figure 3.13. It is evident from Figure 3.13 that a uniform distribution of all three elements Zr, Co and Ni is observed, which reveals the homogeneous nature of the alloy. Similar pattern of uniform distribution of constituent elements is observed for all the alloys.

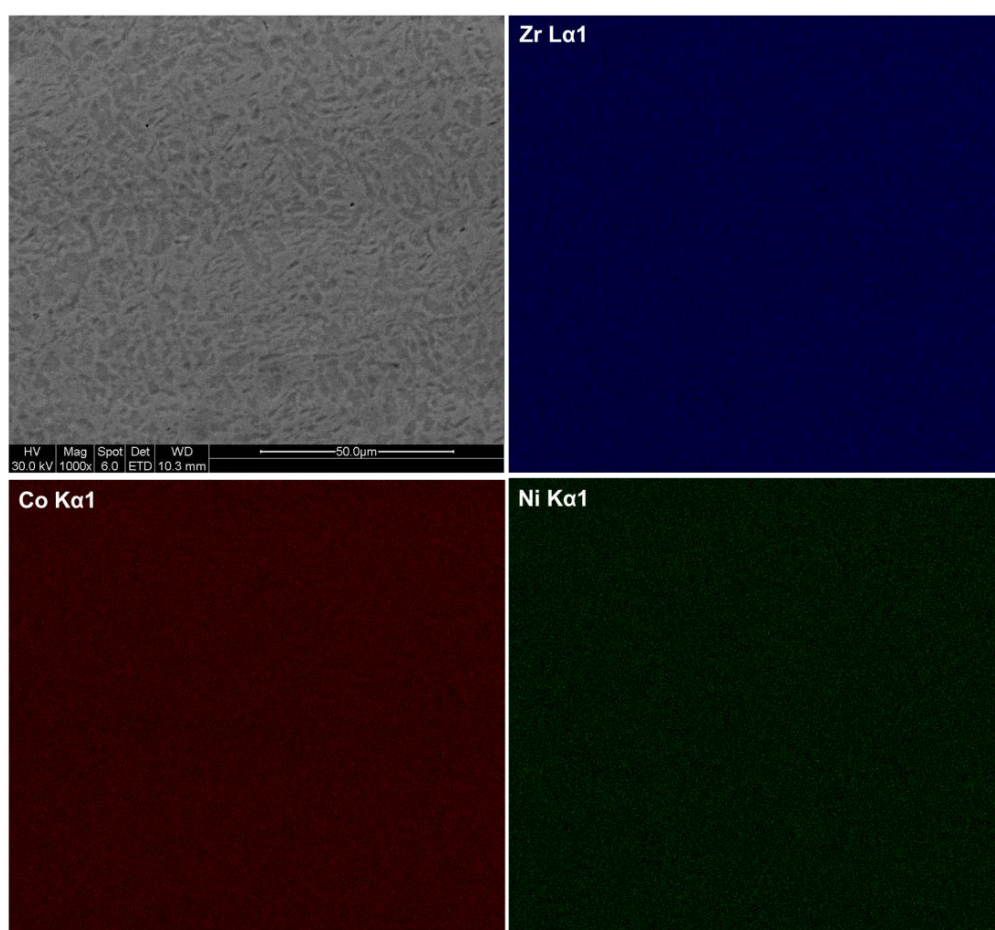


Figure 3.13: Elemental mapping images of $\text{ZrCo}_{0.9}\text{Ni}_{0.1}$ alloy.

Table 3.3: The average chemical compositions (atom %) of $\text{ZrCo}_{1-x}\text{Ni}_x$ alloys obtained by EDAX microanalysis.

| Alloy | Zr L α 1 | Co K α 1 | Ni K α 1 |
|------------------------------------|-----------------|-----------------|-----------------|
| ZrCo | 50.2 | 49.8 | |
| $\text{ZrCo}_{0.9}\text{Ni}_{0.1}$ | 50.5 | 44.3 | 5.2 |
| $\text{ZrCo}_{0.8}\text{Ni}_{0.2}$ | 49.8 | 40.7 | 9.5 |
| $\text{ZrCo}_{0.7}\text{Ni}_{0.3}$ | 50.7 | 34.5 | 14.8 |

3.2.2 Pressure-Composition-Temperature measurements on $\text{ZrCo}_{1-x}\text{Ni}_x\text{-H}_2/\text{D}_2$ systems

The hydrogen/deuterium desorption pressure-composition-temperature (PCT) profiles generated for $\text{ZrCo}_{1-x}\text{Ni}_x\text{-H}_2/\text{D}_2$ systems are shown in Figure 3.14 & 3.15. For better comparison the PCT data of $\text{ZrCo-H}_2/\text{D}_2$ system is also shown in Figure 3.14 & 3.15.

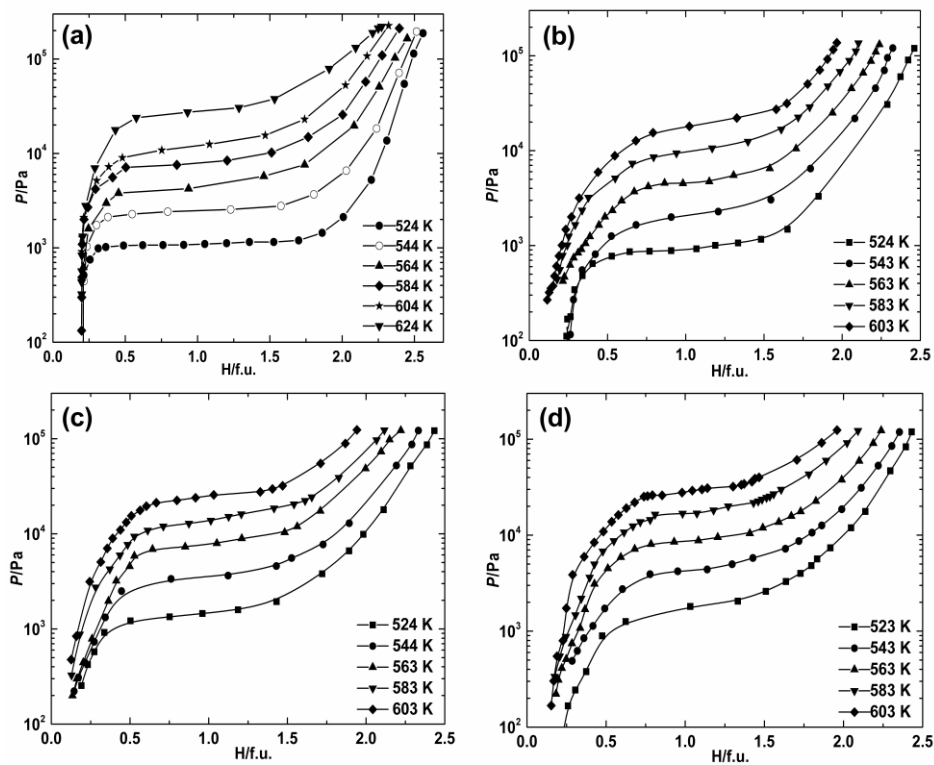


Figure 3.14: Hydrogen desorption pressure-composition isotherms for $\text{ZrCo}_{1-x}\text{Ni}_x\text{-H}_2$ systems: (a) $x = 0$, (b) $x = 0.1$ (c) $x = 0.2$ and (d) $x = 0.3$

It is evident from all the PCT data depicted in Figure 3.14 & 3.15 that in the temperature range of investigation, all the hydrides/deuterides show a single desorption plateau. The reaction involved in the process of de-hydrogenation/de-deuteration of $\text{ZrCo}_{1-x}\text{Ni}_x$ hydride/deuteride which results in single desorption plateau for all the isotherms can be written as;

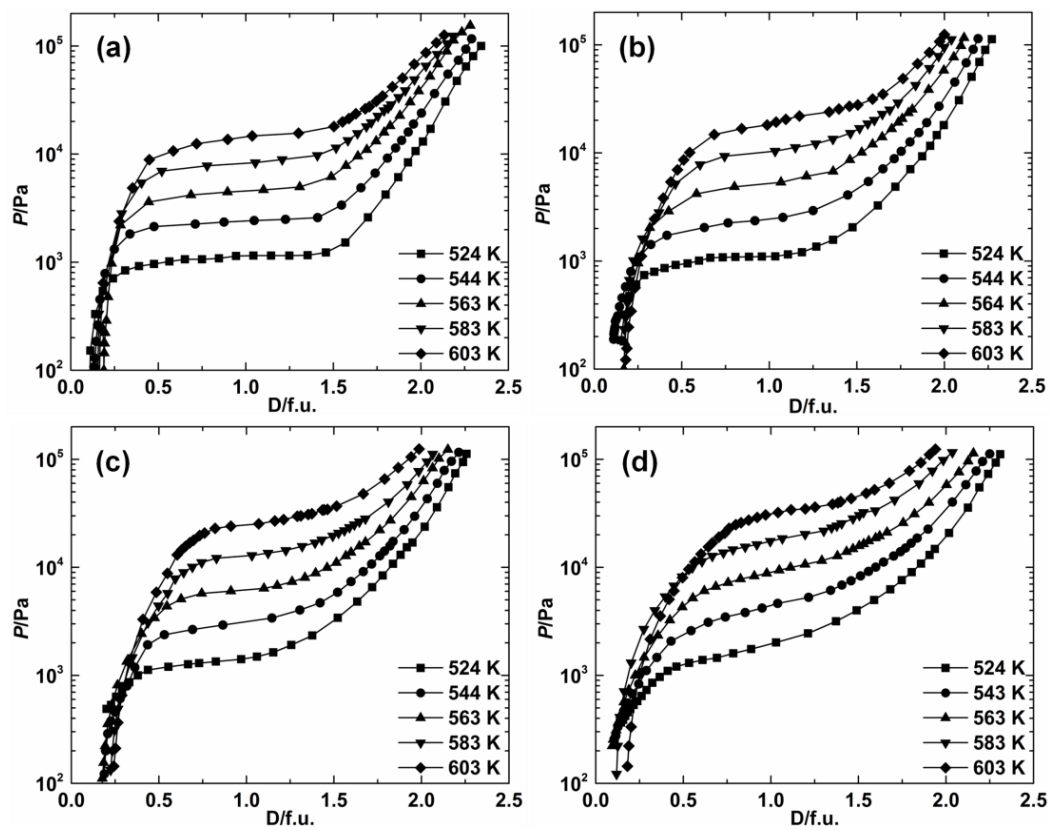
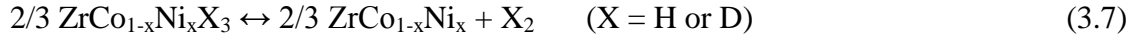


Figure 3.15: Deuterium desorption pressure-composition isotherms for $\text{ZrCo}_{1-x}\text{Ni}_x\text{-D}_2$ systems: (a) $x = 0$, (b) $x = 0.1$ (c) $x = 0.2$ and (d) $x = 0.3$

The temperature dependence of the equilibrium plateau pressure for $\text{ZrCo}_{1-x}\text{Ni}_x\text{-H}_2/\text{D}_2$ systems is best represented by the van't Hoff plot, shown in Figure 3.16. Equilibrium plateau pressure values corresponding to $\text{X/f.u.} = 1$ were taken for construction of the van't Hoff plots. A linear relation was observed for the temperature dependence of equilibrium plateau

pressure and is represented by the van't Hoff relations. The van't Hoff relations obtained for $\text{ZrCo}_{1-x}\text{Ni}_x\text{-H}_2/\text{D}_2$ systems are as follows:

$\text{ZrCo}_{1-x}\text{Ni}_x\text{-H}_2$ systems:

$$\log(P/\text{Pa}) = -4983/(T/\text{K}) + 12.5 \quad (x = 0.1) \quad (3.8)$$

$$\log(P/\text{Pa}) = -4876/(T/\text{K}) + 12.5 \quad (x = 0.2) \quad (3.9)$$

$$\log(P/\text{Pa}) = -4834/(T/\text{K}) + 12.5 \quad (x = 0.3) \quad (3.10)$$

$\text{ZrCo}_{1-x}\text{Ni}_x\text{-D}_2$ systems:

$$\log(P/\text{Pa}) = -4989/(T/\text{K}) + 12.6 \quad (x = 0.1) \quad (3.11)$$

$$\log(P/\text{Pa}) = -4930/(T/\text{K}) + 12.6 \quad (x = 0.2) \quad (3.12)$$

$$\log(P/\text{Pa}) = -4852/(T/\text{K}) + 12.6 \quad (x = 0.3) \quad (3.13)$$

From the van't Hoff plot the enthalpy and entropy change for the de-hydrogenation/deuteriation of $\text{ZrCo}_{1-x}\text{Ni}_x$ hydrides/deuterides are deduced at the average experimental temperature of 563 K and listed in Table 3.4.

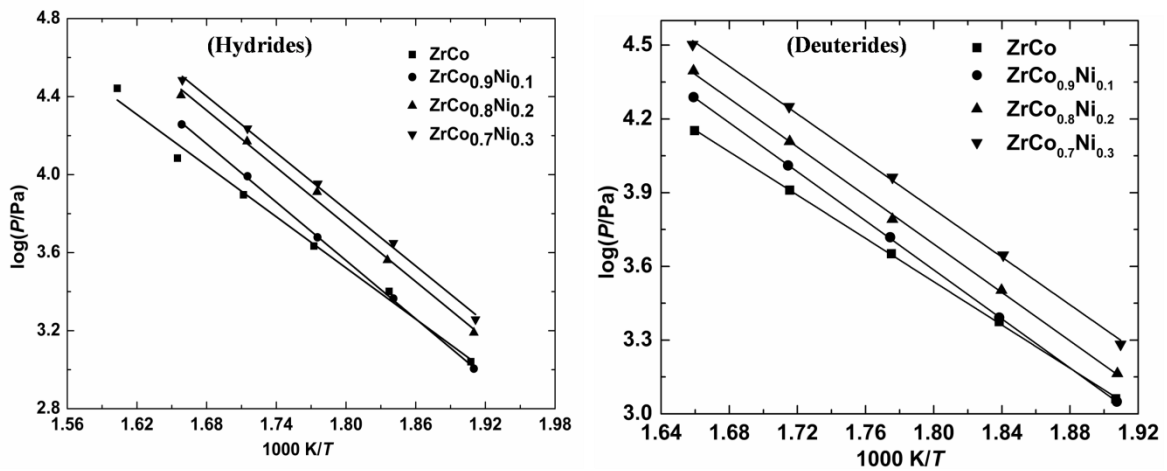


Figure 3.16: van't Hoff plots for $\text{ZrCo}_{1-x}\text{Ni}_x\text{-H}_2/\text{D}_2$ systems

Several reports are available in the literature about the PCT relations in the ZrCo-H₂/D₂ system which is summarized in Section-3.1.3. However, to the best of our knowledge there is very limited PCT data for the Ni- substituted analogues. Only the report by Irvine and Harris [66] shows the PCT relations for ZrCo-H₂ and ZrCo_{0.84}Ni_{0.16}-H₂ systems from 423 to 773 K. In their study, Irvine and Harris [66] have observed two plateau regions both for ZrCo-H₂ and ZrCo_{0.84}Ni_{0.16}-H₂ systems. However, all other literature reports [33, 41, 43, 53, 59, 60-62, 67-69, 99, 100] have proved that there is only a single plateau for the ZrCo-H₂ system. In the present study, we have observed only a single plateau for both ZrCo-H₂ and ZrCo_{1-x}Ni_x-H₂/D₂ systems.

Table 3.4: Thermodynamic functions for desorption of hydrogen/deuterium in ZrCo_{1-x}Ni_x-H₂/D₂ systems.

| System | | $\Delta_r H^\circ$ (kJ/mole H ₂) | $\Delta_r S^\circ$ (J/(mole H ₂ ·K)) | T_{des} (K) |
|---------------------------------------|-----------|---|--|----------------------|
| ZrCo | Hydride | 83.7 ± 3.9 | 122.2 ± 3.9 | 683 |
| | Deuteride | 84.3 ± 0.6 | 124.5 ± 1.1 | 677 |
| ZrCo _{0.9} Ni _{0.1} | Hydride | 95.4 ± 0.9 | 144.1 ± 0.8 | 664 |
| | Deuteride | 95.5 ± 0.4 | 145.5 ± 1.2 | 656 |
| ZrCo _{0.8} Ni _{0.2} | Hydride | 93.4 ± 3.3 | 143.9 ± 3.4 | 650 |
| | Deuteride | 94.4 ± 1.3 | 145.5 ± 1.2 | 645 |
| ZrCo _{0.7} Ni _{0.3} | Hydride | 92.6 ± 2.3 | 143.9 ± 2.5 | 644 |
| | Deuteride | 92.9 ± 1.6 | 145.5 ± 2.3 | 638 |

It is evident from the data reported in Table 3.4 that the Ni-substitution substantially changes the enthalpy and entropy of dehydrogenation reaction compared to ZrCo-H₂ system. The enthalpy change for de-hydrogenation/de-deuteration reactions of Ni substituted hydrides/deuterides is found to be higher than that of pure ZrCo hydrides/deuterides. This can be attributed to the higher enthalpy of formation of Ni hydrides than that of Co hydrides, as is evident in Table 1.4. Another important observation from Figure 3.16 is that desorption

plateau pressure increases with increasing the Ni-content in the $\text{ZrCo}_{1-x}\text{Ni}_x\text{-H}_2$ system. However, for the composition with $x = 0.1$, the desorption plateau pressure is lower than that of ZrCo-H_2 system below 543 K. Similar behavior of the crossover of van't Hoff plots is also observed in for ZrCo-D_2 and $\text{ZrCo}_{0.9}\text{Ni}_{0.1}\text{-D}_2$ systems. Purely based on general analogy, when a non-hydriding element such as Co is replaced by a hydriding element such as Ni, the stability of hydride phase is supposed to increase. However, the trend observed in this study shows that Ni-substitution is destabilizing the hydride phase due to which desorption plateau pressure increases. Lundin et al. [101] have tried to correlate the effect of interstitial hole size on the stability of hydrides of AB- and AB_5 -type intermetallic compounds. They have observed that the increase in tetrahedral hole size increases the stability of hydrides. In order to apply these correlations to explain the trend observed in the present study, it is essential to know the effect of Ni content on the interstitial hole sizes in the $\text{ZrCo}_{1-x}\text{Ni}_x$ alloys which has to be generated by further experiments or modeling.

For the practical application of these metal-hydrogen systems in ITER SDS, it is essential to know the desorption temperature (T_{des}) for release of 100 kPa of hydrogen. From the van't Hoff relations, the desorption temperature (T_{des}) for the $\text{ZrCo}_{1-x}\text{Ni}_x\text{-H}_2/\text{D}_2$ systems were calculated. The variation of T_{des} with Ni content is shown in Figure 3.17. It is evident from this figure that the T_{des} decreases with increase in Ni-content without affecting the storage capacity, which suggests that Ni-substituted ZrCo alloys are favorable for use in ITER SDS.

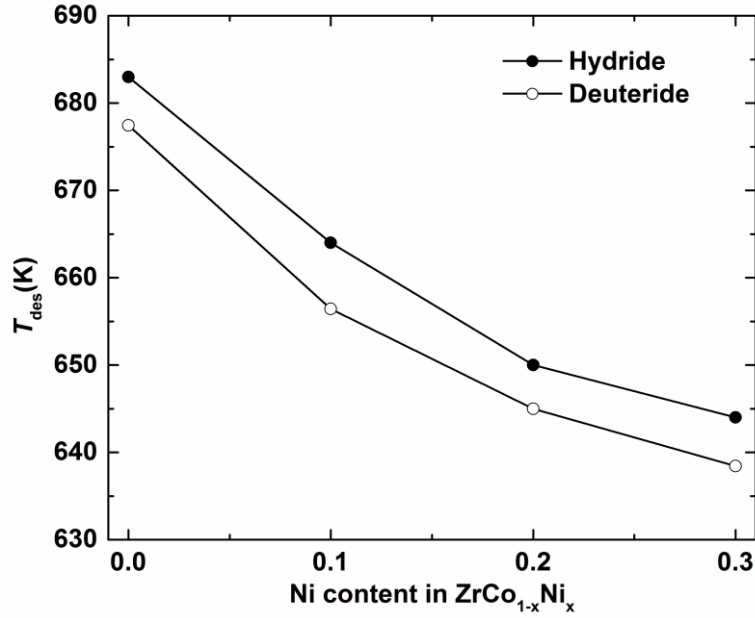


Figure 3.17: Variation of T_{des} with Ni content in $\text{ZrCo}_{1-x}\text{Ni}_x$ alloys

A comparison of thermodynamic parameters for $\text{ZrCo}_{1-x}\text{Ni}_x\text{-H}_2$ and $\text{ZrCo}_{1-x}\text{Ni}_x\text{-D}_2$, Table 3.4, reveal that the equilibrium plateau pressures for $\text{ZrCo}_{1-x}\text{Ni}_x\text{-D}_2$ systems are higher than that of $\text{ZrCo}_{1-x}\text{Ni}_x\text{-H}_2$ systems which is expected based on normal hydrogen isotope effect [40].

It can be seen from Eq. 3.6 that the hydrogen isotope effect on the equilibrium pressure of hydrogen arises from the interplay of two thermodynamic factors namely, entropy and enthalpy that control the relative stabilities of the corresponding isotopic hydrides. The interplay of two thermodynamic parameters and the net hydrogen isotope effect is discussed in detailed in Section-3.1.3. It is evident from Table 3.4 that there is no substantial isotopic effect on the enthalpy of dehydrogenation/de-deuteration for $\text{ZrCo}_{1-x}\text{Ni}_x\text{-H}_2/\text{D}_2$ systems. Hence, the difference in equilibrium plateau pressure arises due to the difference in entropy of reaction for hydrides and deuterides. Since the entropy of desorption reaction ($\Delta_r S^\circ$) for deuterides is higher than that of hydrides, a normal isotope effect is observed for all the alloys. The normal isotope effect for all $\text{ZrCo}_{1-x}\text{Ni}_x$ alloys can also be confirmed from Figure 3.17, which indicates the lower desorption temperature (T_{des}) for the deuterides than the

corresponding hydrides. Based on these observation, it is expected that the equilibrium pressure will follow the trend: $p(T_2) > p(D_2) > p(H_2)$ for all $ZrCo_{1-x}Ni_x$ alloys.

3.2.3 Hydrogen absorption-desorption cyclic life studies

The reversible storage capacity of any hydrogen storage material mainly relies on its long-term cyclic stability. Hence, the absorption-desorption cyclic life studies of $ZrCo_{1-x}Ni_x-H_2$ systems are investigated in the present study as described in the Section-2.5. Effect of hydrogen absorption-desorption cycles on the storage capacity of $ZrCo_{1-x}Ni_x$ alloys is shown in Figure 3.18.

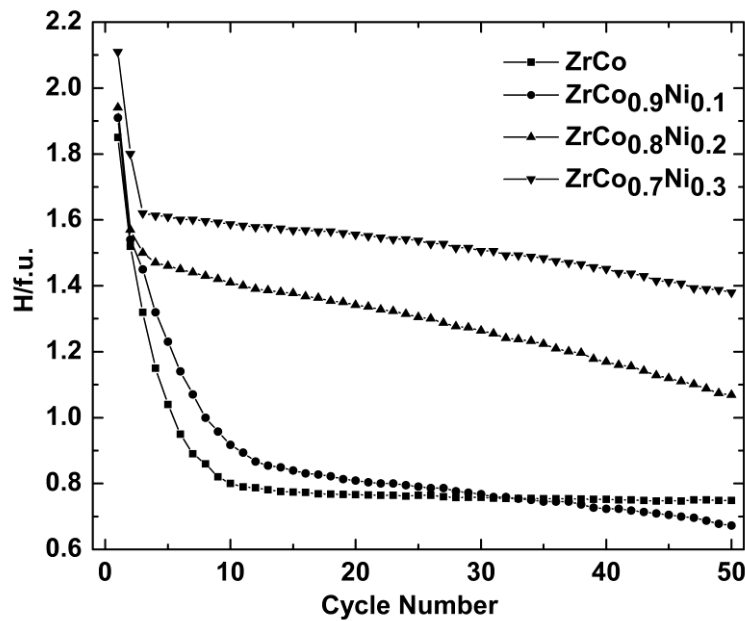


Figure 3.18: Effect of hydrogen absorption-desorption cycles on the storage capacity of $ZrCo_{1-x}Ni_x$ alloys at 583 K

It is evident from Figure 3.18 that the hydrogen absorption capacity (H/f.u.) at 583 K for $ZrCo$ and $ZrCo_{0.9}Ni_{0.1}$ alloys decrease substantially up to 10 repeated cycles after which it remains almost constant. For the alloys of compositions $ZrCo_{0.8}Ni_{0.2}$ and $ZrCo_{0.7}Ni_{0.3}$, the absorption capacity decreases slightly upto 3 repeated cycles after which there is small

gradual decrease in H/f.u. up to 50 cycles. However, the final absorption capacity after 50 repeated cycles follow the trend: $\text{ZrCo}_{0.7}\text{Ni}_{0.3} > \text{ZrCo}_{0.8}\text{Ni}_{0.2} > \text{ZrCo} > \text{ZrCo}_{0.9}\text{Ni}_{0.1}$.

The XRD patterns of the hydride phase after 50th cycles are shown in Figure 3.19. It is clearly evident from this figure that the hydrides of all the alloys form a small fraction of ZrCo_2 and ZrH_2 along with ZrCoH_3 as the major product. Hence, it can be inferred that hydrogen absorption-desorption cycles results in disproportionation according to reaction in Eq. 1.24. However, due to very small particle size after 50 cycles of absorption-desorption, the XRD pattern of the sample did not show very sharp and high intensity peaks. Therefore, it was not possible to carry out Rietveld refinement to calculate phase fractions in the samples. In absence of accurately quantifying the amount of phase fractions of ZrH_2 and ZrCo_2 the extent of disproportionation reaction could not be ascertained.

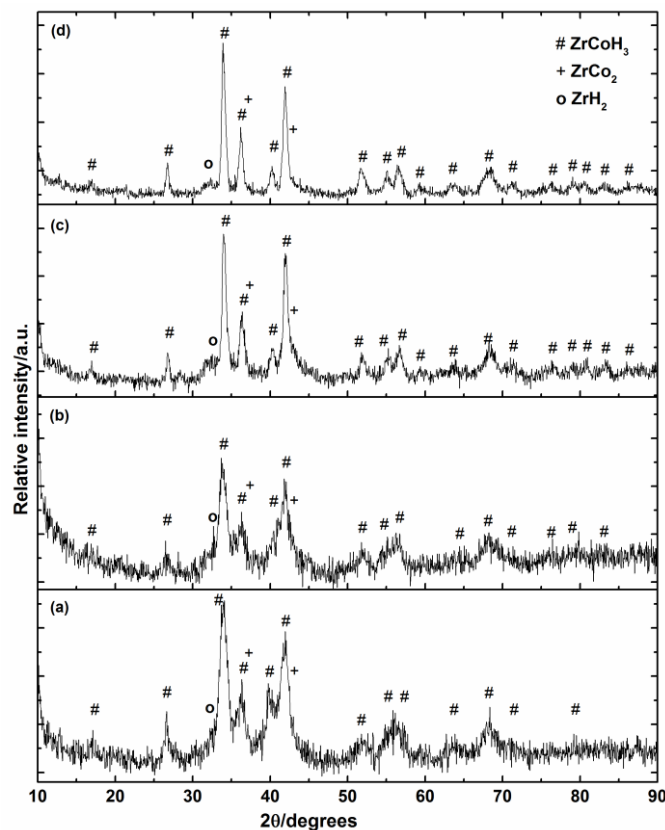


Figure 3.19: X-ray diffraction patterns of hydride phases after 50th cycles: (a) $x = 0$, (b) $x = 0.1$, (c) $x = 0.2$ and (d) $x = 0.3$

The crystallite sizes of hydrides before and after 50th cycle of hydrogen absorption-desorption are calculated by using the Scherrer formula [102] and are listed in Table 3.5. It is observed that upon cycling the crystallite size decreases significantly for compositions of $x = 0$ and 0.1, whereas the change is very small for compositions of $x = 0.2$ and 0.3. It is proposed from the above trend in crystallite size that the disproportionation kinetics is faster for compositions of $x = 0$ and 0.1 than that for $x = 0.2$ and 0.3.

Table 3.5: Effect of hydrogen absorption-desorption cycles on crystallite size of $\text{ZrCo}_{1-x}\text{Ni}_x$ hydrides.

| Compound | Crystallite size (Å) | |
|---|----------------------|------------------------------|
| | Before cycling | After 50 th cycle |
| ZrCo hydride | 135 | 69 |
| ZrCo _{0.9} Ni _{0.1} hydride | 121 | 67 |
| ZrCo _{0.8} Ni _{0.2} hydride | 136 | 112 |
| ZrCo _{0.7} Ni _{0.3} hydride | 158 | 136 |

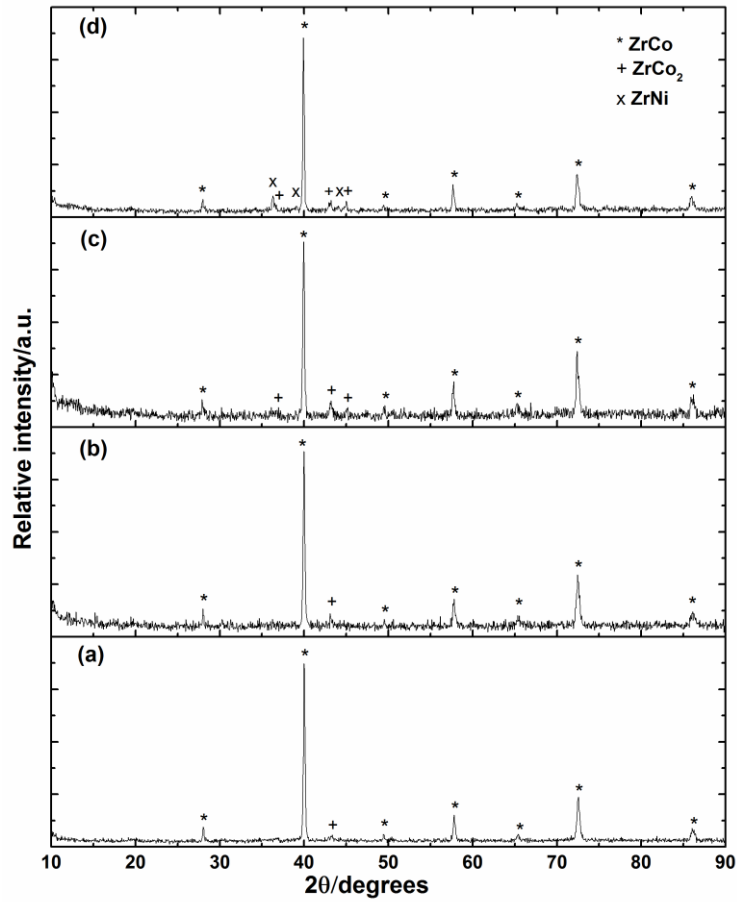


Figure 3.20: X-ray diffraction patterns of de-hydrated phases after 50th cycle: (a) $x = 0$, (b) $x = 0.1$, (c) $x = 0.2$ and (d) $x = 0.3$

Further, the XRD pattern of the de-hydrated phase after 50th cycle is shown in Figure 3.20. A comparison of Figure 3.8 with Figure 3.20 reveals that the fraction of ZrCo_2 phase appears in the cycled samples which can be attributed to hydrogen induced disproportionation upon successive hydrogen absorption-desorption cycles.

3.3 Storage behavior of $\text{ZrCo}_{0.9}\text{Fe}_{0.1}$ alloy

3.3.1 Materials Characterization

The phase diagram of Co-Fe system suggests that Fe has very limited solubility (~ 10 atom% at 773 K) in Co [91]. Therefore, in the present work it was decided to investigate the hydrogen isotope storage behavior of $\text{ZrCo}_{0.9}\text{Fe}_{0.1}$ alloy. Figure 3.21 represent the X-ray diffraction patterns of $\text{ZrCo}_{0.9}\text{Fe}_{0.1}$ alloy and its hydride/deuteride.

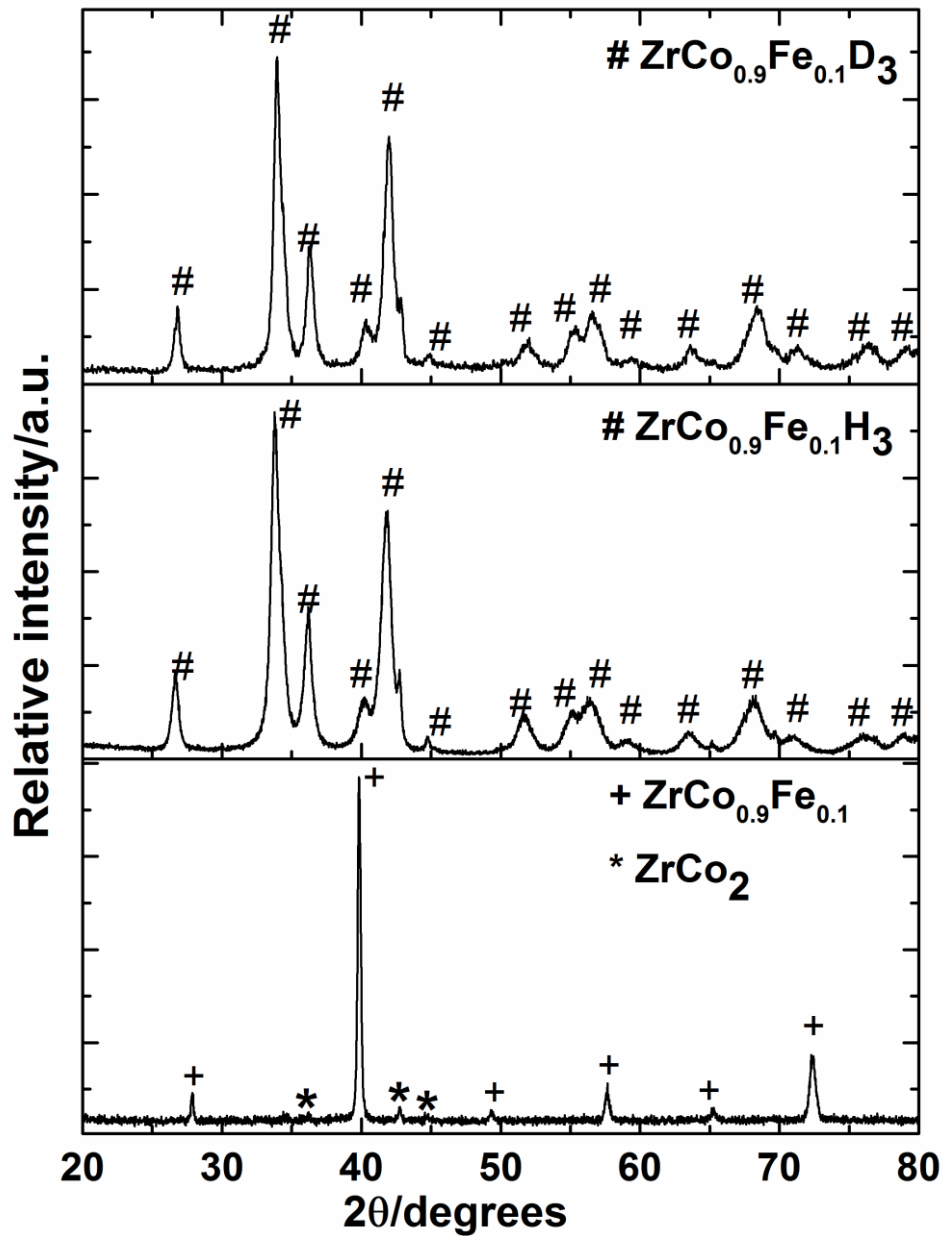


Figure 3.21: X-ray diffraction pattern of $\text{ZrCo}_{0.9}\text{Fe}_{0.1}$ alloy, its hydride and deuteride

Formation of the alloy and its hydride/deuteride were confirmed by comparing their X-ray diffraction patterns with the JCPDS (Joint Committee on Powder Diffraction Standards) files [89]. It is evident from Figure 3.21 that alike ZrCo, ZrCo_{0.9}Fe_{0.1} alloy also has a small amount of ZrCo₂ impurity phase. This figure also confirms the formation of a cubic phase ZrCo_{0.9}Fe_{0.1} alloy similar to ZrCo. The XRD patterns shown in Figure 3.21 unveil the formation of a single orthorhombic phase similar to ZrCoH₃ for both the ZrCo_{0.9}Fe_{0.1} hydride and deuteride. The lattice parameter and cell volume of the ZrCo_{0.9}Fe_{0.1} alloy were calculated by Rietveld refinement of XRD data using the FULLPROF program [79]. Rietveld refinement pattern of ZrCo_{0.9}Fe_{0.1} alloy is shown in Figure 3.22.

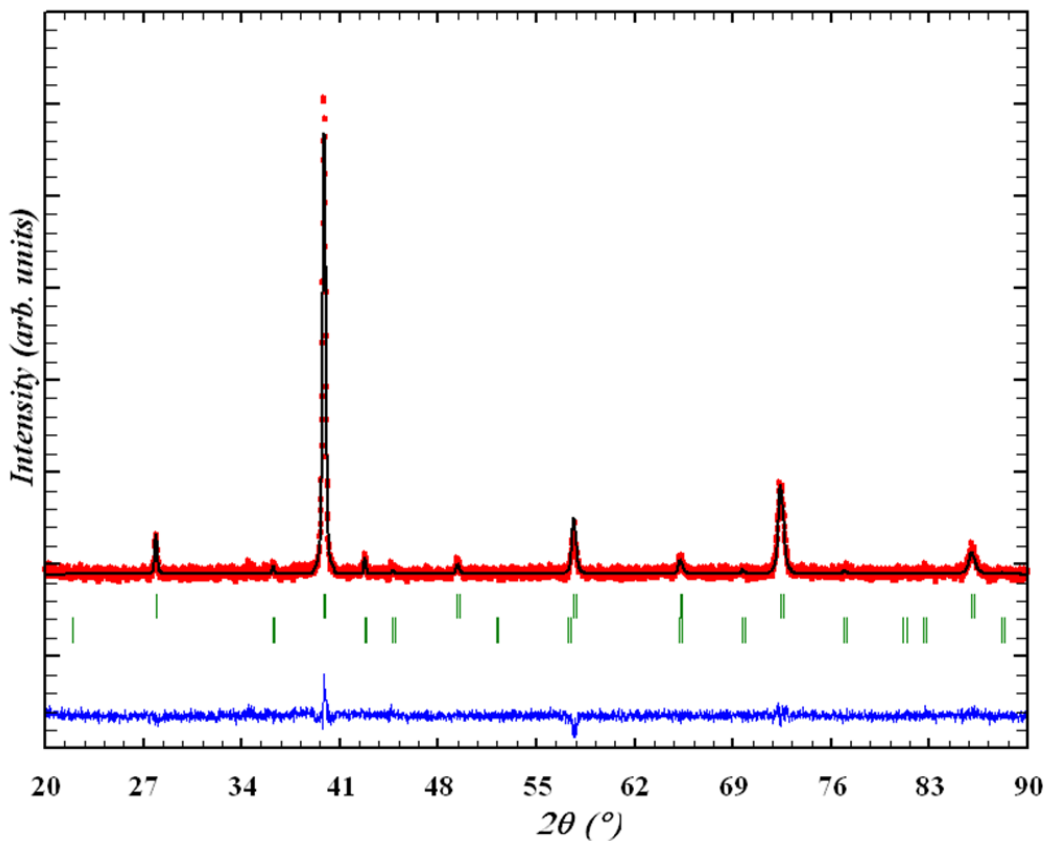


Figure 3.22: Rietveld refinement of X-ray diffraction pattern of ZrCo_{0.9}Fe_{0.1} alloy. The tick marks indicate ZrCo (top) and ZrCo₂ (bottom) phases

The refinement results are listed in Table 3.6 and compared with the corresponding parameters of ZrCo alloy. The values of lattice parameter and cell volume for ZrCo_{0.9}Fe_{0.1} alloy are found to be slightly higher than that of ZrCo alloy, which is in accordance with their atomic radii values (atomic radii of Co = 1.25 Å and Fe = 1.26 Å). However, the phase fraction of ZrCo₂ impurity phase was found to be ~4% in ZrCo_{0.9}Fe_{0.1} alloy as compared to the value of ~1% for the ZrCo alloy.

Table 3.6: Lattice parameters and unit cell volume of ZrCo and ZrCo_{0.9}Fe_{0.1} alloys.

| Alloy | Lattice parameters | Unit cell volume of | Phase | Ref. | |
|---------------------------------------|--------------------|---------------------|----------------------|------------------|-------------------|
| | of | major | constituent | abundances/ vol% | |
| | constituent | phase | phase (ZrCo Phase) / | ZrCo | ZrCo ₂ |
| | (ZrCo Phase) / Å | Å ³ | phase | phase | phase |
| ZrCo | 3.1957 (1) | 32.637 (2) | 99 | 1 | This study |
| ZrCo _{0.9} Fe _{0.1} | 3.1959 (2) | 32.642 (4) | 96 | 4 | This study |

The SEM images of ZrCo_{0.9}Fe_{0.1} alloy and its hydride are shown in Figure 3.23. This reveals a cleavage type surface for ZrCo_{0.9}Fe_{0.1} alloy and a cleavage type fracture surface for the hydride phase. The presence of cracks in SEM image of hydride phase can be attributed to the expansion of lattice of ZrCo_{0.9}Fe_{0.1} alloy upon hydrogenation. The EDX spectra of ZrCo_{0.9}Fe_{0.1} alloy is shown in Figure 3.24. The microanalysis carried out at different morphological positions of the alloy was used to find out the average composition of the alloy which is in accordance with the nominal composition. The homogeneity of the alloy was confirmed by elemental mapping. The elemental mapping images of ZrCo_{0.9}Fe_{0.1} alloy are shown in Figure 3.25 which reveals the homogeneous nature of the alloy.

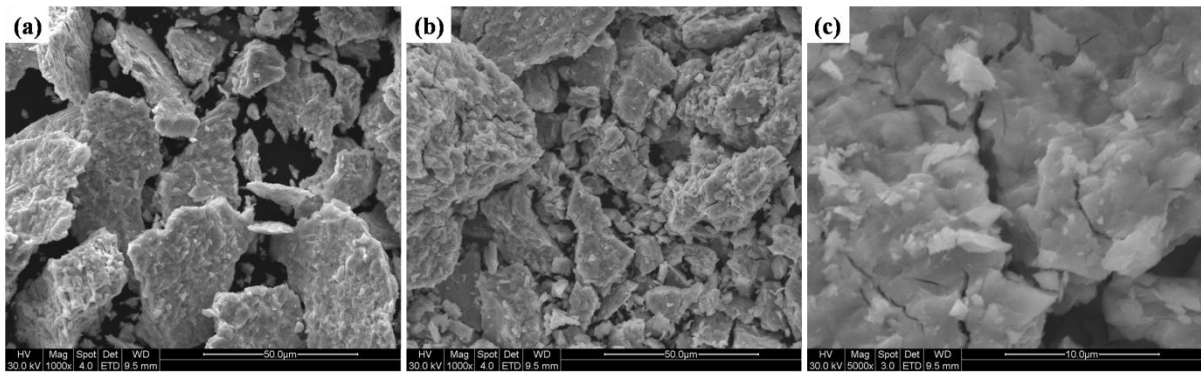


Figure 3.23: SEM images of (a) $\text{ZrCo}_{0.9}\text{Fe}_{0.1}$ alloy at magnifications of 1000x, (b) & (c) hydride of $\text{ZrCo}_{0.9}\text{Fe}_{0.1}$ at magnifications of 1000x and 5000x, respectively

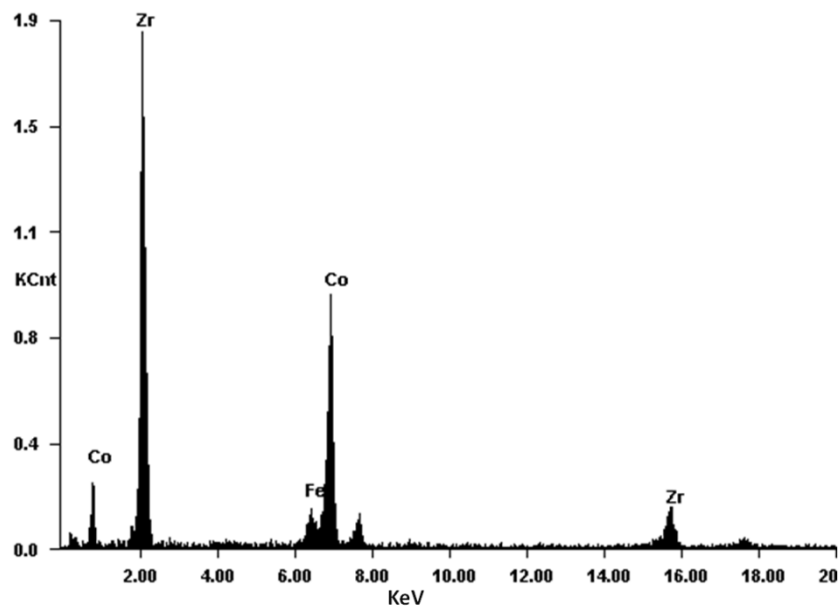


Figure 3.24: EDS spectra of $\text{ZrCo}_{0.9}\text{Fe}_{0.1}$ alloy

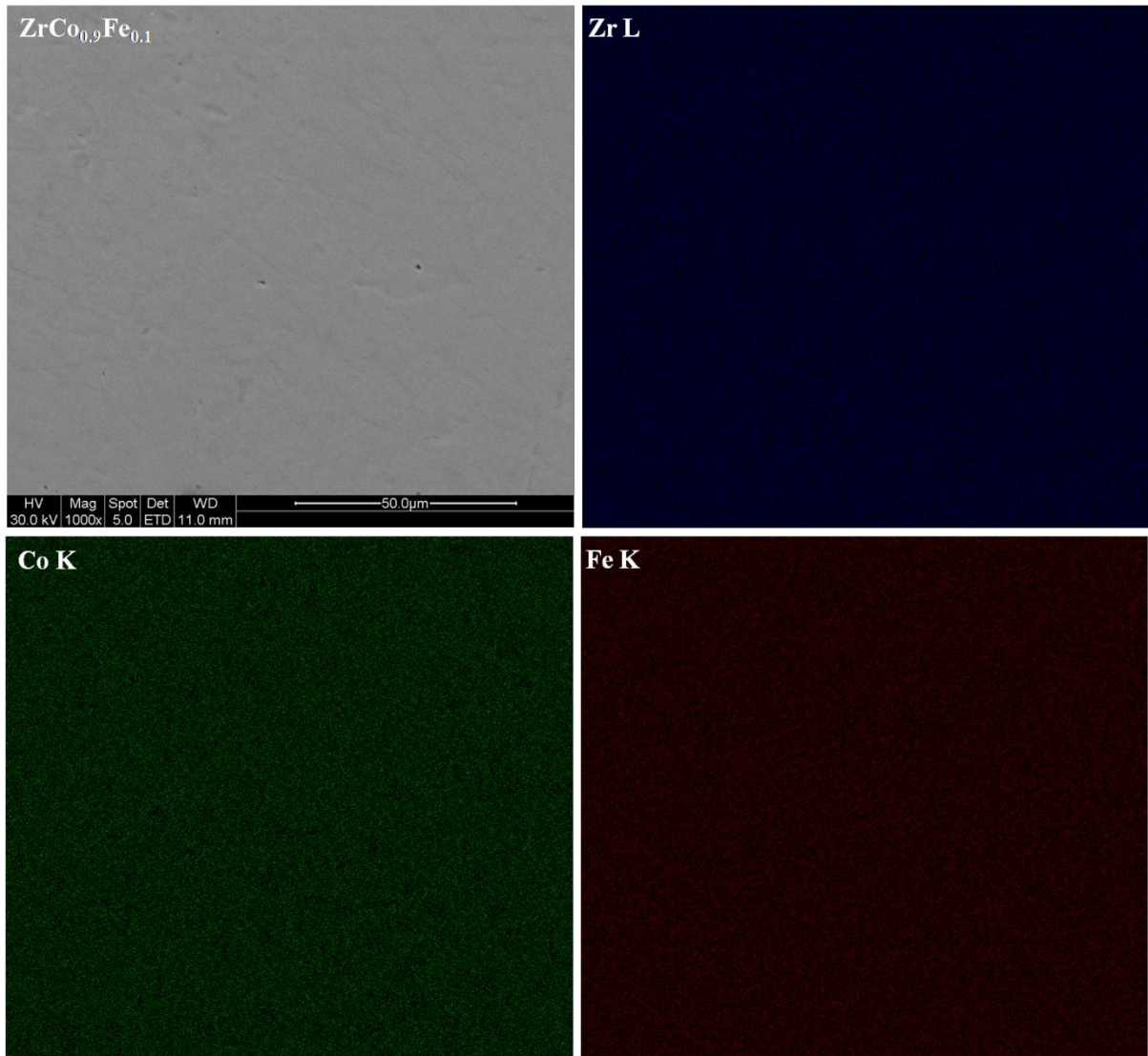


Figure 3.25: Elemental mapping images of $\text{ZrCo}_{0.9}\text{Fe}_{0.1}$ alloy

3.3.2 Pressure-Composition-Temperature measurements on $\text{ZrCo}_{0.9}\text{Fe}_{0.1}\text{-H}_2/\text{D}_2$ systems

The hydrogen/deuterium desorption pressure-composition isotherms for $\text{ZrCo}_{0.9}\text{Fe}_{0.1}\text{-H}_2/\text{D}_2$ systems are shown in Figure 3.26. The reactions involved in the pressure-composition isotherms for hydride and deuterides can be written as:



It is evident from all the isotherms shown in Figure 3.26 that in the temperature range of investigation, both the hydride and deuteride show a single desorption plateau and the plateau width is found to decrease with increase in temperature. A van't Hoff plot was constructed using the plateau pressure data and the thermodynamic parameters were calculated using the van't Hoff equation for hydrogen/deuterium desorption reaction. The van't Hoff relations obtained for $\text{ZrCo}_{0.9}\text{Fe}_{0.1}\text{-H}_2/\text{D}_2$ systems are as follows;

$\text{ZrCo}_{0.9}\text{Fe}_{0.1}\text{-H}_2$ system

$$\log(P/\text{Pa}) = -3613/(T/\text{K}) + 10.0 \quad (3.16)$$

$\text{ZrCo}_{0.9}\text{Fe}_{0.1}\text{-D}_2$ system

$$\log(P/\text{Pa}) = -3633/(T/\text{K}) + 10.1 \quad (3.17)$$

The van't Hoff plot for $\text{ZrCo}_{0.9}\text{Fe}_{0.1}\text{-H}_2/\text{D}_2$ systems are shown in Figure 3.27. Using these van't Hoff relations the enthalpy ($\Delta_r H^\circ$) and entropy ($\Delta_r S^\circ$) change for the /de-hydrogenation/de-deuteration of $\text{ZrCo}_{0.9}\text{Fe}_{0.1}$ hydride/deuteride were deduced at the average experimental temperature of 553 K and listed in Table 3.7.

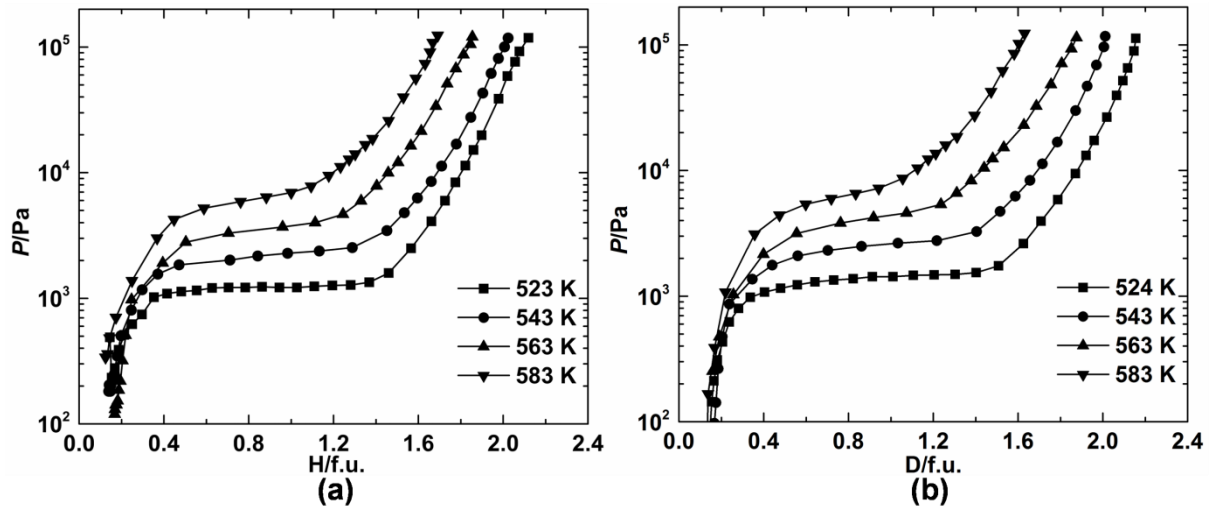


Figure 3.26: Hydrogen/deuterium desorption pressure-composition isotherms for (a) $\text{ZrCo}_{0.9}\text{Fe}_{0.1}\text{-H}_2$ and (b) $\text{ZrCo}_{0.9}\text{Fe}_{0.1}\text{-D}_2$ systems

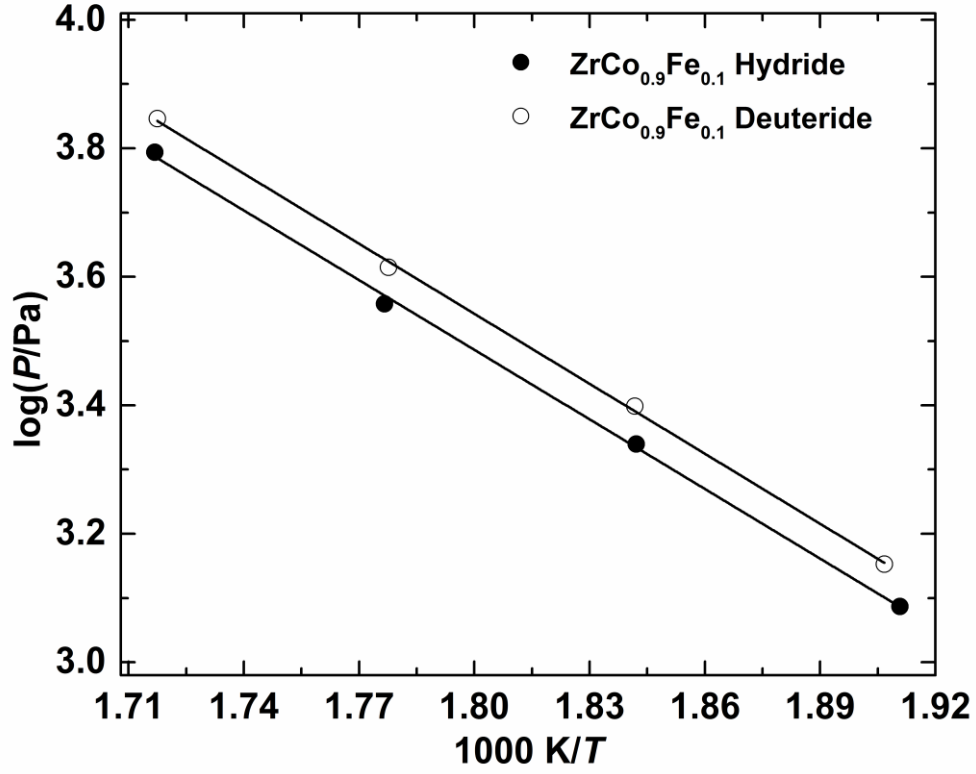


Figure 3.27: van't Hoff plots for $\text{ZrCo}_{0.9}\text{Fe}_{0.1}\text{-H}_2/\text{D}_2$ systems

Table 3.7: Thermodynamic functions for desorption of hydrogen/deuterium in $\text{ZrCo-H}_2/\text{D}_2$ and $\text{ZrCo}_{0.9}\text{Fe}_{0.1}\text{-H}_2/\text{D}_2$ systems.

| System | $\Delta_r H$ (kJ/mole H_2) | $\Delta_r S$ (J/(mole $\text{H}_2 \cdot \text{K}$)) | T_{des} (K) | Ref. |
|---|---|---|-------------------------|------------|
| ZrCo-H_2 | 83.7 ± 3.9 | 122.2 ± 3.9 | 683 | This study |
| ZrCo-D_2 | 84.3 ± 0.6 | 124.5 ± 1.1 | 677 | This study |
| $\text{ZrCo}_{0.9}\text{Fe}_{0.1}\text{-H}_2$ | 69.2 ± 1.5 | 95.7 ± 1.0 | 723 | This study |
| $\text{ZrCo}_{0.9}\text{Fe}_{0.1}\text{-D}_2$ | 69.6 ± 1.2 | 97.7 ± 1.0 | 712 | This study |

In addition, a comparison of the thermodynamic parameters for $\text{ZrCo}_{0.9}\text{Fe}_{0.1}\text{-H}_2/\text{D}_2$ and $\text{ZrCo-H}_2/\text{D}_2$ systems are made in Table 3.7. This comparison reveals that the values of enthalpy and entropy of dehydrogenation reaction for $\text{ZrCo}_{0.9}\text{Fe}_{0.1}\text{-H}_2$ system differs significantly from the values for $\text{ZrCo-H}_2/\text{D}_2$ systems. The enthalpy change for de-hydrogenation/de-deuteration reactions of Fe substituted hydrides/deuterides is found to be lower than that of pure ZrCo hydrides/deuterides. This can be attributed to the lower enthalpy of formation of Fe hydride than that of Co hydride, as is evident in Table 1.4. It is evident from Table 3.7 that the values of entropy changes for the $\text{ZrCo}_{0.9}\text{Fe}_{0.1}\text{-H}_2/\text{D}_2$ systems are $\sim 95 \text{ J}/(\text{mole H}_2\cdot\text{K})$ which is substantially lower than the values observed for $\text{ZrCo-H}_2/\text{D}_2$ systems discussed in section-3.1.3. For most of the simple binary metal hydride systems, the average value of entropy change is nearly equal to $130 \text{ J}/(\text{mole H}_2\cdot\text{K})$ which corresponds to the loss of hydrogen entropy from gas to solid phase. However, to our knowledge, this is not a universal rule and for many hydrides, this value substantially vary from the ideal value of $130 \text{ J}/(\text{mole H}_2\cdot\text{K})$. In particular, a survey of literature on Fe-substituted alloys [103, 104] shows that the entropy change is very low reaching around $\sim 61 \text{ J}/(\text{mole H}_2\cdot\text{K})$ [104] for the iron containing compounds. The results of present study also corroborate with earlier observations for iron bearing compounds. However, there is no sound explanation reported for this discrepancy in Fe-substituted alloys.

It can be seen from Eq. 3.6 that the hydrogen isotope effect on the equilibrium pressure of hydrogen/deuterium depends on the values of enthalpy and entropy change for a particular reaction involved [40]. Thereby, the interplay of these two thermodynamic factors controls the relative stability of the corresponding isotopic hydrides. It can be seen from Table 3.7 that the values of enthalpy of de-hydrogenation and de-deuteration for $\text{ZrCo}_{0.9}\text{Fe}_{0.1}\text{-H}_2/\text{D}_2$ systems do not differ much. Therefore, the nature of isotope effect for $\text{ZrCo}_{0.9}\text{Fe}_{0.1}$ alloy will arise due to the difference in entropy of reactions shown in Eqs. 3.14 and 3.15. The van't Hoff plots

presented in Figure 3.27 clearly show that the equilibrium plateau pressure of $\text{ZrCo}_{0.9}\text{Fe}_{0.1}\text{-D}_2$ system is higher than that of $\text{ZrCo}_{0.9}\text{Fe}_{0.1}\text{-H}_2$ system. This order of equilibrium plateau pressures for H_2 and D_2 confirm the normal hydrogen isotope effect for $\text{ZrCo}_{0.9}\text{Fe}_{0.1}$ alloy. Based on the nature of isotope effect, it is expected that the trend in equilibrium pressure will be $p(\text{T}_2) > p(\text{D}_2) > p(\text{H}_2)$ for $\text{ZrCo}_{0.9}\text{Fe}_{0.1}$ alloy.

3.3.3 Hydrogen absorption-desorption cyclic life studies

Figure 3.28 shows the effect of absorption-desorption cycles on the storage capacity of $\text{ZrCo}_{0.9}\text{Fe}_{0.1}$ alloy at 583 K. For better understanding, the cyclic life studies on $\text{ZrCo}_{0.9}\text{Fe}_{0.1}$ alloy is also compared with those of ZrCo alloy in Figure 3.28. This reveals that the hydrogen absorption capacity (H/f.u.) of ZrCo alloy at 583 K decreases remarkably in first 10 cycles and then it remains almost constant. However, for $\text{ZrCo}_{0.9}\text{Fe}_{0.1}$ alloy the hydrogen absorption capacity (H/f.u.) at 583 K decreases significantly up to 5th absorption-desorption cycle after which it remains almost constant. In order to interpret the effect of cyclic life, a comparison of the storage capacity before and after 50 cycles is summarized in Table 3.8. It is evident from Table 3.8 that percent decrease in the hydrogen storage capacity after 50 cycles is almost double for ZrCo-H_2 system compared to the $\text{ZrCo}_{0.9}\text{Fe}_{0.1}\text{-H}_2$ system. It is also observed from Figure 3.28 and Table 3.8 that after 50 repeated cycles the final absorption capacity of $\text{ZrCo}_{0.9}\text{Fe}_{0.1}$ alloy is higher than that of ZrCo alloy.

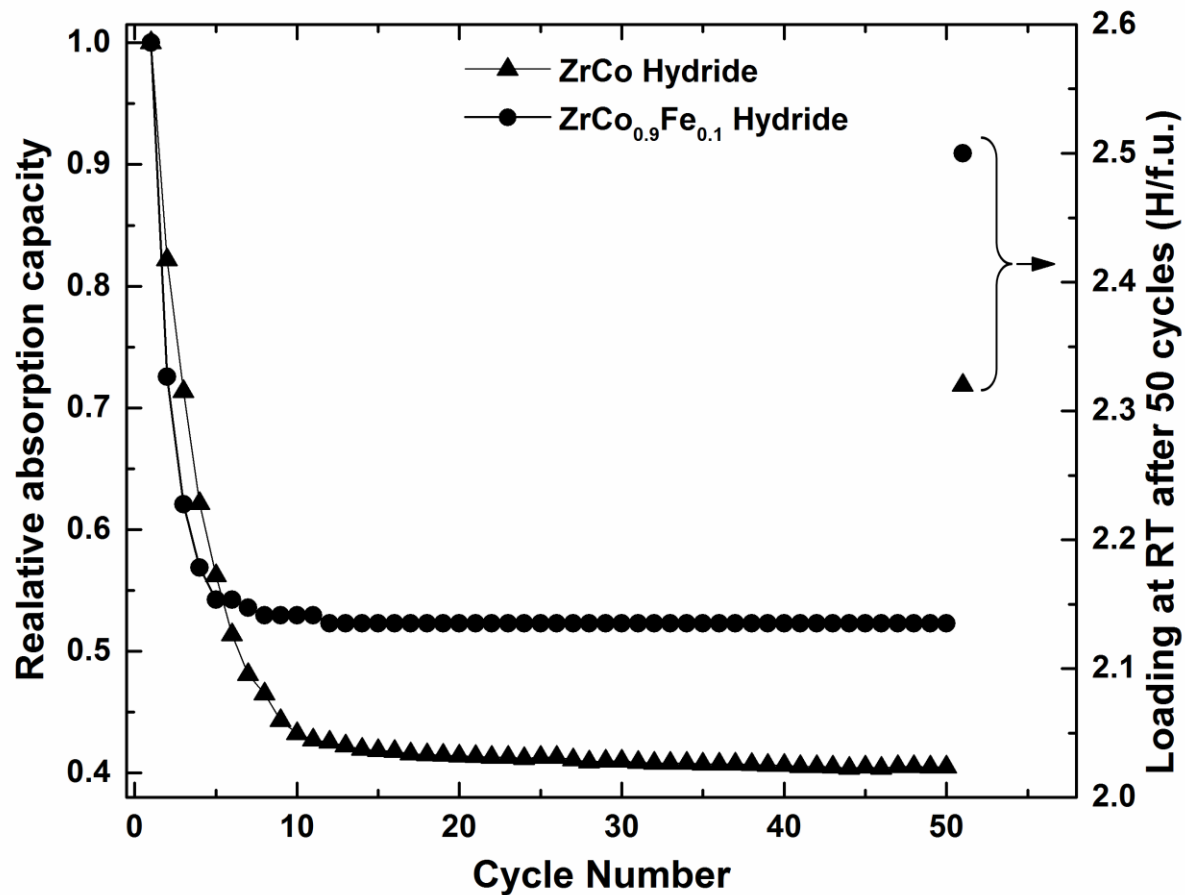


Figure 3.28: Effect of hydrogen absorption-desorption cycles on the storage capacity of $\text{ZrCo}_{0.9}\text{Fe}_{0.1}$ and ZrCo alloys at 583 K

Table 3.8: Effect of hydrogen absorption-desorption cycles on storage capacity of ZrCo and $\text{ZrCo}_{0.9}\text{Fe}_{0.1}$ alloys.

| System | Storage capacity at 0.1 MPa and 298 K | | Decrease in storage capacity upon cycling (%) |
|---|---------------------------------------|------------------------------|---|
| | (H/f.u.) | | |
| | Before cycling | After 50 th cycle | |
| ZrCo-H ₂ | 2.87 | 2.32 | 19.2 |
| ZrCo _{0.9} Fe _{0.1} -H ₂ | 2.77 | 2.50 | 8.5 |

The XRD patterns of the hydride/deuteride phase after 50th cycle are shown in Figure 3.29. It is clearly evident from this figure that upon repeated hydriding/dehydriding cycles the major product ZrCoH_3 is accompanied by formation of a small fraction of ZrCo_2 and ZrH_2 phases. Hence, it can be deduced that repeated hydrogen absorption-desorption cycles result in hydrogen induced disproportionation according to reaction in Eq. 1.24.

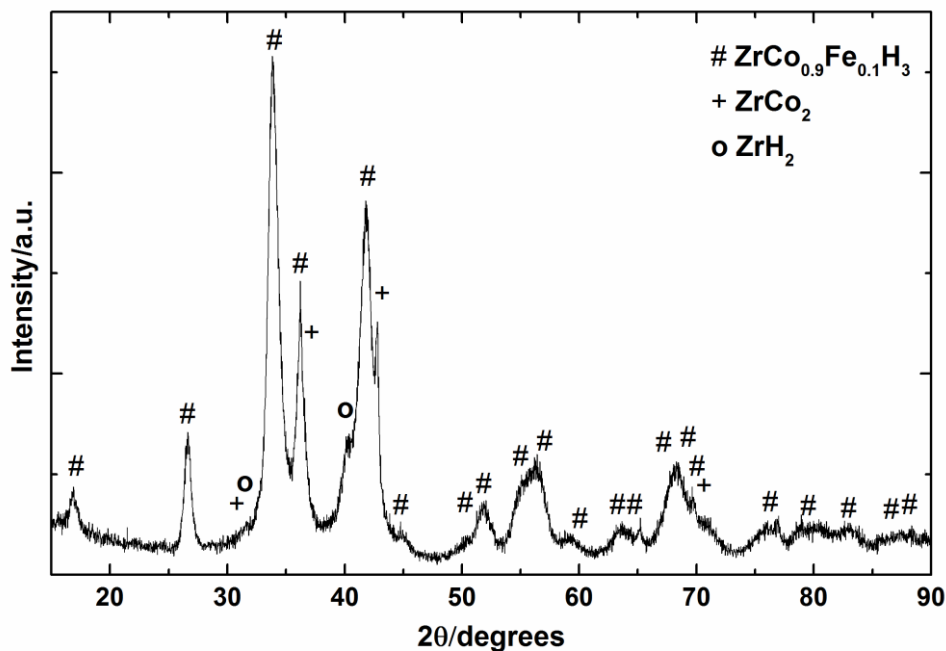


Figure 3.29: X-ray diffraction patterns of $\text{ZrCo}_{0.9}\text{Fe}_{0.1}$ hydride phase after 50th cycle

Table 3.9: Effect of hydrogen absorption-desorption cycles on crystallite sizes of ZrCo and $\text{ZrCo}_{0.9}\text{Fe}_{0.1}$ hydrides.

| Compound | Crystallite size (Å) | | Decrease in crystallite size upon cycling (%) |
|--|----------------------|------------------------------|---|
| | Before cycling | After 50 th cycle | |
| ZrCo hydride | 135 | 69 | 49 |
| $\text{ZrCo}_{0.9}\text{Fe}_{0.1}$ hydride | 79 | 59 | 25 |

A comparison of XRD patterns shown in Figure 3.21 and Figure 3.29 reveals that the full width at half maximum (FWHM) of the X-ray diffraction peaks of $\text{ZrCo}_{0.9}\text{Fe}_{0.1}$ hydride is

found to increase upon cycling. The Scherrer formula [102] was used to calculate the crystallite sizes of $\text{ZrCo}_{0.9}\text{Fe}_{0.1}$ hydride before cycling and after 50th hydrogen absorption-desorption cycle and obtained values were listed in Table 3.9. The crystallite size data for ZrCo-H_2 system was also incorporated in the Table 3.9 for better comparison. It is clearly apparent from Table 3.9 that upon absorption-desorption cycling the crystallite size decreases significantly for ZrCo alloy as compared to $\text{ZrCo}_{0.9}\text{Fe}_{0.1}$ alloy. This trend in crystallite sizes can be attributed to the faster kinetics of disproportionation for ZrCo alloy than that of $\text{ZrCo}_{0.9}\text{Fe}_{0.1}$ alloy. Hence, it can be inferred from the cyclic life studies that the $\text{ZrCo}_{0.9}\text{Fe}_{0.1}$ alloy has higher durability against hydrogen induced disproportionation than that of pure ZrCo alloy.

3.4 Storage behavior of $\text{Zr}_{1-x}\text{Ti}_x\text{Co}$ alloys

3.4.1 Materials Characterization

The X-ray diffraction patterns of $\text{Zr}_{1-x}\text{Ti}_x\text{Co}$ alloys are shown in Figure 3.30. Phase identification of alloys are confirmed by comparing their XRD patterns with the JCPDS (Joint Committee on Powder Diffraction Standards) files [89].

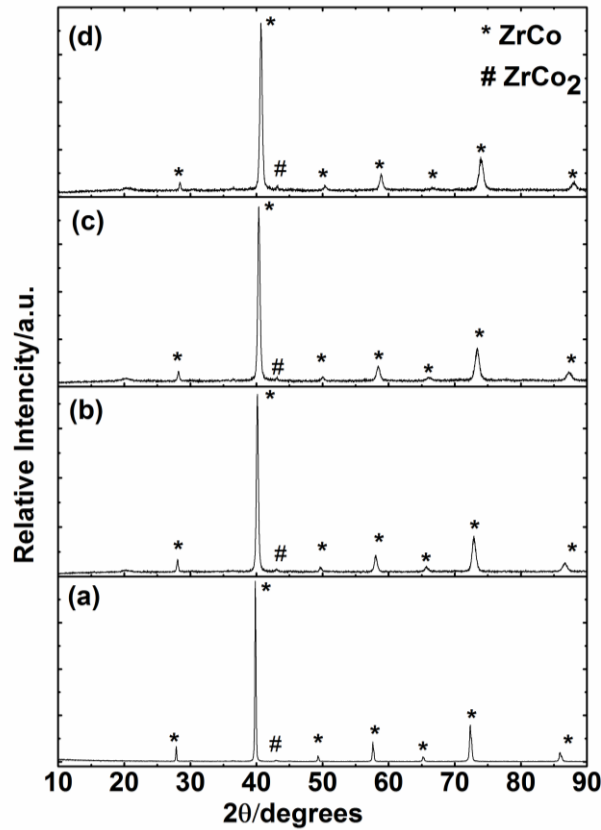


Figure 3.30: X-ray diffraction patterns of $\text{Zr}_{1-x}\text{Ti}_x\text{Co}$ alloys: (a) $x = 0$, (b) $x = 0.1$, (c) $x = 0.2$ and (d) $x = 0.3$

It is evident from X-ray diffraction patterns of $\text{Zr}_{1-x}\text{Ti}_x\text{Co}$ alloys, Figure 3.30, that trace amount of ZrCo_2 phase is present in all the alloys. Figure 3.30 also confirms the formation of b.c.c. (CsCl-type) cubic phase similar to ZrCo for all $\text{Zr}_{1-x}\text{Ti}_x\text{Co}$ alloys.

The lattice parameters and phase abundances of the alloys were calculated by Rietveld refinement of XRD data using the FULLPROF program [79]. A representative Rietveld refinement pattern for $\text{Zr}_{0.8}\text{Ti}_{0.2}\text{Co}$ alloy is shown in Figure 3.31. The refinement results for

all the $\text{Zr}_{1-x}\text{Ti}_x\text{Co}$ alloys are listed in Table 3.10. It is evident from Table 3.10 that lattice parameter and unit cell volume of the b.c.c. $\text{Zr}_{1-x}\text{Ti}_x\text{Co}$ alloys was found to decrease with increase in Ti content. Similar behavior of lattice contraction was also observed by Zhuo et al. [68] and Zhao et al. [71]. The contraction of lattice with increase in Ti content can be explained based on the simple atomic size consideration of Ti and Zr atoms.

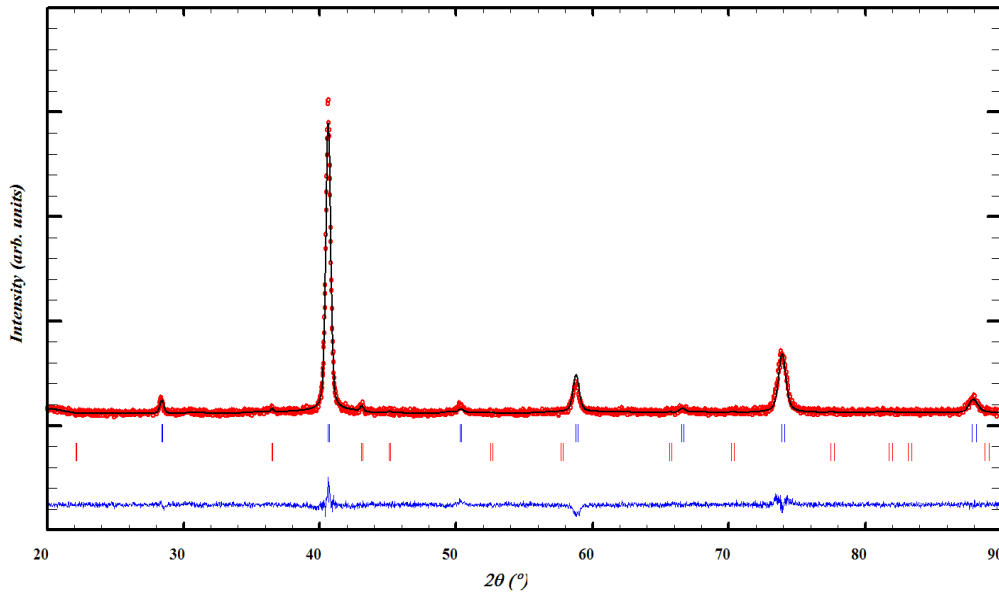


Figure 3.31: Rietveld refinement of X-ray diffraction pattern of $\text{Zr}_{0.8}\text{Ti}_{0.2}\text{Co}$ alloy. The tick marks indicate ZrCo (top) and ZrCo_2 (bottom) phases

Table 3.10: Rietveld refinement results of X-ray diffraction patterns of $\text{Zr}_{1-x}\text{Ti}_x\text{Co}$ alloys.

| Alloy | Lattice parameters of major constituent phase (ZrCo Phase)/ Å | Cell volume of major constituent phase (ZrCo Phase)/ Å ³ | Phase abundances/ vol% | |
|---|---|---|------------------------|-----------------------|
| | | | ZrCo phase | ZrCo_2 phase |
| ZrCo | 3.1957 ± 0.0001 | 32.637 ± 0.002 | 99 | 1 |
| $\text{Zr}_{0.9}\text{Ti}_{0.1}\text{Co}$ | 3.1788 ± 0.0001 | 32.120 ± 0.002 | 98 | 2 |
| $\text{Zr}_{0.8}\text{Ti}_{0.2}\text{Co}$ | 3.1591 ± 0.0001 | 31.528 ± 0.002 | 99 | 1 |
| $\text{Zr}_{0.7}\text{Ti}_{0.3}\text{Co}$ | 3.1404 ± 0.0001 | 30.972 ± 0.002 | 98 | 2 |

The XRD patterns of the hydride/deuteride phases are shown in Figure 3.32 & Figure 3.33. Comparison of XRD patterns with those reported in JCPDS (Joint Committee on Powder Diffraction Standards) files [89] reveal that, all the $\text{Zr}_{1-x}\text{Ti}_x\text{Co}$ hydrides/deuterides forms a single orthorhombic phase similar to ZrCoH_3 .

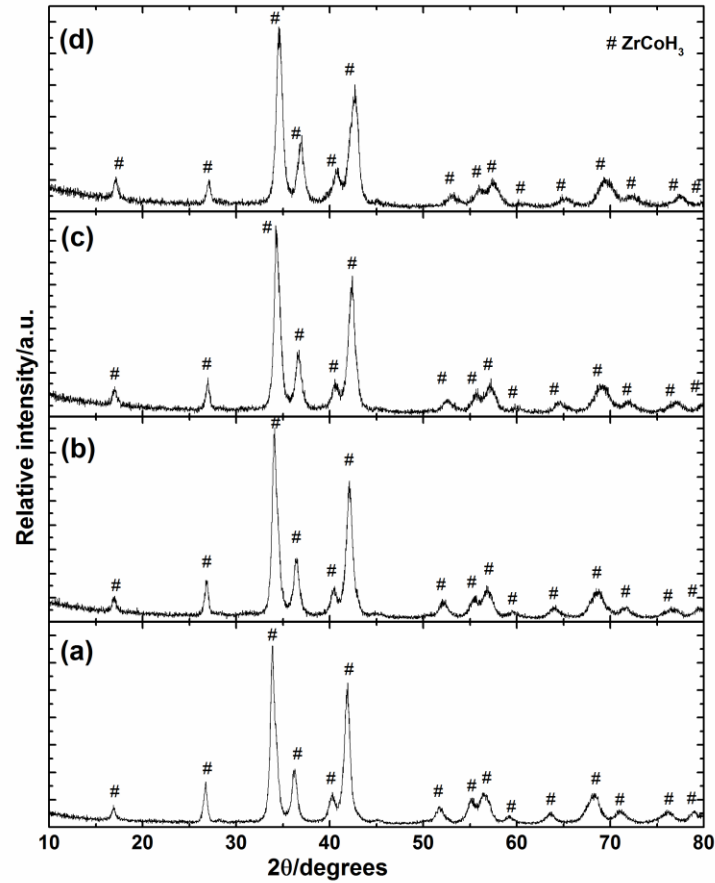


Figure 3.32: X-ray diffraction patterns of hydrides of $\text{Zr}_{1-x}\text{Ti}_x\text{Co}$ alloys: (a) $x = 0$, (b) $x = 0.1$, (c) $x = 0.2$ and (d) $x = 0.3$

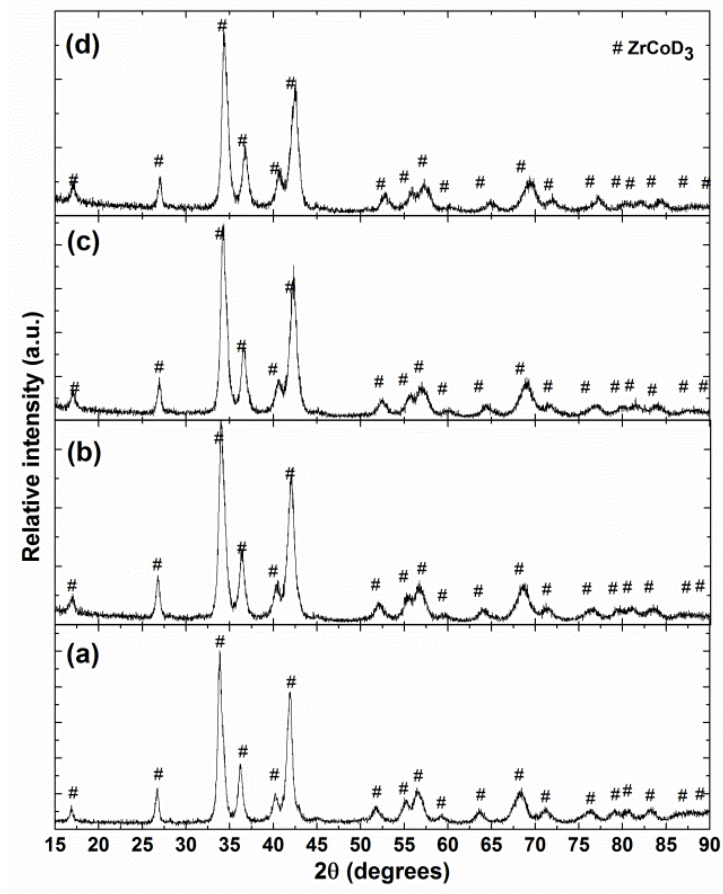


Figure 3.33: X-ray diffraction patterns of deuterides of $Zr_{1-x}Ti_xCo$ alloys: (a) $x = 0$, (b) $x = 0.1$, (c) $x = 0.2$ and (d) $x = 0.3$

All $Zr_{1-x}Ti_xCo$ alloys and their hydrides were characterized by SEM and the representative SEM images of $Zr_{0.9}Ti_{0.1}Co$ alloy and its hydride are shown in Figure 3.34. This figure confirms that all $Zr_{1-x}Ti_xCo$ alloys exhibit a cleavage type surface, whereas their hydride phases show a cleavage type fracture surface. The cracks generated in the hydride phase are attributed to the lattice expansion of ZrCo alloy upon hydrogenation.

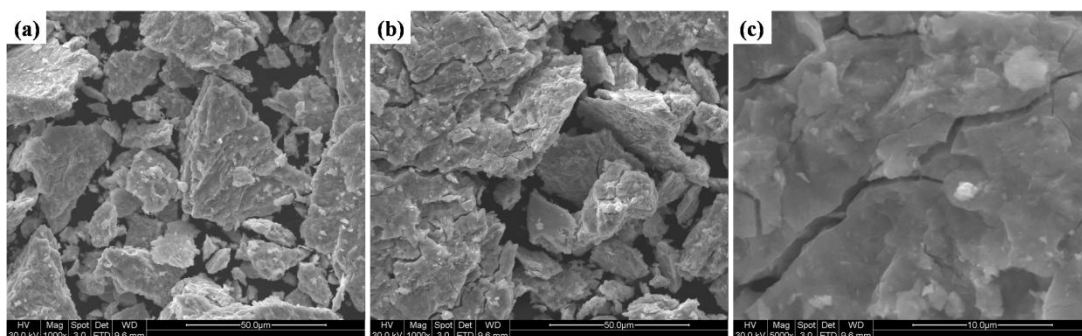


Figure 3.34: SEM images of (a) $Zr_{1-x}Ti_xCo$ alloy at magnifications of 1000x, (b) & (c) hydride of $Zr_{1-x}Ti_xCo$ at magnifications of 1000x and 5000x, respectively.

The EDX spectra of $Zr_{0.9}Ti_{0.1}Co$ alloy is shown in Figure 3.35. The EDAX microanalysis carried out at different morphological positions of the alloy reveals an average composition over the entire sample which is in accordance with the nominal composition of the alloys. The homogeneity of the alloys is confirmed by elemental mapping. The elemental mapping images of $Zr_{0.9}Ti_{0.1}Co$ alloy are shown in Figure 3.36. It is evident from Figure 3.36 that a uniform distribution of all three elements Zr, Ti and Co is observed, which reveals the homogeneous nature of the alloy. Similar pattern of uniform distribution of constituent elements is observed for all $Zr_{1-x}Ti_xCo$ alloys.

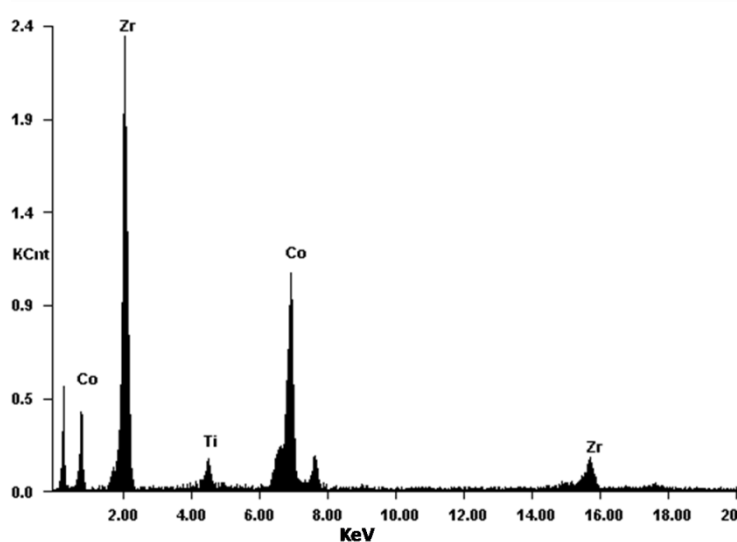


Figure 3.35: EDX spectra of $Zr_{0.9}Ti_{0.1}Co$ alloy

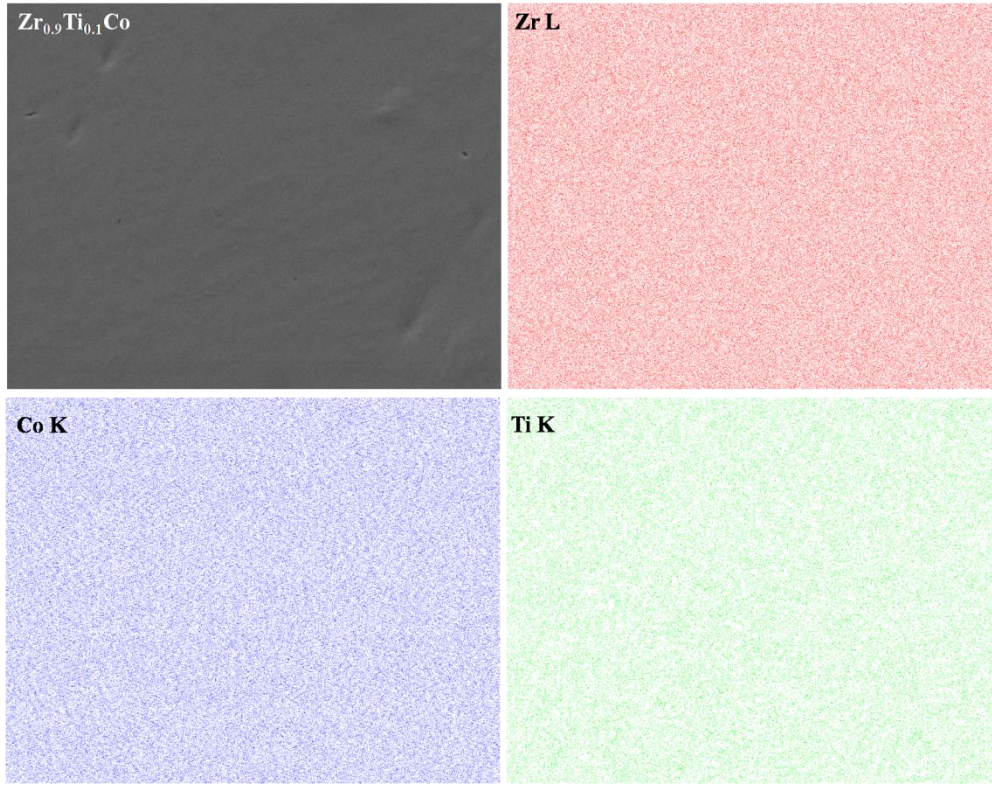
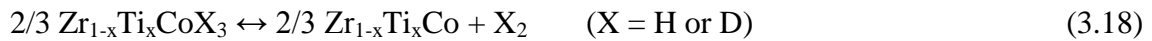


Figure 3.36: Elemental mapping images of $\text{Zr}_{0.9}\text{Ti}_{0.1}\text{Co}$ alloy.

3.4.2 Pressure-Composition-Temperature measurements on $\text{Zr}_{1-x}\text{Ti}_x\text{Co-H}_2/\text{D}_2$ systems

Figure 3.37 & Figure 3.38 show the hydrogen/deuterium desorption pressure-composition-temperature (PCT) profiles generated for $\text{Zr}_{1-x}\text{Ti}_x\text{Co-H}_2/\text{D}_2$ systems. The PCT data of $\text{ZrCo-H}_2/\text{D}_2$ system is also included in Figure 3.37 & Figure 3.38 for better composition. PCT data reveal that all the hydrides/deuterides show a single desorption plateau in the temperature range of investigation and the plateau width was found to decrease with increase in temperature. The reaction involved in the process of de-hydrogenation/de-deuteration of $\text{Zr}_{1-x}\text{Ti}_x\text{Co}$ hydride/deuteride which results in single desorption plateau for all the isotherms can be written as;



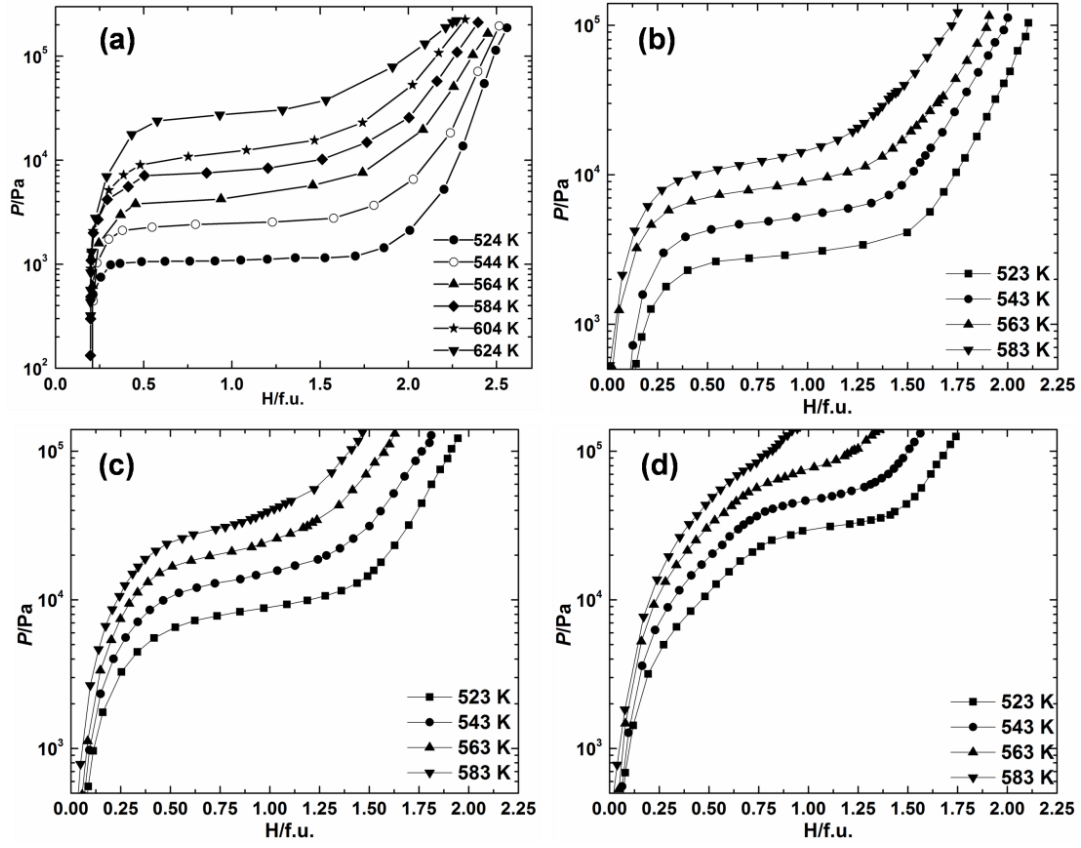


Figure 3.37: Hydrogen desorption pressure-composition isotherms for $Zr_{1-x}Ti_xCo-H_2$ systems: (a) $x = 0$, (b) $x = 0.1$ (c) $x = 0.2$ and (d) $x = 0.3$

By taking the equilibrium plateau pressure values corresponding to $X/f.u. = 1$, van't Hoff plots were constructed for the $Zr_{1-x}Ti_xCo-H_2/D_2$ systems, as shown in Figure 3.39. The van't Hoff relations obtained for $Zr_{1-x}Ti_xCo-H_2/D_2$ systems are as follows;

$Zr_{1-x}Ti_xCo-H_2$ systems:

$$\log(P/Pa) = -3474/(T/K) + 10.1 \quad (x = 0.1) \quad (3.19)$$

$$\log(P/Pa) = -3327/(T/K) + 10.3 \quad (x = 0.2) \quad (3.20)$$

$$\log(P/Pa) = -3012/(T/K) + 10.3 \quad (x = 0.3) \quad (3.21)$$

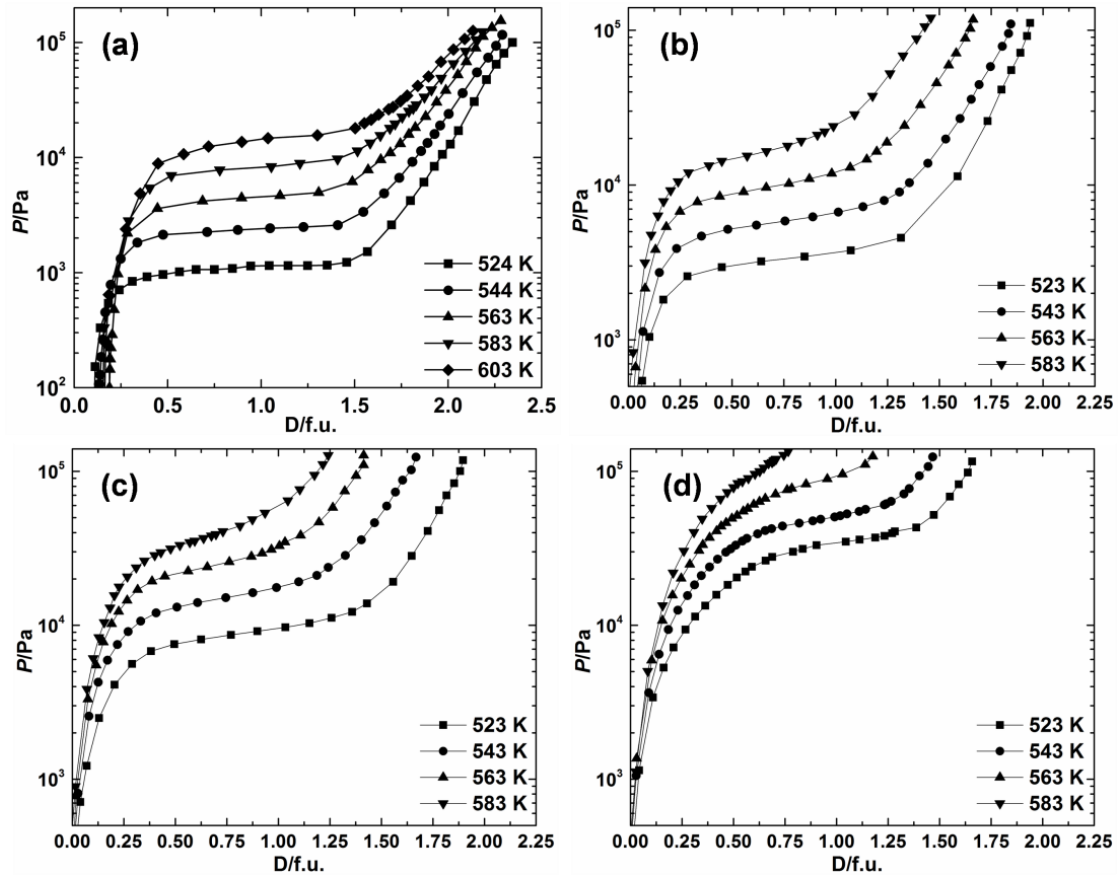


Figure 3.38: Deuterium desorption pressure-composition isotherms for $Zr_{1-x}Ti_xCo-D_2$ systems: (a) $x = 0$, (b) $x = 0.1$ (c) $x = 0.2$ and (d) $x = 0.3$

$Zr_{1-x}Ti_xCo-D_2$ systems:

$$\log(P/Pa) = -3753/(T/K) + 10.7 \quad (x = 0.1) \quad (3.22)$$

$$\log(P/Pa) = -3532/(T/K) + 10.7 \quad (x = 0.2) \quad (3.23)$$

$$\log(P/Pa) = -3095/(T/K) + 10.5 \quad (x = 0.3) \quad (3.24)$$

The enthalpy and entropy change for the de-hydrogenation/de-deuterartion of $Zr_{1-x}Ti_xCo$ hydrides/deuterides were derived from the van't Hoff relations, at the average experimental temperature of 563 K, and listed in Table 3.11..

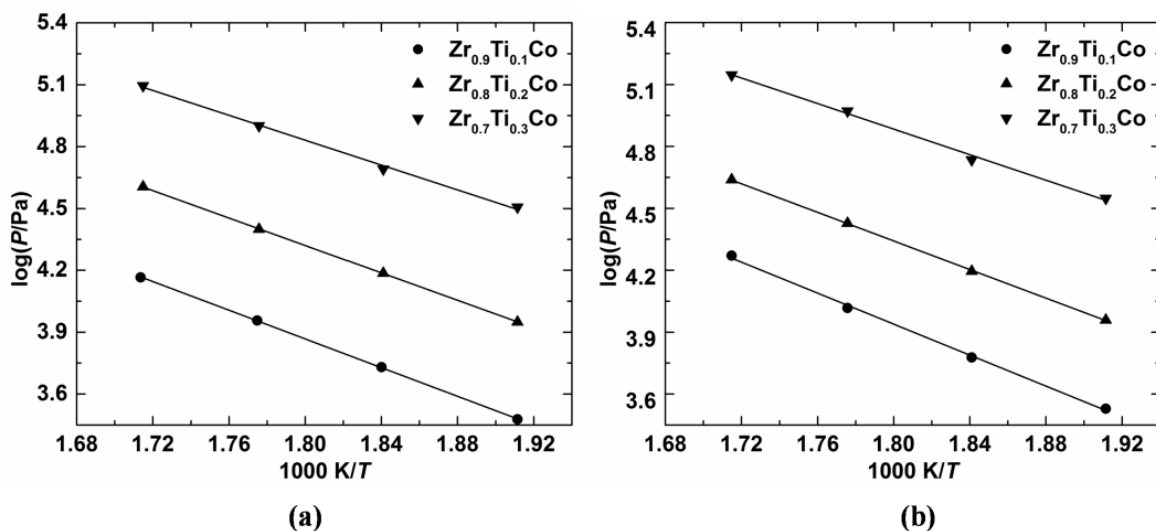


Figure 3.39: van't Hoff plots for (a) $Zr_{1-x}Ti_xCo-H_2$ and (b) $Zr_{1-x}Ti_xCo-D_2$ systems.

To the best of our knowledge, there is very limited data reported on $Zr_{1-x}Ti_xCo-H_2$ systems [68, 71, 105, 106] and no one has reported the data on $Zr_{1-x}Ti_xCo-D_2$ systems. Also, the data reported [68, 71, 105] on $Zr_{1-x}Ti_xCo-H_2$ systems show considerable scatter. Table 3.11 reveals that the enthalpy and entropy of dehydrogenation reaction changes substantially on substitution of Zr with Ti. Also the enthalpy change for de-hydrogenation/de-deuteration reactions of Ti substituted hydrides/deuterides is found to be lower than that of pure ZrCo hydrides/deuterides. Therefore, the trend observed in this study shows that Ti-substitution is destabilizing the hydride phase due to which desorption plateau pressure increases. It can be seen from Table 1.4, that zirconium hydride is more stable than that of titanium hydride, which may results in the lower value of enthalpy of formation for Ti substituted hydrides than that of pure ZrCo hydride. This is purely based on general analogy that when a strong-hydring element such as Zr is replaced by a comparatively less-hydring element such as Ti, the stability of hydride phase is supposed to decrease. In addition to that, it is also evident from Table 3.10 that substitution of Zr with Ti decreases the lattice parameter and cell volume, which in turn decreases the stability of corresponding hydride. In this context, Lundin et al. [101] have tried to correlate the effect of interstitial hole size on the stability of hydrides of AB- and AB₅-type intermetallic compounds. They have observed that the

decrease in tetrahedral hole size decreases the stability of hydrides. However, to apply these correlations to explain the trend observed in the present study, it is essential to know the effect of Ti content on the interstitial hole sizes in the $\text{Zr}_{1-x}\text{Ti}_x\text{Co}$ alloys which has to be generated by further experiments or modeling. Effect of Ti content on desorption plateau pressure can be envisioned from Figure 3.39, which unveil that desorption plateau pressure in $\text{Zr}_{1-x}\text{Ti}_x\text{Co-H}_2$ system increases with increasing the Ti-content.

Table 3.11: Thermodynamic functions for desorption of hydrogen/deuterium in $\text{Zr}_{1-x}\text{Ti}_x\text{Co-H}_2/\text{D}_2$ systems.

| System | | $\Delta_r H^\circ$ (kJ/mole H_2) | $\Delta_r S^\circ$ (J/(mole $\text{H}_2 \cdot \text{K}$)) | T_{des} (K) |
|---|-----------|---|---|----------------------|
| ZrCo | Hydride | 83.7 ± 3.9 | 122.2 ± 3.9 | 683 |
| | Deuteride | 84.3 ± 0.6 | 124.5 ± 1.1 | 677 |
| $\text{Zr}_{0.9}\text{Ti}_{0.1}\text{Co}$ | Hydride | 66.5 ± 0.3 | 97.7 ± 0.2 | 681 |
| | Deuteride | 71.9 ± 1.9 | 109.1 ± 1.8 | 658 |
| $\text{Zr}_{0.8}\text{Ti}_{0.2}\text{Co}$ | Hydride | 63.7 ± 0.2 | 101.5 ± 0.2 | 628 |
| | Deuteride | 67.6 ± 0.3 | 109.1 ± 0.3 | 620 |
| $\text{Zr}_{0.7}\text{Ti}_{0.3}\text{Co}$ | Hydride | 57.7 ± 2.0 | 101.5 ± 1.9 | 568 |
| | Deuteride | 59.3 ± 2.5 | 105.3 ± 2.4 | 563 |

Desorption temperature (T_{des}) for the $\text{Zr}_{1-x}\text{Ti}_x\text{Co-H}_2/\text{D}_2$ systems were derived from the van't Hoff relations and listed in Table 3.11. It is observed that the T_{des} decreases with increase in Ti-content, which suggests that Ti-substituted ZrCo alloys have favorable properties over pure ZrCo alloy for their use in ITER SDS.

A comparison of thermodynamic parameters for $\text{Zr}_{1-x}\text{Ti}_x\text{Co-H}_2$ and $\text{Zr}_{1-x}\text{Ti}_x\text{Co-D}_2$, Table 3.11, reveal that the equilibrium plateau pressure for $\text{Zr}_{1-x}\text{Ti}_x\text{Co-D}_2$ systems is higher than that of $\text{Zr}_{1-x}\text{Ti}_x\text{Co-H}_2$ systems which is expected based on normal hydrogen isotope effect [40]. Section-3.1.3 deals with the detailed discussion about the parameters governing the net

hydrogen isotope effect on the equilibrium pressure of hydrogen. Table 3.11 reveals that the enthalpy and entropy of dehydrogenation reaction changes substantially on substitution of Zr with Ti. Also the enthalpy change for de-hydrogenation/de-deuteration reactions of Ti substituted hydrides/deuterides is found to be lower than that of pure ZrCo hydrides/deuterides. Therefore, the trend observed in this study shows that Ti-substitution is destabilizing the hydride phase due to which desorption plateau pressure increases. It can be seen from Table 1.4, that zirconium hydride is more stable than that of titanium hydride, which may results in the lower value of enthalpy of formation for Ti substituted hydrides than that of pure ZrCo hydride. This is purely based on general analogy that when a strong-hydring element such as Zr is replaced by a comparatively less-hydring element such as Ti, the stability of hydride phase is supposed to decrease. In addition to that, it is also evident from Table 3.10 that substitution of Zr with Ti decreases the lattice parameter and cell volume, which in turn decreases the stability of corresponding hydride. In this context, Lundin et al. [101] have tried to correlate the effect of interstitial hole size on the stability of hydrides of AB- and AB₅-type intermetallic compounds. They have observed that the decrease in tetrahedral hole size decreases the stability of hydrides. However, to apply these correlations to explain the trend observed in the present study, it is essential to know the effect of Ti content on the interstitial hole sizes in the Zr_{1-x}Ti_xCo alloys which has to be generated by further experiments or modeling. Effect of Ti content on desorption plateau pressure can be envisioned from Figure 3.39, which unveil that desorption plateau pressure in Zr_{1-x}Ti_xCo-H₂ system increases with increasing the Ti-content.

Table 3.11 unveil that there is a substantial isotopic effect on the enthalpy of dehydrogenation/de-deuteration for Zr_{1-x}Ti_xCo-H₂/D₂ systems. Also the entropy of desorption reaction ($\Delta_r S^\circ$) for deuterides is higher than that of hydrides. The interplay of enthalpy and entropy of desorption reaction for hydrides and deuterides decides the net hydrogen isotope

effect. A normal isotope effect is observed for all the $\text{Zr}_{1-x}\text{Ti}_x\text{Co}$ alloys which lead to higher equilibrium pressure of deuterium than that of hydrogen at a particular temperature. The normal isotope effect for all $\text{Zr}_{1-x}\text{Ti}_x\text{Co}$ alloys can also be confirmed from Table 3.11, which indicates the lower desorption temperature (T_{des}) for the deuterides than the corresponding hydrides. Considering the normal hydrogen isotope effect, the trend of equilibrium pressure for all $\text{Zr}_{1-x}\text{Ti}_x\text{Co}$ alloys will be as follows: $p(\text{T}_2) > p(\text{D}_2) > p(\text{H}_2)$.

3.5 Structural studies on Zr-Co-M deuterides

3.5.1 Neutron diffraction studies on $\text{ZrCo}_{1-x}\text{Ni}_x$ deuterides

Irodova et al. [107] reported that the ZrCoH_3 is isostructural with the ZrNiH_3 . Though having similar structure, the hydrogen induced disproportionation behavior of both the compound is different. ZrNiH_3 has higher durability against hydrogen induced disproportionation [108] in comparison to ZrCoH_3 . However, ZrNi alloy is not useful for storage of hydrogen isotopes as it has dual plateau region in the pressure-composition isotherms (PCIs) [109]. In our previous discussion in Section-0, we have shown that Ni substituted compounds $\text{ZrCo}_{1-x}\text{Ni}_x\text{H}_3$ ($x = 0.1, 0.2$ and 0.3) have improved hydrogen storage properties over ZrCo. It was also reported, that with increase in Ni content the dissociation temperature for supply of 100 kPa of hydrogen decreases and the the durability against hydrogen induced disproportionation increases. Since the structures of both ZrCoH_3 and ZrNiH_3 are same, this gives a clue that difference between hydrogen storage properties of these compound can be attributed to occupancy of hydrogen in different interstitial sites. In the *Cmcm* space group the possible crystallographic sites for hydrogen occupation has been classified into three groups and the sites were identified by Wyckoff's notation [110]:

(1) $4c_1$ sites surrounded by 4 Zr atoms at $(0\ y\ 1/4)$ lattice position.

(2) $4c_2$, $8g_1$ and $8f_1$ site surrounded by 3 Zr and 1 Co/Ni atoms at $(0\ y\ 1/4)$, $(x\ y\ 1/4)$ and $(0\ y\ z)$ respectively. The $4c_2$ site is located in a bipyramid made by a common triangular base of 3 Zr atoms and 2 Co/Ni atoms at the summit [64].

(3) $8f_2$ and $8e$ sites surrounded by 2 Zr and 2 Co/Ni atoms at $(0\ y\ z)$ and $(x\ 0\ 0)$ respectively.

Simultaneous occupation of all these sites is not possible because as per Switendick criteria [111], only those metal hydrides are stable in which H-H distance is 2.1 Å or more. In addition to that Lundin et al. [101], also reported that for formation of a stable hydride the hole radii of interstitial site which is being occupied by hydrogen atom should be larger than

0.39 Å. Based on these criterias Westlake [96], had proposed that for ZrCoH_3 only $4c_2$ and $8f_1$ sites are occupied by hydrogen atoms which was in accordance with the neutron diffraction results of Irodova et al. [107]. These occupancies were exactly the same as for ZrNiH_3 [112]. However, Jacob and Bloch [113] proposed another model based on Fermi distribution function which allowed the partial occupancies for aforementioned three group of sites. They predicted partial occupancy of $8f_2$ and $8e$ sites. Further, Bekris et al. [64] have predicted from their DSC data that ~4% of hydrogen occupies the interstitial sites in which the Zr-H distance is shorter than that of Zr-H distance in ZrH_2 . However, none of the above confirm their predictions by any experimental method. Hence, to fully understand the difference in disproportionation behaviour of ZrCoH_3 , $\text{ZrCo}_{1-x}\text{Ni}_x\text{H}_3$, $\text{ZrCo}_{0.9}\text{Fe}_{0.1}\text{H}_3$, and $\text{Zr}_{1-x}\text{Ti}_x\text{CoH}_3$, though they have similar crystal structure, it was felt necessary to study the interstitial site occupancies of hydrogen in these compounds. As XRD cannot locate hydrogen in the lattice, therefore to locate sites of hydrogen occupancy direct experimental technique like neutron powder diffraction (NPD) was utilized in the present investigation.

Owing to high incoherent scattering nature of hydrogen atom, it was not possible to perform the neutron powder diffraction experiments with hydrides. Therefore, the NPD experiments were carried out on $\text{ZrCo}_{1-x}\text{Ni}_x$ deuterides. Since, XRD method gives the higher accuracy of lattice parameters than that of NPD method, the lattice parameter obtained from XRD analysis were used in the refinement of NPD data. The X-ray diffraction patterns of all $\text{ZrCo}_{1-x}\text{Ni}_x$ deuterides are shown in Figure 3.11. The XRD analysis revealed formation of single orthorhombic phase (space group *Cmcm*) similar to ZrCoD_3 for all $\text{ZrCo}_{1-x}\text{Ni}_x$ deuterides. The lattice parameters and unit cell volumes of $\text{ZrCo}_{1-x}\text{Ni}_x$ deuterides were calculated by Rietveld refinement of XRD data and are listed in Table 3.12. A typical Rietveld refinement pattern of $\text{ZrCo}_{0.9}\text{Ni}_{0.1}\text{D}_3$ is shown in Figure 3.40. It is evident from Table 3.12 that parameter a decreases while b , c and unit cell volume increases with increase in Ni content.

Rietveld refinement of neutron diffraction data was carried out by varying the background, occupancies and position of atoms. The refinement results are listed in Table 3.13. A typical neutron diffraction pattern of $\text{ZrCo}_{0.8}\text{Ni}_{0.2}\text{D}_3$ is shown in Figure 3.41.

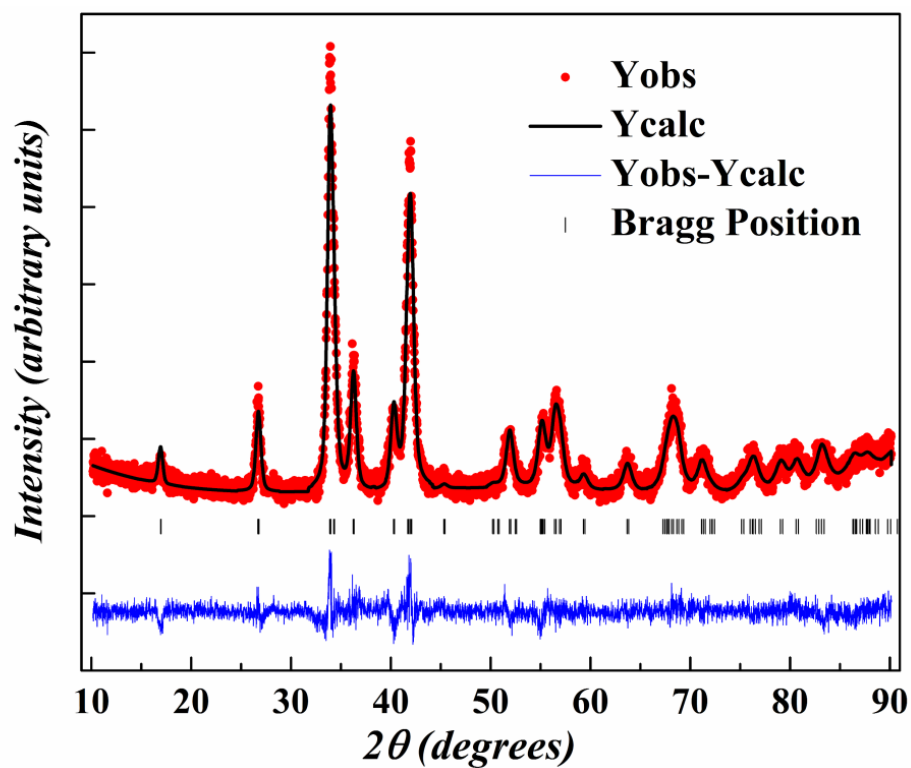


Figure 3.40: Rietveld refinement of X-ray diffraction pattern of $\text{ZrCo}_{0.9}\text{Ni}_{0.1}\text{D}_3$.

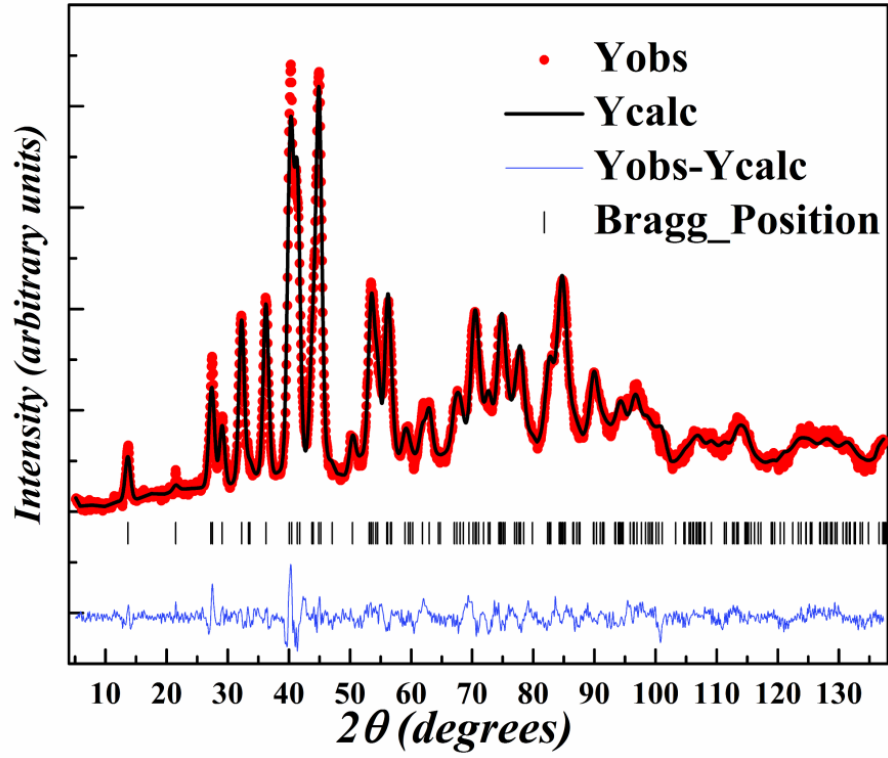


Figure 3.41: Rietveld refinement of neutron diffraction pattern of $\text{ZrCo}_{0.8}\text{Ni}_{0.2}\text{D}_3$.

Table 3.12: Lattice parameter and unit cell volumes of $\text{ZrCo}_{1-x}\text{Ni}_x$ deuterides from Rietveld refinement of XRD data.

| System | Lattice Parameters | | | Volume [\AA^3] |
|-----------|----------------------|----------------------|----------------------|---------------------------|
| | a [\AA] | b [\AA] | c [\AA] | |
| $x = 0$ | 3.5230 ± 0.0004 | 10.4491 ± 0.0011 | 4.3276 ± 0.0005 | 159.31 ± 0.03 |
| $x = 0.1$ | 3.5217 ± 0.0004 | 10.4561 ± 0.0012 | 4.3280 ± 0.0005 | 159.37 ± 0.03 |
| $x = 0.2$ | 3.5211 ± 0.0003 | 10.4679 ± 0.0010 | 4.3288 ± 0.0004 | 159.55 ± 0.02 |
| $x = 0.3$ | 3.5164 ± 0.0004 | 10.4877 ± 0.0011 | 4.3293 ± 0.0005 | 159.66 ± 0.03 |

Table 3.13: Rietveld refinement results of neutron diffraction data for $\text{ZrCo}_{1-x}\text{Ni}_x$ deuterides.

| Parameters | | x in $\text{ZrCo}_{1-x}\text{Ni}_x$ deuterides | | | |
|-------------------------|---|--|-------------|------------|------------|
| | | 0.0 | 0.1 | 0.2 | 0.3 |
| D1 ($4c_2$) (0 y 1/4) | y | 0.9269(39) | 0.9300(5) | 0.9282(3) | 0.9291(3) |
| Occupancy (%) | | 29.3 | 30.8 | 30.1 | 31.1 |
| D2 ($8f_1$) (0 y z) | y | 0.3119(2) | 0.3125(3) | 0.3122(2) | 0.3119(2) |
| | z | 0.5047(6) | 0.5047(7) | 0.5062(4) | 0.5053(4) |
| Occupancy (%) | | 66.9 | 66.4 | 67.2 | 66.4 |
| D3 ($8e$) (x 0 0) | x | 0.2219(81) | 0.2243(139) | 0.2549(88) | 0.2637(95) |
| Occupancy (%) | | 3.8 | 2.8 | 2.7 | 2.5 |
| Zr-D distance (Å) | | 1.937(12) | 1.940(20) | 1.994(14) | 2.022(15) |
| R_p (%) | | 3.29 | 6.70 | 1.81 | 2.13 |
| R_{wp} (%) | | 4.15 | 9.86 | 2.36 | 2.89 |
| R_{exp} (%) | | 3.61 | 2.46 | 1.32 | 1.40 |

The deuterium atoms were allowed to occupy $8f_2$ and $8e$ sites in addition to the earlier reported [107], $4c_2$ and $8f_1$ sites. A significant reduction in χ^2 was observed with addition of these extra sites for deuterium occupation. It was observed that among $8f_2$ and $8e$ sites, the deuterium occupies only $8e$ sites. This observation is in agreement with the Switendick criterion [111], which also prohibits the simultaneous occupation of both $8f_2$ and $8e$ sites as the H-H distance between these two sites is too small ($\sim 1.3\text{\AA}$). It can be seen from Table 3.13 that for ZrCoD_3 the occupancy of $8e$ site is $\sim 3.8\%$ which is in accord with the prediction of Bekris et al. [64]. The crystal structure of ZrCoD_3 with new deuterium site ($8e$) is shown in Figure 3.42. Variation of occupancy of new $8e$ site and Zr-D distance with Ni content in

$\text{ZrCo}_{1-x}\text{Ni}_x\text{D}_3$ are also shown in Figure 3.43. It is evident from Figure 3.43 that the occupancy of new $8e$ site decreases with increase in Ni content, from $\sim 3.8\%$ for ZrCoD_3 to $\sim 2.5\%$ for $\text{ZrCo}_{0.7}\text{Ni}_{0.3}\text{D}_3$. Figure 3.43 also reveals that the Zr-D distance increases from 1.937 \AA in ZrCoD_3 to 2.022 \AA in $\text{ZrCo}_{0.7}\text{Ni}_{0.3}\text{D}_3$. Since the Zr-D distance in $8e$ sites for ZrCoD_3 is smaller than Zr-D distance in ZrD_2 , the deuterium of $8e$ site is not released upon desorption and forms a stable ZrD_2 phase and therefore results partial disproportionation of material according to reaction in Eq. 1.24. Since, the occupancy of $8e$ site decreases and also the Zr-D distance for the same increases, it is desirable that the durability of $\text{ZrCo}_{1-x}\text{Ni}_x\text{D}_3$ against hydrogen induced disproportionation should increase with increase in Ni content and it has been verified by results of cyclic absorption-desorption experiments on $\text{ZrCo}_{1-x}\text{Ni}_x\text{-H}_2$ systems reported in Section-3.2.3.

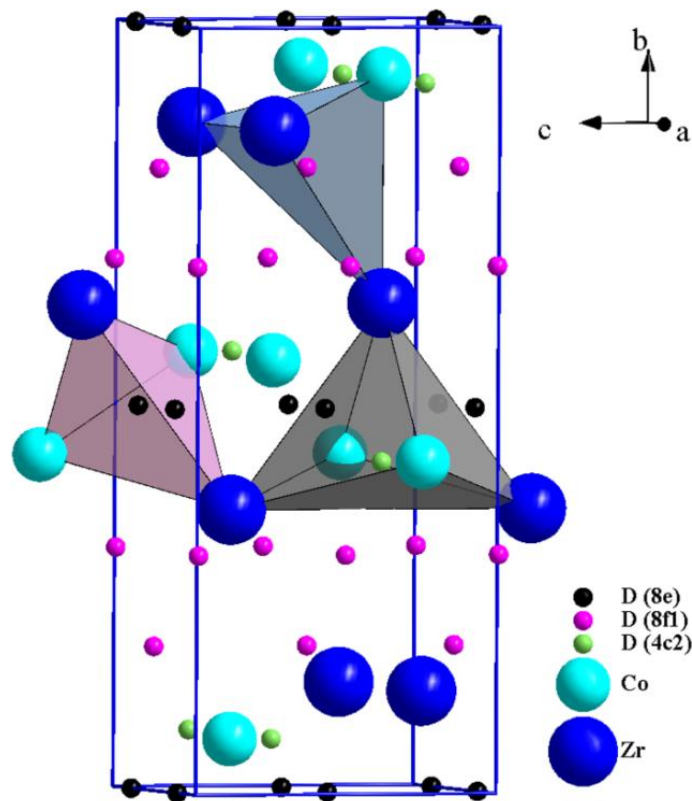


Figure 3.42: The crystal structure of ZrCoD_3 .

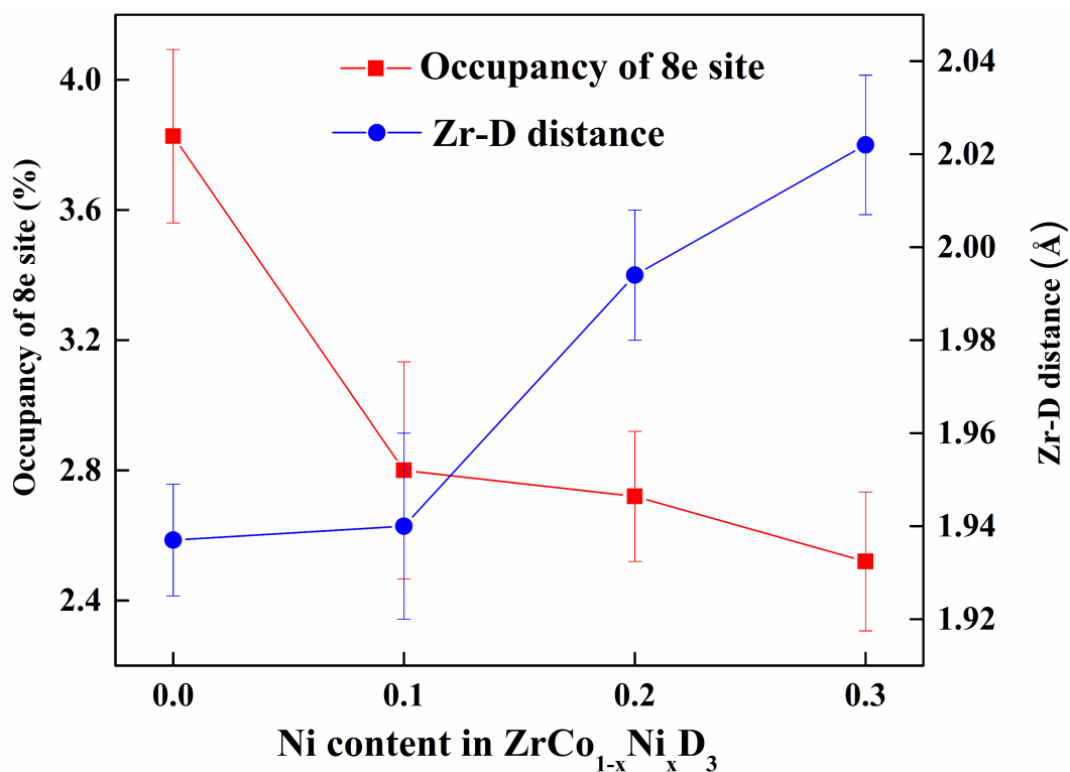


Figure 3.43: Variation of occupancy of new 8e site and Zr-D distance with Ni content in $\text{ZrCo}_{1-x}\text{Ni}_x\text{D}_3$.

3.5.2 Neutron diffraction studies on $\text{ZrCo}_{0.9}\text{Fe}_{0.1}$ deuteride

The neutron diffraction pattern (NPD) of $\text{ZrCo}_{0.9}\text{Fe}_{0.1}\text{D}_3$ is shown in Figure 3.44. Rietveld refinement of neutron diffraction data was carried out by varying the background, occupancies and position of atoms. The Rietveld refinement results of XRD and NPD data are listed in Table 3.14 and Table 3.15, respectively. The detailed structural information of ZrCoD_3 is discussed in Section-3.5.1, where it has been found that in ZrCoD_3 the deuterium occupies a new site 8e in addition to $4c_2$ and $8f_1$. For refinement of deuterium site occupancies in $\text{ZrCo}_{0.9}\text{Fe}_{0.1}\text{D}_3$, the deuterium atoms were allowed to occupy $8f_2$ and 8e sites in addition to the earlier reported [107], $4c_2$ and $8f_1$ sites. A significant reduction in χ^2 was observed with addition of these extra sites for deuterium occupation. Similar to ZrCoD_3 , it

was also observed in $\text{ZrCo}_{0.9}\text{Fe}_{0.1}\text{D}_3$ that deuterium occupies only $8e$ sites between the $8f_2$ and $8e$ sites.

The ZrH_2 and ZrCo_2 phases are thermodynamically more stable compared to ZrCoH_3 and ZrCo , due to which desorption of ZrCoH_3 leads to disproportionation of material according to reaction (1) [61, 62]. The crystal structure of ZrCo is cubic and that of ZrCoH_3 is orthorhombic, due to which considerable changes in the crystallographic position of the atoms occurs during hydrogen absorption-desorption cycles. Therefore, the knowledge of hydrogen/deuterium occupancies in different crystallographic sites plays an important role in understanding the disproportionation behavior. In Section-3.5.1, it has been reported that in ZrCoD_3 ~ 3.8% of deuterium goes to a new site $8e$. Since the Zr-D distance (1.937 Å) in $8e$ sites for ZrCoD_3 is smaller than Zr-D distance in ZrD_2 , during the desorption there is a probability that the deuterium of $8e$ site does not get released and forms a stable ZrD_2 phase thus leading to the disproportionation of the material. Hence, the occupancy of this particular site ' $8e$ ' will directly affect the extent of disproportionation of material. It is evident from Table 3.15 that, in case of $\text{ZrCo}_{0.9}\text{Fe}_{0.1}\text{D}_3$ the occupancy of new site $8e$ is found to be 1.8% which is lower than the value for ZrCoD_3 . In addition, the Zr-D distance in $8e$ site for $\text{ZrCo}_{0.9}\text{Fe}_{0.1}\text{D}_3$ is 2.201 Å which is higher than the value for ZrCoD_3 . The crystal structure of $\text{ZrCo}_{0.9}\text{Fe}_{0.1}\text{D}_3$ with new deuterium site ($8e$) is shown in Figure 3.45. Based on this decreased occupancy of $8e$ site, which is responsible for hydrogen induced disproportionation, and increased Zr-D distance it can be proposed that the durability of $\text{ZrCo}_{0.9}\text{Fe}_{0.1}\text{D}_3$ against disproportionation should be higher than that for ZrCoD_3 . This observation is also supported by cyclic absorption-desorption experiments on $\text{ZrCo}_{0.9}\text{Fe}_{0.1}\text{-H}_2$ systems, discussed in Section-3.3.3.

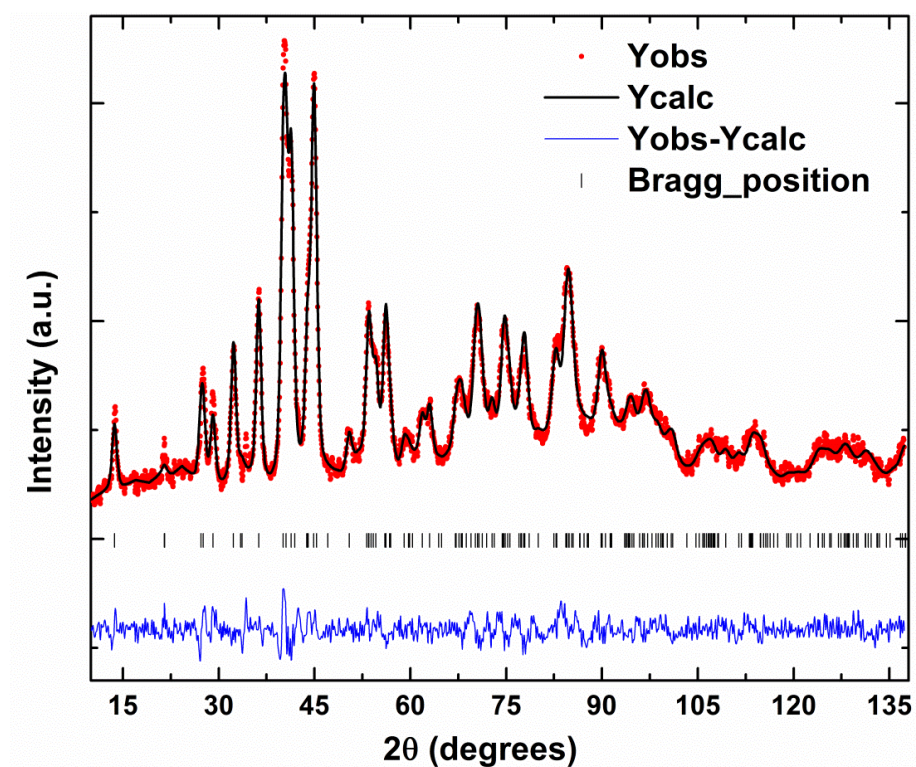


Figure 3.44: Neutron diffraction pattern of $\text{ZrCo}_{0.9}\text{Fe}_{0.1}\text{D}_3$ with Rietveld refinement.

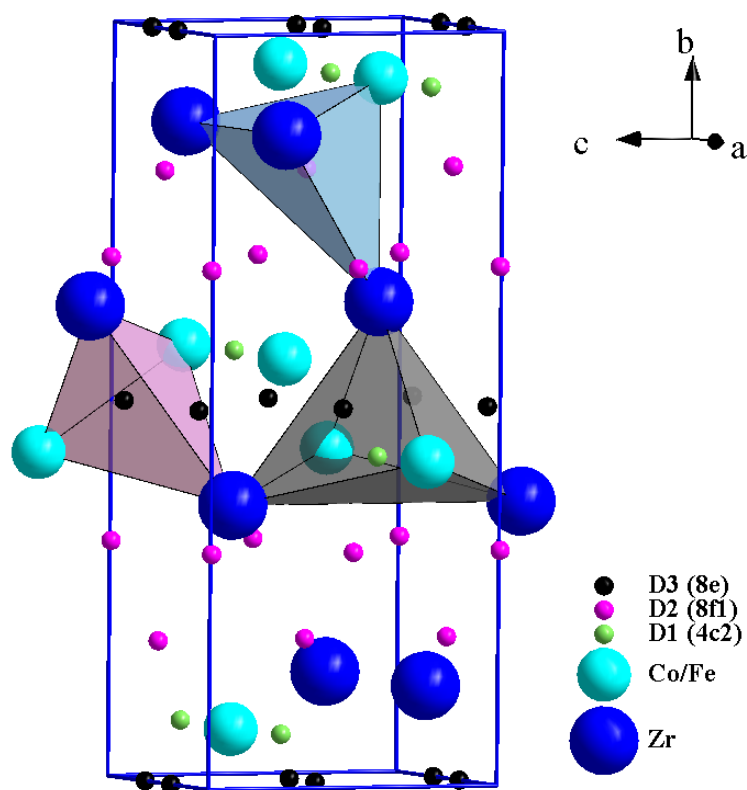


Figure 3.45: Crystal structure of $\text{ZrCo}_{0.9}\text{Fe}_{0.1}\text{D}_3$.

Table 3.14: Lattice parameters and unit cell volume of ZrCo and ZrCo_{0.9}Fe_{0.1} deuteride.

| Compound | Lattice parameter (Å) | | | Unit cell volume (Å ³) |
|--|-----------------------|-------------|-----------|------------------------------------|
| | <i>a</i> | <i>b</i> | <i>c</i> | |
| ZrCoD ₃ | 3.5230(4) | 10.4491(11) | 4.3276(5) | 159.31(3) |
| ZrCo _{0.9} Fe _{0.1} D ₃ | 3.5228(3) | 10.4414(10) | 4.3274(5) | 159.18(3) |

Table 3.15: Rietveld refinement results of neutron diffraction data for ZrCo_{1-x}Fe_x deuterides.

| Parameters | | x in ZrCo _{1-x} Fe _x deuterides | |
|---------------------------------|---|---|-----------------|
| | | 0.0 | 0.1 |
| D1 (4c ₂) (0 y 1/4) | y | 0.9269 ± 0.0039 | 0.9279 ± 0.0003 |
| Occupancy (%) | | 29.3 | 29.9 |
| D2 (8f ₁) (0 y z) | y | 0.3119 ± 0.0002 | 0.3119 ± 0.0002 |
| | z | 0.5047 ± 0.0006 | 0.5041 ± 0.0005 |
| Occupancy (%) | | 66.9 | 68.3 |
| D3 (8e) (x 0 0) | x | 0.2219 ± 0.0081 | 0.3725 ± 0.0139 |
| Occupancy (%) | | 3.8 | 1.8 |
| Zr-D distance (Å) | | 1.937 ± 0.012 | 2.201 ± 0.030 |
| <i>R</i> _p (%) | | 3.29 | 1.93 |
| <i>R</i> _{wp} (%) | | 4.15 | 2.45 |
| <i>R</i> _{exp} (%) | | 3.61 | 1.81 |

3.5.3 Neutron diffraction studies on $\text{Zr}_{1-x}\text{Ti}_x\text{Co}$ deuterides

NPD measurements were carried out on $\text{Zr}_{1-x}\text{Ti}_x\text{Co}$ deuterides and a schematic neutron diffraction pattern (NPD) of $\text{Zr}_{0.8}\text{Ti}_{0.2}\text{CoD}_3$ is shown in Figure 3.46. Rietveld refinement of neutron diffraction data was carried out by varying the background, occupancies and position of atoms. The Rietveld refinement results of XRD and NPD data are listed in Table 3.16 and Table 3.17, respectively. It is evident from Table 3.16 that all lattice parameters a , b , c and unit cell volume is decreases with increase in Ti content. The detailed structural information of ZrCoD_3 is discussed in Section-3.5.1, where it has been found that in ZrCoD_3 the deuterium occupies a new site $8e$ in addition to $4c_2$ and $8f_1$.

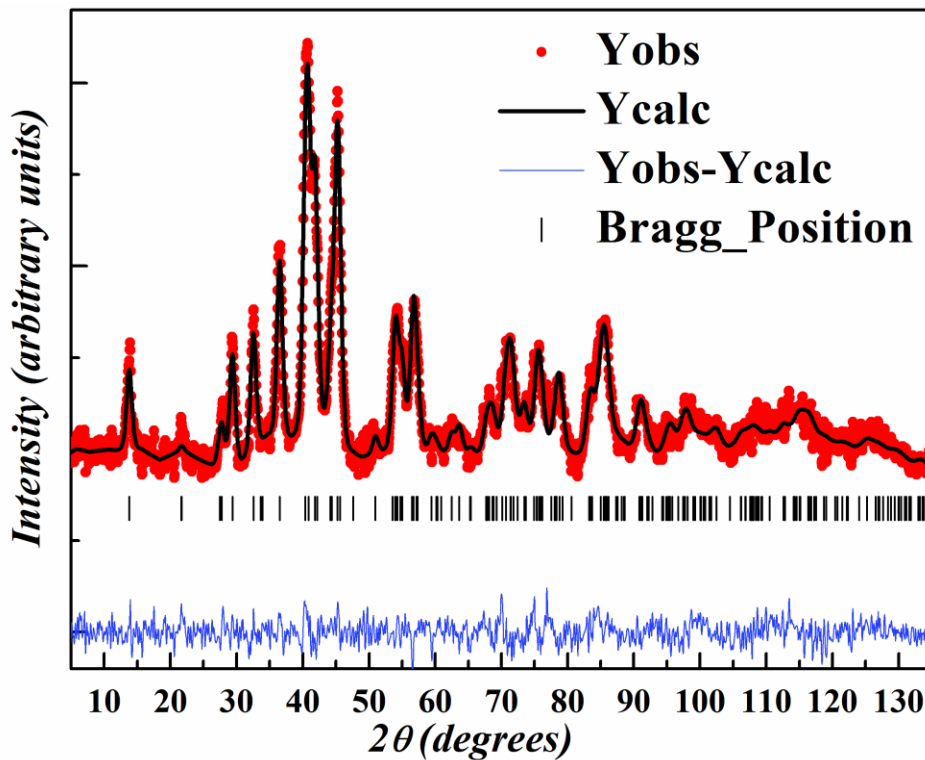


Figure 3.46: Neutron diffraction pattern of $\text{Zr}_{0.8}\text{Ti}_{0.2}\text{CoD}_3$ with Rietveld refinement.

Table 3.16: Lattice parameter and unit cell volumes of $\text{Zr}_{1-x}\text{Ti}_x\text{Co}$ deuterides from Rietveld refinement of XRD data.

| System | Lattice Parameters | | | Volume [\AA^3] |
|-----------|----------------------|----------------------|----------------------|---------------------------|
| | a [\AA] | b [\AA] | c [\AA] | |
| $x = 0$ | 3.5230(4) | 10.4491(11) | 4.3276(5) | 159.31(3) |
| $x = 0.1$ | 3.5041(3) | 10.4120(9) | 4.3160(4) | 157.47(2) |
| $x = 0.2$ | 3.4852(3) | 10.3773(11) | 4.3018(5) | 155.58(3) |
| $x = 0.3$ | 3.4616(3) | 10.3362(11) | 4.2863(5) | 153.36(3) |

Table 3.17: Rietveld refinement results of neutron diffraction data for $\text{Zr}_{1-x}\text{Ti}_x\text{Co}$ deuterides.

| Parameters | | x in $\text{Zr}_{1-x}\text{Ti}_x\text{Co}$ deuterides | | | |
|--------------------------------|---|---|-------------|-------------|-------------|
| | | 0.0 | 0.1 | 0.2 | 0.3 |
| D1 ($4c_2$) (0 y 1/4) | y | 0.9269(39) | 0.9289(4) | 0.9273(4) | 0.9270(4) |
| Occupancy (%) | | 29.3 | 29.7 | 29.9 | 30.0 |
| D2 ($8f_1$) (0 y z) | y | 0.3119(2) | 0.3124(3) | 0.3117(3) | 0.3110(3) |
| | z | 0.5047(6) | 0.5046(7) | 0.5059(7) | 0.5059(8) |
| Occupancy (%) | | 66.9 | 68.4 | 68.4 | 68.0 |
| D3 ($8e$) (x 0 0) | x | 0.2219(81) | 0.4135(204) | 0.2872(197) | 0.2846(178) |
| Occupancy (%) | | 3.8 | 1.8 | 1.7 | 2.0 |
| Zr-D distance (\AA) | | 1.937(12) | 2.280(40) | 2.030(30) | 2.020(30) |
| R_p (%) | | 3.29 | 4.46 | 3.76 | 2.13 |
| R_{wp} (%) | | 4.15 | 5.57 | 4.78 | 2.89 |
| R_{exp} (%) | | 3.61 | 3.14 | 2.92 | 1.40 |

During the refinement of NPD data of $\text{Zr}_{1-x}\text{Ti}_x\text{Co}$ deuterides, the deuterium atoms were allowed to occupy $8f_2$ and $8e$ sites in addition to the earlier reported [107], $4c_2$ and $8f_1$ sites. A significant reduction in χ^2 was observed with addition of these extra sites for deuterium occupation. Alike other Ni or Fe substituted Zr-Co-M deuterides, for $\text{Zr}_{1-x}\text{Ti}_x\text{Co}$ deuterides also it was observed that among $8f_2$ and $8e$ sites the deuterium occupies only $8e$ sites. This phenomenon is in accordance with the Switendick criterion [111], which also prohibits the simultaneous occupation of both $8f_2$ and $8e$ sites as the H-H distance between these two sites is too small ($\sim 1.3\text{\AA}$). Variation of $8e$ site occupancy and its Zr-D distance with Ti content in $\text{Zr}_{1-x}\text{Ti}_x\text{CoD}_3$ is shown in Figure 3.48. As is evident from Table 3.13, the occupancy of $8e$ site in ZrCoD_3 is $\sim 3.8\%$ which is in accord with the prediction of Bekris et al. [64]. Since, the Zr-D distance (1.937\AA) in $8e$ site for ZrCoD_3 is smaller than Zr-D distance in ZrD_2 , the deuterium of $8e$ site does not get released upon desorption and forms a stable ZrD_2 phase thus leading to the partial disproportionation of the material. It is evident from Figure 3.48 that, Ti substitution for Zr ($x=0.1$) significantly decreases the occupancy of $8e$ site and also increases the Zr-D distance for this site. Further decrease in Zr-D distance with increase in Ti content can be attributed to the lattice contraction upon substitution of Zr with Ti, which is smaller in size. Occupancy of $8e$ site with Ti content was found to remain constant within the error limits. The lowest occupancy of $8e$ site was found to be 1.7% for $\text{Zr}_{0.8}\text{Ti}_{0.2}\text{CoD}_3$. The crystal structure of $\text{Zr}_{0.8}\text{Ti}_{0.2}\text{CoD}_3$ with new deuterium site ($8e$) is shown in Figure 3.47. Based on this decreased occupancy of $8e$ site, which is responsible for hydrogen induced disproportionation, and increased Zr-D distance it can be proposed that the durability of $\text{Zr}_{1-x}\text{Ti}_x\text{CoD}_3$ against disproportionation should be higher than that for ZrCoD_3 .

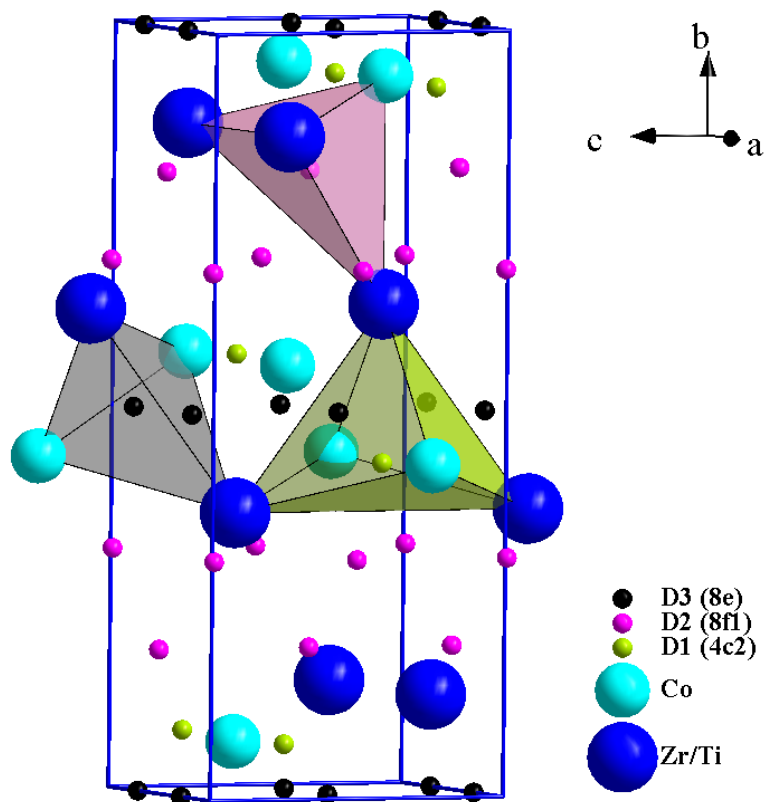


Figure 3.47: Crystal structure of $\text{Zr}_{0.8}\text{Ti}_{0.2}\text{CoD}_3$.

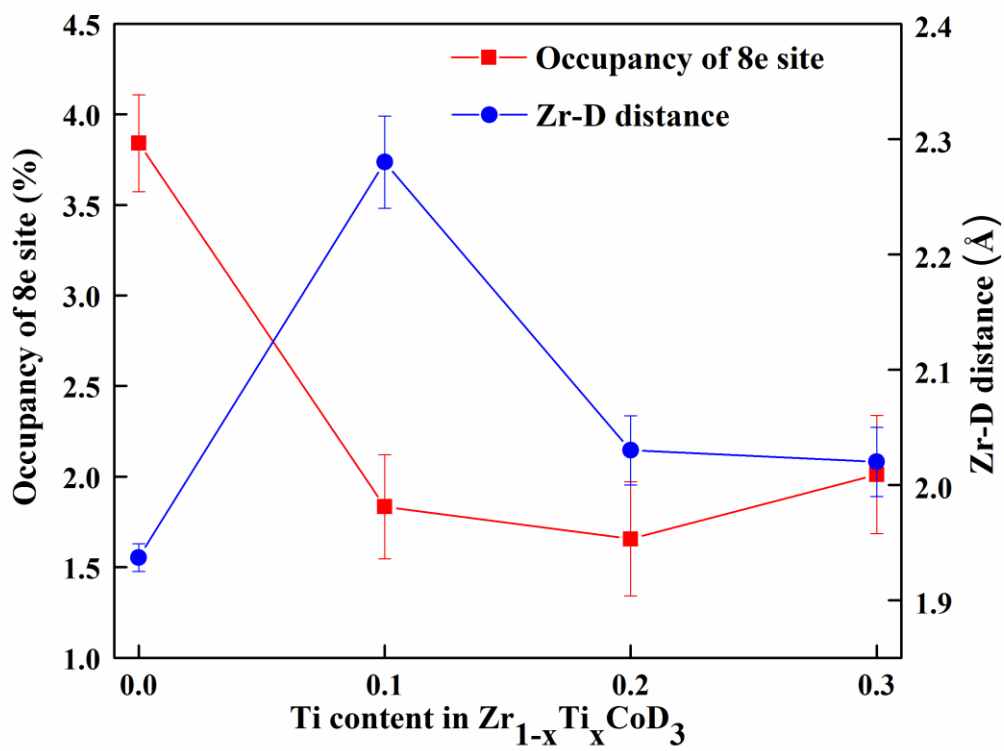


Figure 3.48: Variation of occupancy of new $8e$ site and Zr-D distance with Ti content in $\text{Zr}_{1-x}\text{Ti}_x\text{CoD}_3$.

3.6 Isothermal disproportionation behavior of Zr-Co-M ternary alloys

Isothermal disproportionation studies were carried out on all Zr-Co-M ternary alloys, to compare thier hydrogen induced disproportionation nature and to find the most suitable ternary alloy having high durability against disproportionation. In this context, the isothermal disproportionation behavior of hydrides of these alloys were investigated at 750 K, the maximum possible desorption temperature, under delivery conditions, i.e. hydrogen over pressure around ≥ 1 bar. For this purpose, the hydride phase was heated to 750 K and the over pressure of hydrogen in the system was selected accordingly to get the hydrogen pressure above 1 bar. Thereafter, the system under this condition was kept isothermal at 750 K for 10 hours and then cooled to room temperature. The change of system pressure is monitored with time and temperature and shown in Figure 3.50.

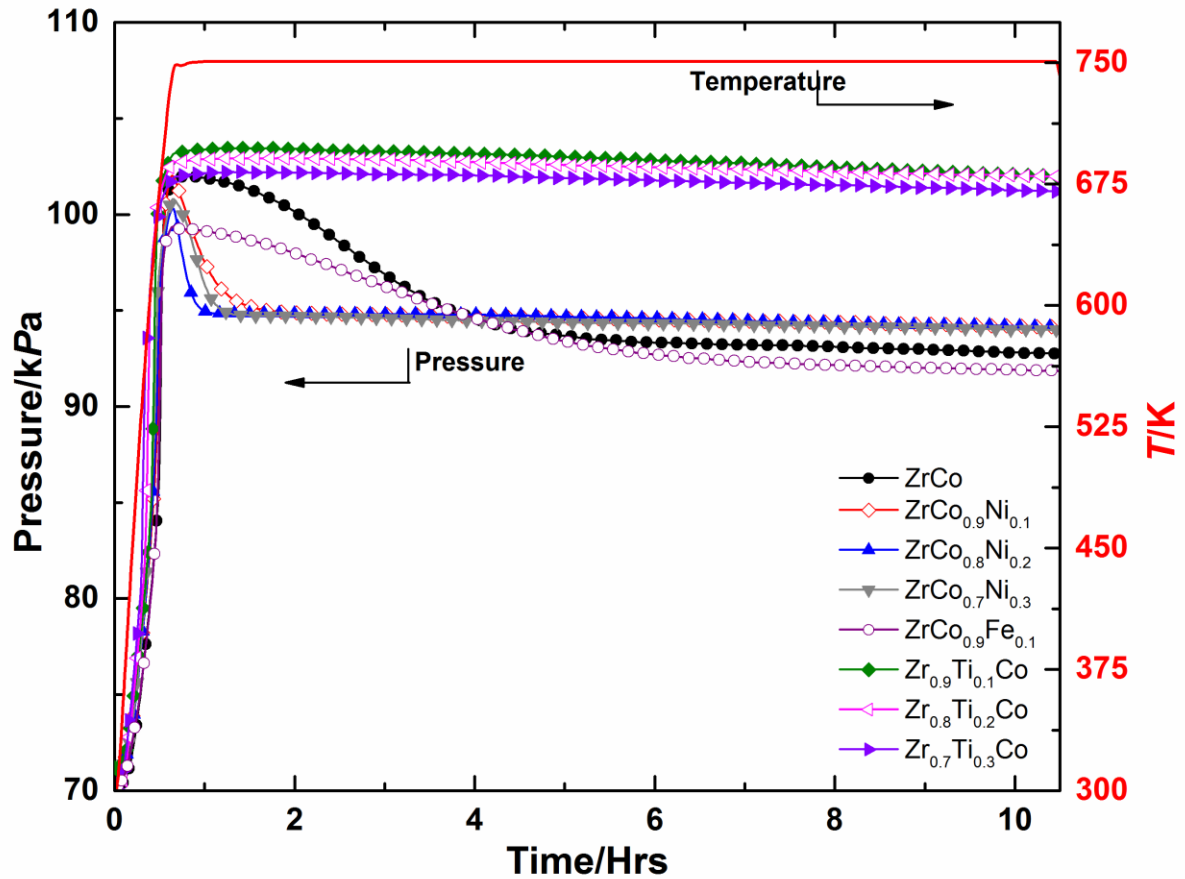


Figure 3.49: Change in pressure with time for Zr-Co-M-H₂ systems at 750 K.

It is evident from Figure 3.50 that the system pressure initially increases rapidly with increase in temperature which is due to desorption of hydrogen from the Zr-Co-M hydride phase. In isothermal condition at 750 K, the behavior of pressure change with time is different for different ternary alloys.

For ZrCo-H₂ system, after attaining the final temperature of 750 K the system pressure remains constant for around 25 minutes and then decreases gradually till an equilibrium is reached. The existence of induction period in the disproportionation of ZrCo-H₂ system is in consistent with the reported literature [65, 105]. The reduction of system pressure can be attributed to the disproportionation of ZrCoH₃ to thermodynamically more stable ZrH₂ and ZrCo₂ phases [114, 115] according to following reaction;



It is important to note that at 750 K, the plateau equilibrium pressure of hydrogen over ZrH₂ is very less (~100 Pa) [33], hence the pressure in the system is due to the presence of extra hydrogen.

In order to see the phase changes during the course of isothermal conditions, the Zr-Co-M hydrides before and after disproportionation studies were characterized by XRD. Figure 3.50 shows the XRD patterns before isothermal studies, which indicates the formation of single orthorhombic phase, similar to that of ZrCoH₃ for all Zr-Co-M hydrides. XRD patterns of all Zr-Co-M-H₂ systems after disproportionation studies is shown in Figure 3.51.

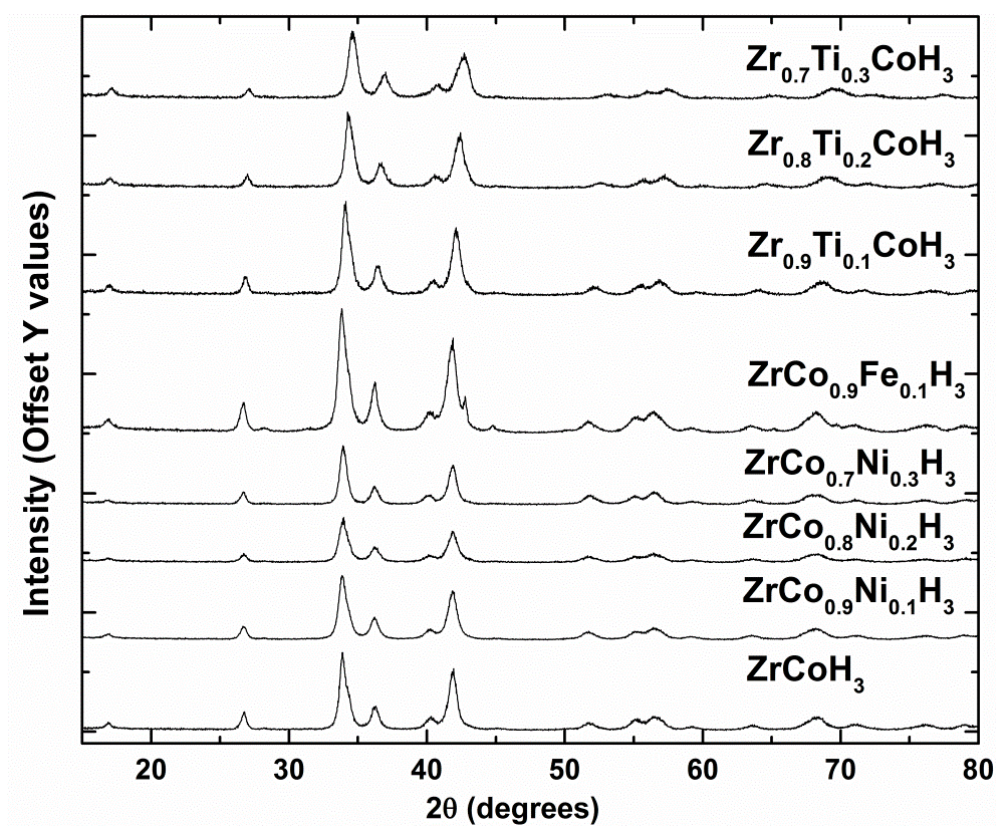


Figure 3.50: XRD patterns of Zr-Co-M hydrides before disproportionation studies.

It is evident from Figure 3.51 that ZrCoH_3 is completely converted into the more stable phases ZrH_2 and ZrCo_2 formed according to the above mentioned disproportionation reaction, Eq. 3.25, which is in line with the observations reported in literature [62, 65, 105, 108, 116, 117].

Figure 3.50 reveals that, for $\text{ZrCo}_{1-x}\text{Ni}_x\text{-H}_2$ systems the disproportionation reaction is very fast without any induction period. Similar behavior is observed for $\text{ZrCo}_{0.9}\text{Fe}_{0.1}\text{-H}_2$, however disproportionation has some induction period of around 25 minutes, same as ZrCo-H_2 system. XRD of both $\text{ZrCo}_{1-x}\text{Ni}_x\text{-H}_2$ and $\text{ZrCo}_{0.9}\text{Fe}_{0.1}\text{-H}_2$ systems after disproportionation experiments, Figure 3.51, indicates the peaks corresponding to ZrH_2 and ZrCo_2 phases, thereby resulting the complete disproportionation of these ternary alloys.

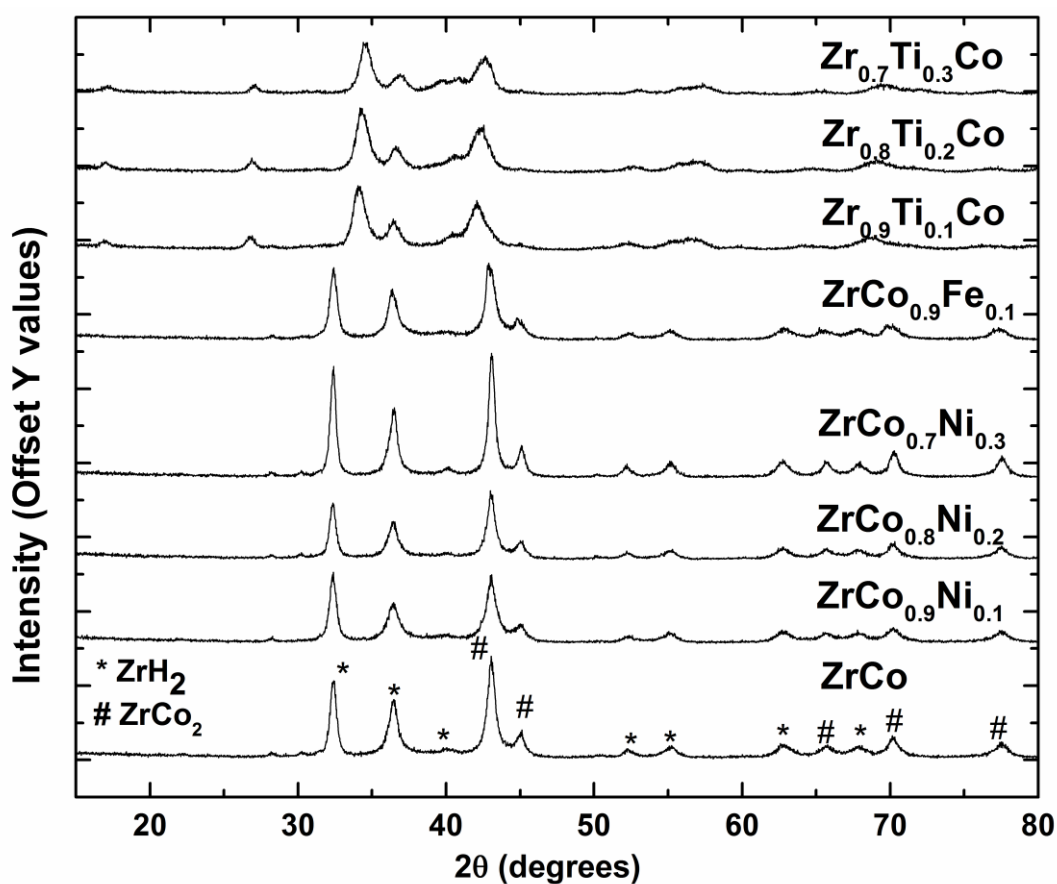


Figure 3.51: XRD patterns of Zr-Co-M hydrides after disproportionation studies.

Hence, ternary alloying of ZrCo with both Ni and Fe catalyse the disproportionation reaction. However, the disproportion rate has been found to be lower for Fe substituted alloy than that of Ni substituted alloys. Similar behavior of hydrogen induced disproportionation is reported by Zhang et al. [105] for $\text{ZrCo}_{0.8}\text{Ni}_{0.2}$ alloy.

For $\text{Zr}_{1-x}\text{Ti}_x\text{Co-H}_2$ systems, it can be seen from Figure 3.50 that system hydrogen pressure remains almost constant during the course of isothermal condition. A magnification view of pressure vs. time plot for $\text{Zr}_{1-x}\text{Ti}_x\text{Co-H}_2$ systems is shown in Figure 3.52.

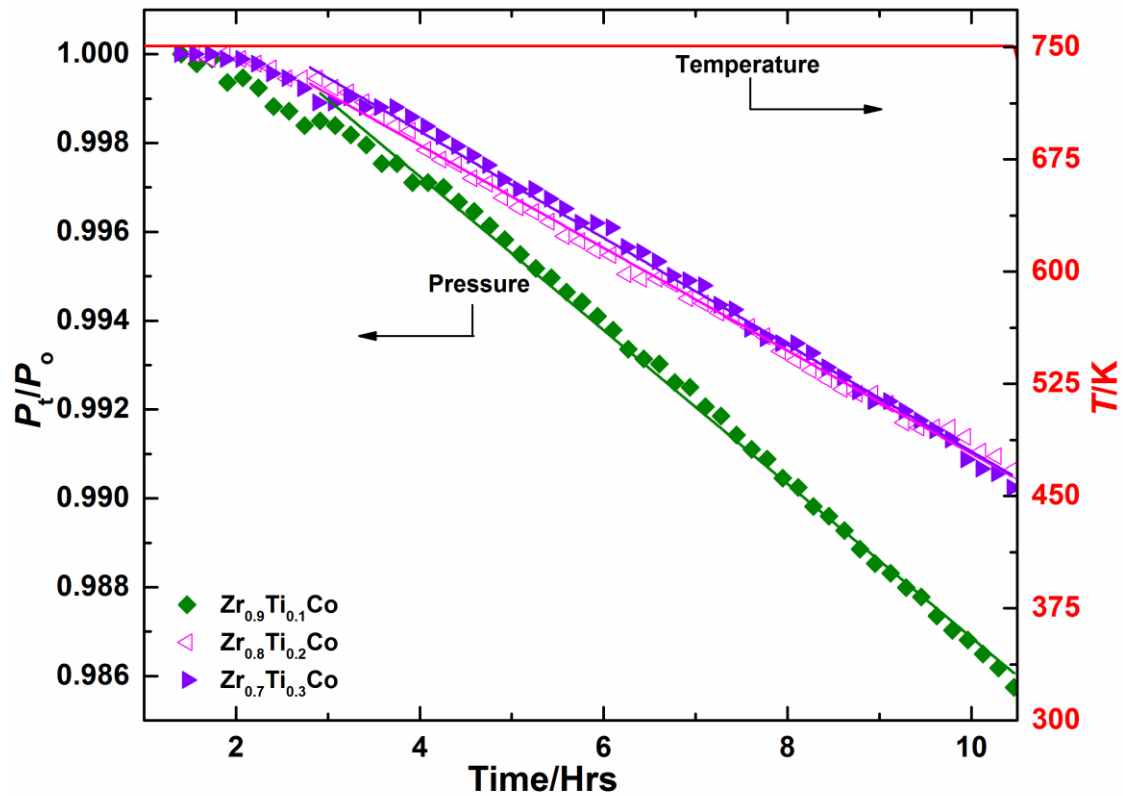


Figure 3.52: Change in pressure with time for $Zr_{1-x}Ti_xCo-H_2$ systems at 750 K.

Important observation from Figure 3.52 is that for $Zr_{1-x}Ti_xCo-H_2$ systems the drop in pressure is very low, ~ 2 kPa in 10 hours. Among all $Zr_{1-x}Ti_xCo-H_2$ systems, the highest rate of pressure drop is found to be for $x=0.1$ and the lowest is for $x=0.2$. These observations are in consistent with the occupancies of $8e$ site and its Zr-H distances, discussed in Section-3.5.3. Figure 3.51 also confirm the presence of phase similar to $ZrCoH_3$ for all Ti substituted ZrCo hydrides. Based on these observations, it can be proposed that among all Zr-Co-M ternary alloys the $Zr_{0.8}Ti_{0.2}Co$ alloy has highest durability against hydrogen induced disproportionation and hence it has a potential to substitute the highly pyrophoric and radioactive material uranium being used in tritium handling facilities.

CHAPTER 4

SUMMARY AND CONCLUSION

4 Summary and Conclusion

In the present thesis, a systematic approach has been applied to investigate the effect of ternary alloying on the hydrogen isotope storage properties of ZrCo alloy. Ternary alloys $\text{Zr}_{1-x}\text{Ti}_x\text{Co}$ and $\text{ZrCo}_{1-x}\text{M}_x$ (M= Ni and Fe) were prepared and characterized by different techniques like XRD, SEM, EDS and Elemental mapping. The hydrogen isotope storage behavior of Zr-Co-M ternary alloys were investigated by generating the hydrogen/deuterium desorption Pressure-Composition Isotherms (PCIs) by employing Sieverts' type volumetric apparatus. The thermodynamic parameters of the hydrogenation reactions and their corresponding isotopic effects were evaluated. Thermodynamic functions for desorption of hydrogen/deuterium in Zr-Co-M - H_2/D_2 systems are summarised in Table 4.1. Hydrogen induced disproportionation behavior of Zr-Co-M ternary alloys were investigated by hydrogen absorption-desorption cyclic life and isothermal studies. The phenomenon of hydrogen induced disproportionation in different Zr-Co-M ternary alloys was investigated by employing neutron powder diffraction (NPD) as the structural elucidation technique. Rietveld refinement results of NPD data of all Zr-Co-M deuterides are summarized in Table 4.2.

**Table 4.1: Thermodynamic functions for desorption of hydrogen/deuterium in Zr-Co-M
-H₂/D₂ systems.**

| System | | $\Delta_r H^0$ (kJ/mole H ₂) | $\Delta_r S^0$ (J/(mole H ₂ ·K)) | T_{des} (K) |
|--|-----------|---|--|-------------------------|
| ZrCo | Hydride | 83.7 ± 3.9 | 122.2 ± 3.9 | 683 |
| | Deuteride | 84.3 ± 0.6 | 124.5 ± 1.1 | 677 |
| ZrCo _{0.9} Ni _{0.1} | Hydride | 95.4 ± 0.9 | 144.1 ± 0.8 | 664 |
| | Deuteride | 95.5 ± 0.4 | 145.5 ± 1.2 | 656 |
| ZrCo _{0.8} Ni _{0.2} | Hydride | 93.4 ± 3.3 | 143.9 ± 3.4 | 650 |
| | Deuteride | 94.4 ± 1.3 | 145.5 ± 1.2 | 645 |
| ZrCo _{0.7} Ni _{0.3} | Hydride | 92.6 ± 2.3 | 143.9 ± 2.5 | 644 |
| | Deuteride | 92.9 ± 1.6 | 145.5 ± 2.3 | 638 |
| ZrCo _{0.9} Fe _{0.1} | Hydride | 69.2 ± 1.5 | 95.7 ± 1.0 | 723 |
| | Deuteride | 69.6 ± 1.2 | 97.7 ± 1.0 | 712 |
| Zr _{0.9} Ti _{0.1} Co | Hydride | 66.5 ± 0.3 | 97.7 ± 0.2 | 681 |
| | Deuteride | 71.9 ± 1.9 | 109.1 ± 1.8 | 658 |
| Zr _{0.8} Ti _{0.2} Co | Hydride | 63.7 ± 0.2 | 101.5 ± 0.2 | 628 |
| | Deuteride | 67.6 ± 0.3 | 109.1 ± 0.3 | 620 |
| Zr _{0.7} Ti _{0.3} Co | Hydride | 57.7 ± 2.0 | 101.5 ± 1.9 | 568 |
| | Deuteride | 59.3 ± 2.5 | 105.3 ± 2.4 | 563 |

Table 4.2: Rietveld refinement results of neutron diffraction data for Zr-Co-M deuterides

| Parameters | ZrCo | x in ZrCo _{1-x} Ni _x deuterides | | | | ZrCo _{0.9} Fe _{0.1} | x in Zr _{1-x} Ti _x Co deuterides | | |
|---------------------------------|------|---|-------------|------------|------------|---------------------------------------|--|-------------|-------------|
| | | 0.1 | 0.2 | 0.3 | | | 0.1 | 0.2 | 0.3 |
| D1 (4c ₂) (0 y 1/4) | y | 0.9269(39) | 0.9300(5) | 0.9282(3) | 0.9291(3) | 0.9279(3) | 0.9289(4) | 0.9273(4) | 0.9270(4) |
| Occupancy (%) | | 29.3 | 30.8 | 30.1 | 31.1 | 29.9 | 29.7 | 29.9 | 30.0 |
| D2 (8f ₁) (0 y z) | y | 0.3119(2) | 0.3125(3) | 0.3122(2) | 0.3119(2) | 0.3119(2) | 0.3124(3) | 0.3117(3) | 0.3110(3) |
| | z | 0.5047(6) | 0.5047(7) | 0.5062(4) | 0.5053(4) | 0.5041(5) | 0.5046(7) | 0.5059(7) | 0.5059(8) |
| Occupancy (%) | | 66.9 | 66.4 | 67.2 | 66.4 | 68.3 | 68.4 | 68.4 | 68.0 |
| D3 (8e) (x 0 0) | x | 0.2219(81) | 0.2243(139) | 0.2549(88) | 0.2637(95) | 0.3725(139) | 0.4135(204) | 0.2872(197) | 0.2846(178) |
| Occupancy (%) | | 3.8 | 2.8 | 2.7 | 2.5 | 1.8 | 1.8 | 1.7 | 2.0 |
| Zr-D distance (Å) | | 1.937(12) | 1.940(20) | 1.994(14) | 2.022(15) | 2.201(30) | 2.280(40) | 2.030(30) | 2.020(30) |
| R _p (%) | | 3.29 | 6.70 | 1.81 | 2.13 | 1.93 | 4.46 | 3.76 | 2.13 |
| R _{wp} (%) | | 4.15 | 9.86 | 2.36 | 2.89 | 2.45 | 5.57 | 4.78 | 2.89 |
| R _{exp} (%) | | 3.61 | 2.46 | 1.32 | 1.40 | 1.81 | 3.14 | 2.92 | 1.40 |

Following conclusions are drawn from the present study:

- (i) The X-ray diffraction patterns of $\text{ZrCo}_{1-x}\text{Ni}_x$ ($x = 0.0, 0.1, 0.2$ and 0.3), $\text{ZrCo}_{0.9}\text{Fe}_{0.1}$ and $\text{Zr}_{1-x}\text{Ti}_x\text{Co}$ ($x = 0.1, 0.2$ and 0.3) alloys confirm the formation of b.c.c. phase similar to ZrCo for all the alloys. All the alloys show a small fraction of ZrCo_2 as impurity phase.
- (ii) A single desorption plateau is observed for all the pressure-composition isotherms (PCIs).
- (iii) The hydrogen/deuterium desorption pressure-composition-temperature (PCT) studies revealed that the T_{des} for release of 100 kPa of H_2/D_2 systematically decreases with increase in Ni or Ti content and increases when cobalt is substituted with Fe. The lowest desorption temperature is observed for $\text{Zr}_{0.7}\text{Ti}_{0.3}\text{Co}$ alloy. The T_{des} for deuterides were found to be lower than those of corresponding hydrides.
- (iv) The thermodynamic parameters for hydrogen/deuterium desorption reactions were systematically investigated.
- (v) The normal hydrogen isotope effect is observed for all ternary alloys which shows that the equilibrium pressure of deuterium is higher than that of hydrogen at all experimental temperatures. This study revealed that equilibrium pressure of tritium at a particular temperature will be higher than that of deuterium and hydrogen for all ternary alloys.
- (vi) Structural studies by neutron powder diffraction reveal that in Zr-Co-M deuterides, deuterium occupies a new site $8e$ in addition to the earlier reported $4c_2$ and $8f_1$ sites. Occupancy of $8e$ site is found to be responsible for hydrogen induced disproportionation. Among all Zr-Co-M deuteride studied, $\text{Zr}_{0.8}\text{Ti}_{0.2}\text{Co}$ showed the lowest occupancy of $8e$ site.
- (vii) Isothermal disproportionation studies on these systems revealed that the $\text{Zr}_{0.8}\text{Ti}_{0.2}\text{Co}$ alloy has the highest durability against hydrogen induced disproportionation, which is in accordance with the neutron diffraction results.

- (viii) Considering the PCT studies, hydrogen induced disproportionation studies and structural studies, it is proposed that among the alloys studied, the $\text{Zr}_{0.8}\text{Ti}_{0.2}\text{Co}$ alloy is the most suitable non-pyrophoric and non-radioactive ternary alloy as a substitute for the conventionally used highly pyrophoric uranium bed for tritium storage applications. This alloy has potential for its use in tritium handling facilities for storage supply and recovery of hydrogen isotopes.
- (ix) The measurements of thermodynamic parameters like $\Delta_r H^\circ$ and $\Delta_r S^\circ$ of de-hydrogenation/de-deuteration of certain alloy has yielded the trend and magnitude of hydrogen isotope effect. However, due to experimental constraints such data could not be generated using tritium gas, in the present study. Considering the trend and magnitude of hydrogen isotope effect the tritium storage properties like equilibrium pressure, desorption temperature etc. for the concerned material can be predicted qualitatively. As it is known, the trends in thermodynamic properties are governed by the difference in zero point energies for hydrides, deuterides and tritides as well as the difference in absolute entropies of H_2 , D_2 and T_2 . Hence, by calculating the enthalpies of formation of hydrides, deuterides and tritides and correlating them with the difference in their respective zero point energies, it is viable to calculate the thermodynamic properties of tritides by extrapolating the data of hydrides and deuterides.

5 REFERENCES:

- [1] Hall DO, Lobina E. Private and public interests in water and energy. *Natural Resources Forum*. 2004;28:277-286.
- [2] Hook M, Tang X. Depletion of fossil fuels and anthropogenic climate change-A review. *Energy Policy*. 2013;52:797-809.
- [3] <https://www.iter-india.org/fusion-energy.php?id=24>
- [4] Schlabach L, Zuttel A. Hydrogen-storage materials for mobile application. *Nature*. 2001;414:353-58.
- [5] Sheffield J. Fusion Energy in India's Long-term Energy Future. Joint Institute of Energy and Environment. Report No. 2003-03.
- [6] Nuclear Astrophysics Compilation of Reaction rates (NACRE), Web page: http://pntpm3.ulb.ac.be/Nacre/barre_database.htm.
- [7] By Dstrozzi - Own work, CC BY 2.5, Web page: <https://commons.wikimedia.org/w/index.php?curid=2351259>.
- [8] Lawson JD. Some Criteria for a Power-producing Thermonuclear Reactor. *Proc. Phys. Soc. (London)* B70 (6) (1957).
- [9] Stephen O. Dean. Search for the Ultimate Energy Source: A History of the U.S. Fusion Energy Program. Springer;2013.
- [10] International Fusion Research Council. Status Report on Fusion Research. *Nuclear Fusion*. October 2005;45:10A.
- [11] An Assessment of the Prospects for Inertial Fusion Energy. National Academies Press. July 2013;pp.229.
- [12] International Thermonuclear Experimental Reactor (ITER). <<http://www.iter.org/>>.
- [13] ITER EDA Documentation Series No. 22, IAEA/ITER EDA/DS/22, 2001.

- [14] McCracken G, Stott P. Fusion: The Energy of the Universe. Elsevier Academic Press, London, UK;2005.
- [15] Figure supplied courtesy of JET-EFDA publications copyright Euratom, Author provided, <http://figures.euro-fusion.org/Images/JG95.113-55c1500.1500.jpg>.
- [16] Kakiuchi M. Hydrogen: Inorganic chemistry, in: R.B King (Ed.), Encyclopedia of Inorganic Chemistry, Vol. 3, Wiley;1994:1444-1471.
- [17] Souers PC. Hydrogen Properties for Fusion Energy, Univ. Calif Press, Berkeley;1986.
- [18] Lasser R. Tritium and Helium-3 in Metals. Springer Series in Mater. Sci. Vol 9. Springer-Verlag, Berlin;1989.
- [19] Encyclopedria Britannica. Micropredia. 15th ed. 11. Chicago. 933;1988.
- [20] Mannone F. (Ed.). Safety in Tritium Handling Technology, in: Eurocourses: Nuclear Science and Technology, Kluwer Academic Publishers;1993.
- [21] Evans EA. Tritium and its compounds. John Wiley. New York;1975.
- [22] Rudy CR, Rudy KC. Tritium half-life. MLM-248. Mound Laboratory. Miamisburg. Ohio;1977.
- [23] Eberle U, Felderhoff M, Schüth F. Chemical and physical solutions for hydrogen storage. Angew Chem Int Ed. 2009;48:6608-6630.
- [24] Züttel A. Materials for hydrogen storage. Mater Today. 2003;6:24-33.
- [25] Sherif SA, Zeytinoglu N, Veziroğlu TN. Liquid hydrogen: potential, problems, and a proposed research program. Int J Hydrogen Energy. 1997; 22(7):683-688.
- [26] Scanlon, L.G., et al., Hydrogen Storage Based on Physisorption. J Phys Chem B. 2009;113(14): 4708-4717.
- [27] Hirscher M, Hirose K. Handbook of Hydrogen Storage: New Materials for Future Energy Storage. Wiley;2010.

- [28] Sastri MVC, Viswanathan B, Murthy SS. Metal hydrides: fundamentals and applications, Narosa Publishing House, New Delhi;1998.
- [29] Lennard-Jones JE. Processes of adsorption and diffusion on solid surfaces. Trans Faraday Soc. 1932;28:333-359.
- [30] Andreasen A.,\ Hydrogen Storage Materials with Focus on Main Group I-II Elements, Ph. D. Dissertation, Risø National Laboratory, Denmark;2005.
- [31] Schlapbach L (Ed.). Hydrogen in Intermetallic Compounds II, Vol. 67 of Topics in Applied Physics, Springer-Verlag;1992.
- [32] Martin M, Gommel C, Borkhart C, Fromm E. Absorption and desorption kinetics of hydrogen storage alloys. J Alloys Compd. 1996;238(1–2):193-201.
- [33] Mueller WM, Blackledge JP, Libowitz GG. Metal Hydrides. Academic Press. New York;1968.
- [34] Gibbs JW. The Scientific Papers of J. Willard Gibbs, Vol. 1: Thermodynamics, Published by Dover Publications Inc.;1961.
- [35] Libowitz GG, Hayes H F, Gibb TRP. The system zirconium-nickel and hydrogen. Inorg Chem. 1957;62:76-79.
- [36] Flanagan TB, Bowerman BS, Biehl GE. Hysteris in Metal/Hydrogen systems. Scr Metall. 1980;14:443-447.
- [37] Buschow KHJ, Bouten PCP, Miedema AR. Hydrides formed from intermetallic compounds of two transition metals: a special class of ternary alloys. Rep Prog Phys. 1982;45:937-1039.
- [38] Bouten PCP, Miedema AR. On the heats of formation of the binary hydrides of transition metals. J Less-Common Met. 1980;71:147-160.
- [39] Sicking G. Isotope effect in metal-hydrogen systems. J Less-Common Met. 1984;101:169-190.

- [40] Andreev BM, Magomedbekov EP, Sicking GH. Interaction of Hydrogen Isotopes with Transition Metals and Intermetallic Compounds, Springer-Verlag, New York;1996.
- [41] Bekris N, Besserer U, Sirch M, Penzhorn R-D. "On the thermal stability of the zirconium/cobalt-hydrogen system". Fusion Eng Design. 2000;50:781-789.
- [42] Haar R, Friedman AS, Beckett CW. Ideal gas thermodynamic functions and isotope exchange functions for the diatomic hydrides, deuterides and tritides. Natl Bur Stand (U.S.), Monograph 20 (U.S.) GPO, Washington, D.C.;1961.
- [43] Penzhorn RD, Devillers M, Sirch M. Evaluation of ZrCo and other getters for tritium handling and storage. J Nucl Mater. 1990;170:217-231.
- [44] Willin E, Sirch M, Penzhorn RD, Devillers M. Metal getters for tritium storage. Fusion Technol. 1988;14:756-63.
- [45] Burger LL, Trevorrow LE. Release of Tritium from Fuel and Collection for Storage. Controlling Air-Borne Effluents from Fuel Cycle Plants (ANS-AIChE Meeting);1976.
- [46] Maienschein JL. Feasibility of Chemical Getter Beds in Scavenging Tritium from Inert Gases. Nuclear Technology. 1978;38:387-404.
- [47] Holtslander WJ, Miller JM. Immobilization and Packaging of Recovered Tritium, Report AECL-7757, Atomic Energy of Canada, Ltd.;1982.
- [48] Shmayda WT, Mayer P. Uranium beds for temporary tritium storage. J Less-Common Met. 1984;104:239-250.
- [49] Longhurst GR. Pyrophoricity of tritium-storage bed materials. Fusion Technol. 1998;14:750-755.
- [50] Yamamoto T, Tanaka S, Yamawaki H. Hydrogen absorption/desorption properties of U_2Ti . J Nucl Material. 1990;170:140-146.

- [51] Jat RA, Sawant SG, Rajan MB, Dhanuskar JR, Kaity S, Parida SC. Hydrogen isotope effect on storage behavior of U_2Ti and $UZr_{2.3}$. J Nucl Mater. 2013;443:316-320.
- [52] Yamamoto T, Yoneoka T, Kokubo S, Yamawaki M. Development of tritium processing material - A U-Zr alloy as a promising tritium storage material" Fusion Eng Design. 1989;7:363-367.
- [53] Nagasaki T, Konishi S, Katsuta H, Naruse Y. Zirconium-cobalt compound as the material for a reversible tritium getter. Fusion Technol. 1986;9:506-509.
- [54] Watanabe K, Tanaka K, Matsuyama H, Hasegawa K. ZrNi alloys as candidate getter materials for tritium processing. Fusion Eng Design 1991;18:27-32.
- [55] Ortman MS, Warren TJ, Smith DJ. Use of Metal Hydrides for Handling Tritium. Fusion Technol. 1985;8:2330-2334.
- [56] Lartigue C, Percheron-Guegan A, Achard JC, Tasset F. Thermodynamic and structural properties of $LaNi_{5-x}Mn_x$ compounds and their related hydrides. J Less-Common Metals. 1980;75:23-29.
- [57] Cho S, Chang MH, Yun SH, Kang HG, Jung KJ, Chung H, et al. ITER Storage and Delivery System R&D in Korea. IEEE Trans Plasma Sci. 2010;38:425-433.
- [58] Shim M, Chung H, Yoshida H, Jin H, Lee J, Song KM, et al. Hydriding/dehydriding characteristics on fast heat transfer response ZrCo bed for ITER. Fusion Eng Des. 2009;84:1763-1766.
- [59] Cho S, Chang MH, Yun SH, Kang HG, Chung H, Song KM, et al. R&D activities on the tritium storage and delivery system in Korea. Fus Sci Tech. 2011;60:1077-1082.
- [60] Shmayda WT, Heics AG, Kherani NP. Comparison of uranium and zirconium cobalt for tritium storage. J Less-Common Met. 1990;162:117-127.
- [61] Devillers M, Sirch M, Penzhorn RD. Hydrogen-induced disproportionation of the intermetallic compound ZrCo. Chem Mater. 1992;4:631-639.

- [62] Konishi S, Nagasaki T, Okuno K. Reversible disproportionation of ZrCo under high temperature and hydrogen pressure. *J Nucl Mater.* 1995;223:294-299.
- [63] Shim M, Chung H, Cho S, Yoshida H. Disproportionation Characteristics of a Zirconium-Cobalt Hydride Bed Under ITER Operating Conditions. *Fus Sci Tech.* 2008;53:830-840.
- [64] Bekris N, Sirch M. On the Mechanism of the Disproportionation of ZrCo Hydrides. *Fusion Sci Technol.* 2012;62:50-55.
- [65] Hara M, Okabe T, Mori K, Watanabe K. Kinetics and mechanism of hydrogen-induced disproportionation of ZrCo. *Fusion Eng Des.* 2000;49-50:831-838.
- [66] Irvine SJC, Harris IR. An investigation of the systems ZrCo-H₂ and ZrCo_{0.84}Ni_{0.16}-H₂. *J Less-Common Met.* 1980;74:33-43.
- [67] Konishi S, Nagasaki T, Hayashi T, Okuno K. Equilibrium hydrogen pressure on the solid solutions of ZrCo-HfCo Intermetallic compounds. *J Nucl Mater.* 1995;223:300-304.
- [68] Zhuo H, Xiaopeng L, Lijun J, Shumao W. Hydrogen storage properties of Zr_{1-x}Ti_xCo intermetallic compound. *Rare Metals.* 2006;25:200-203.
- [69] Gongli T, Xiaopeng L, Lijun J, Shumao W, Zhinian L, Hualing L. Dehydrogenation characteristic of Zr_{1-x}M_xCo (M=Hf, Sc) alloy. *Trans Nonferrous Met Soc China.* 2007;17:s949-953.
- [70] Peng L, Jiang C, Xu Q, Wu X. Hydrogen-induced disproportionation characteristics of Zr(1-x)Hf(x)Co(x = 0, 0.1, 0.2 and 0.3) alloys. *Fusion Eng Des.* 2013;88:299-303.
- [71] Zhao Y, Li R, Tang R, Li B, Yu R, Liu W, Kou H, Meng J. Effect of Ti substitution on hydrogen storage properties of Zr_{1-x}Ti_xCo (x = 0, 0.1, 0.2, 0.3) alloys. *J Energy Chemistry.* 2014;23:9-14.
- [72] Kroll WJ. The Production of Ductile Titanium. *Trans Electroch Soc.* 1940;78:35-47.

- [73] Bragg WL. The Diffraction of Short Electromagnetic Waves by a Crystal. Proceedings of the Cambridge Philosophical Society 1913;17:43-57.
- [74] Dehm G, Howe JM, Zweck J. In-Situ Electron Microscopy : Applications in Physics, Chemistry and Materials Science. Wiley-VCH Verlag GmbH, germany (2012).
- [75] Fahlman BD. Materials Chemistry. Springer Netherlands;2007.
- [76] Hauback BC. Structural characterisation of hydride materials, In: G. Walker (Ed), Solid-state hydrogen storage: Materials and chemistry. Woodhead Publishing Limited, Cambridge England;2008.
- [77] Ross DK. Neutron scattering studies for analyzing solid-state hydrogen storage, In: G. Walker (Ed), Solid-state hydrogen storage: Materials and chemistry. Woodhead Publishing Limited, Cambridge England;2008.
- [78] Squires GL. Introduction to the theory of thermal neutron scattering. Cambridge University Press, Cambridge;1978.
- [79] Rodriguez-Carvajal J. FULLPROF: A program for rietveld refinement and pattern matching analysis. Abstracts of the Satellite Meeting on Powder Diffraction of the XVthIUCr Congress, Toulouse, France.1990;p.127.
- [80] <http://www.icdd.com>
- [81] Rietveld HM. Line profiles of neutron powder-diffraction peaks for structure refinement. Acta Crystallogr. 1967;22:151-152.
- [82] Rietveld HM. A profile refinement method for nuclear and magnetic structures. J Appl Crystallogr. 1969;2:65-71.
- [83] Young RA (Ed.). The Rietveld method; IUCr Monographs on Crystallography no 5; Oxford University Press; New York;1993.
- [84] McCusker LB, Von Dreele RB, Cox DE, Louer D, Scardi P. Rietveld refinement guidelines. J Appl Cryst. 1999;32:36-50.

- [85] Roisnel T, Rodríguez-Carvajal J. WinPLOTTR: A Windows Tool for Powder Diffraction Pattern Analysis. *Materials Science Forum* 2001;378-381:118-123.
- [86] Broom DP. Hydrogen storage materials: the characterisation of their storage properties. Springer-Verlag, London;2011.
- [87] Karl J. Gross et al., Recommended Best Practices for the Characterization of Storage Properties of Hydrogen Storage Materials: V 3.34 (2012), National Renewable Energy Laboratory Contract No. 147388, H₂ Technology Consulting, LLC.
- [88] NIST Standard Reference Database 23, Web link: <http://www.nist.gov/srd/nist23.htm>
- [89] PCPDFWIN Version 2.2, 2001, JCPDS-ICDD.
- [90] Harris IR, Hussain D, Barraclough KG. The constitution of the binary equiatomic alloys of Zr with Fe, Co and Ni. *Scr Metall.* 1970;4:305-308.
- [91] Binary Alloy Phase Diagrams, 2nd Ed. Plus Updates, ASM International, The Materials Information Society;1990.
- [92] Hossain D, Harris IR, Barraclough KG. A study of ZrCo and related ternary phases represented by the general formula, $Zr_{50}Co_{50-x}Ni_x$. *J Less-Common Met.* 1974;37:35-57.
- [93] Wicke E, Brodowsky H. Hydrogen in palladium and palladium alloys. in *Hydrogen in Metals-II.* edited by Alefeld G, Volkl J. Springer-Verlag, Berlin. 1978;29:73-155.
- [94] Kost ME, Padurets LN, Chertkov AA, Mikheeva VI. Dissociation isotherms in the ZrNi-H₂(D₂) and ZrCo-H₂(D₂) systems. *Russ J Inorg Chem.* 1980;25:471-473.
- [95] Heics AG, Shmayda WT. Tritium ageing of zirconium cobalt. *Fusion Technol.* 1992;21:1030-1034.
- [96] Westlake DG. Stoichiometries and interstitial site occupation in the hydrides of ZrNi and other isostructural intermetallic compounds. *J Less-Common Met.* 1980;75:177-185.

- [97] Carvalho EM, Harris IR. X-ray diffraction studies of structural changes in the system $\text{Zr}_{50}\text{Co}_{50-x}\text{Ni}_x$ ($0 \leq x \leq 50$): III. J Less-Common Met. 1985;106:143-152.
- [98] Harris IR, Norman M. Observations on the lattice spacings of some $\alpha\text{Pd-X}$ solid solutions and some Pd_3X phases. J Less-Common Met. 1970;22:127-130.
- [99] Konishi S, Nagasaki T, Yokokawa N, Naruse Y. Development of zirconium-Cobalt beds for recovery, storage and supply of tritium. Fusion Eng Des. 1989;10:355-358.
- [100] Devillers M, Sirch M, Brendendiek-Kamper S, Penzhorn RD. Characterization of the ZrCo-Hydrogen System in View of Its Use for Tritium Storage. Chem Mater. 1990;2:255-262.
- [101] Lundin CE, Lynch FE, Magee CB. A correlation between the interstitial hole sizes in intermetallic compounds and the thermodynamic properties of the hydrides formed from those compounds. J Less-Common Met. 1977;56:19-37.
- [102] Scherrer P. Bestimmung der Grösse und der Inneren Struktur von Kolloidteilchen Mittels Röntgenstrahlen, Nachrichten von der Gesellschaft der Wissenschaften, Göttingen. Mathematisch-Physikalische Klasse. 1981;2:98-100.
- [103] Singh RK, Lototsky MV, Srivastava ON. Thermodynamical, structural, hydrogen storage properties and simulation studies of P–C isotherms of $(\text{La}, \text{Mm})\text{Ni}_{5-y}\text{Fe}_y$. Int J Hydrogen Energy. 2007;32:2971-2976.
- [104] Davidson DJ, Sai Raman SS, Lototsky MV, Srivastava ON. On the computer simulation of the P–C isotherms of ZrFe_2 type hydrogen storage materials. Int J Hydrogen Energy. 2003;28:1425-1431.
- [105] Zhang et al., Effects and mechanism of Ti, Ni, Sc, Fe substitution on the thermal stability of zirconium cobalt–hydrogen system, Int J Hydrogen Energy. 2015;40:6582-6593.

- [106] Kou et al., Comparative study of full-scale thin double-layered annulus beds loaded with ZrCo, $\text{Zr}_{0.8}\text{Hf}_{0.2}\text{Co}$ and $\text{Zr}_{0.8}\text{Ti}_{0.2}\text{Co}$ for recovery and delivery of hydrogen isotopes. *Int J Hydrogen Energy*. 2015;40:10923-10933.
- [107] Irodova AV, Somenkov VA, Shil'shtein SS, Padurets LN, Chertkov AA. Structure of ZrCoD_3 . *Sov Phys Crystallogr*. 1978;23:591-592.
- [108] Hara M, Kanesaka I, Watanabe K, Kabutomori T. Durability of ZrCo and ZrNi against absorption–desorption cycles in hydrogen. *Ann Rep Hydrog Isot Res Center Toyama Univ*. 1994;14:85-96.
- [109] Libowitz GG, Hayes HF, Gibb Jr TRP. The system zirconium-nickel and hydrogen. *J Phys Chem*. 1958;62:76-79.
- [110] Hahn Th. *International Tables for Crystallography, Volume A: Space-group symmetry*. Kluwer Academic Publishers, Dordrecht, The Netherlands 1995.
- [111] Switendick AC. Theoretical Study of Hydrogen in Metals: Current Status and Further Prospects. SAND, 1978, 78-0250.
- [112] Peterson SW, Sadana VN, Korst WL. Neutron diffraction study of nickel zirconium hydride. *J Phys*. 1964;25:451-453.
- [113] Jacob I, Bloch JM. Interstitial site occupation of hydrogen atoms in intermetallic hydrides: ZrNiH_x case. *Solid State Commun*. 1982;42:541-545.
- [114] Fredrickson DR, Nuttall RL, Flotow HE, Hubbard WN. The Enthalpies of Formation of Zirconium Dihydride and Zirconium Dideuteride. *J Phys Chem*. 1963;67:1506-1509.
- [115] Gachon JC, Hertz J. Enthalpies of formation of binary phases in the systems FeTi, FeZr, CoTi, CoZr, NiTi, and NiZr, by direct reaction calorimetry. *CALPHAD* 1983;7:1-12.

- [116] Watanabe K, Hara M, Matsuyama M, Kanesaka I, Kabutomori T. Stability of ZrCo and ZrNi to heat cycles in hydrogen atmosphere. *Fusion Technol.* 1995;28:1437-1442.
- [117] Hara M, Kobayashi T, Watanabe K, Okabe T, Kabutomori T. Hydrogen induced disproportionation of ZrCo at constant temperatures in hydrogen atmosphere. *Ann Rep Hydrog Isot Res Center Toyama Univ.* 1995;15:75-83.
- [118] Hara M, Kobayashi T, Kobayashi T, Okabe T, Mori K, Watanabe K. Isotope effect on disproportionation of ZrCo. *Ann Rep Hydrog Isot Res Center* 1996;16:69-79.